The Pennsylvania State University

The Graduate School

Department of Materials Science and Engineering

PULSED-LASER CRYSTALLIZATION OF FERROELECTRIC/PIEZOELECTRIC OXIDE THIN FILMS

A Dissertation in

Materials Science and Engineering

by

Adarsh Rajashekhar

Submitted in Partial Fulfillment of the Requirements for the Degree of

Doctor of Philosophy

May 2017

The dissertation of Adarsh Rajashekhar was reviewed and approved* by the following:

Susan Trolier-McKinstry
Professor of Ceramic Science and Engineering
Dissertation Advisor
Chair of Committee

Clive A. Randall
Professor of Materials Science and Engineering

Long-Qing Chen
Distinguished Professor of Materials Science and Engineering

Srinivas Tadigadapa
Professor of Electrical Engineering

Suzanne Mohney

Professor of Materials Science and Engineering and Electrical Engineering
Chair, Intercollege Graduate Degree Program in Materials Science and Engineering

*Signatures are on file in the Graduate School

Abstract

Integration of ferroelectric/piezoelectric thin films, such as those of lead zirconate titanate (PZT), with temperature sensitive substrates (complementary metal oxide semiconductors (CMOS), or polymers) would benefit from growth at substrate temperatures below 400˚C. However, high temperatures are usually required for obtaining good quality PZT films via conventional routes like rapid thermal processing (>550°C). Those conditions are not compatible either with polymer substrates or completed CMOS circuits and dictate exploration of alternative methods to realize integration with such substrates.

In part of this work, factors influencing KrF excimer laser induced crystallization of amorphous sputtered $Pb(Zr_{0.30}Ti_{0.70})O_3$ thin films at substrate temperatures <~215°C were investigated. (111) Pt/Si substrates were utilized to understand the process window. Laser energy densities studied were in the range 35 – 85 mJ/cm^2. The Pb content in the films was varied via the Ar gas pressure (in the range 5 mTorr – 9 mTorr) during sputtering of amorphous films. It was seen that a higher Pb content in the as-deposited films aided nucleation of the perovskite phase. Ozone-containing ambients (10% O_3/90% O_2) during the annealing promoted the formation of the metastable Pb-rich pyrochlore/fluorite phase, while annealing in pure oxygen produced the perovskite phase at relatively lower annealing laser energy densities. Heterogeneous nucleation from the substrate is favored on utilizing a layer-by-layer growth and crystallization process. Films were also grown on polymers using this method. Ferroelectric switching

was demonstrated, but extensive process optimization would be needed to reduce leakage and porosity.

Real time laser annealing during growth allows for scaling of the layer-by-layer growth process. A pulsed laser deposition system with *in situ* laser annealing was thus designed, built, and utilized to grow $Pb(Zr_{0.52}Ti_{0.48})O_3$ thin films on a laser crystallized $Pb(Zr_{0.20}Ti_{0.80})O_3$ seed layer, at a temperature of ~370˚C. Polycrystalline 1.1 μm thick films exhibited columnar grains with small grain sizes (~30 nm). The films showed well-saturated hysteresis loops (with a remanent polarization of ~25 $\mu C/cm^2$, and a coercive field of ~50 kV/cm) and exhibited loss tangents <2.5% with a permittivity of ~730. Film orientation could be controlled via the substrate choice; {111} $Pb(Zr_{0.52}Ti_{0.48})O_3$ films were grown on oriented (111) $Pb(Zr_{0.30}Ti_{0.70})O_3$ sol-gel seed layers, while epitaxial {001} films were prepared on (100) $SrTiO_3$ single crystals.

In order to study the microstructure evolution in these films, *in situ* pulsed-laser annealing was used to grow crystalline lead zirconate titanate ($PbZr_{0.52}Ti_{0.48}O_3$) thin films at a substrate temperature of ~370˚C on $PbZr_{0.30}Ti_{0.70}O_3$-buffered platinized silicon substrates. Transmission electron microscopy (TEM) analysis indicated that the films were well crystallized into columnar grains, but with pores segregated at the grain boundaries. Lateral densification of the grain columns was significantly improved by reducing the partial pressure of oxygen from 120 mTorr to 50 mTorr, presumably due to enhanced adatom mobility at the surface accompanying increased bombardment. It was found that varying the fractional annealing duration with respect to the deposition duration produced little effect on lateral grain growth. However, increasing the fractional annealing duration led to shift of 111 PZT X-ray diffraction peaks to higher

2θ values, suggesting residual in-plane tensile stresses in the films. Thermal simulations were used to understand the annealing process. Evolution of the film microstructure is described in terms of transient heating from the pulsed laser determining the nucleation events, while the energy of the arriving species dictates grain growth/coarsening.

Table of Contents

LIST OF FIGURES

LIST OF TABLES

ACKNOWLEDGEMENTS

First and foremost, I would like to immensely thank my advisor Dr. Susan Trolier-McKinstry, for showing faith in me through the ups and downs, and guiding me through this work. Among several things, I have been really fortunate in witnessing and obtaining education from her exceptional research acumen. She provides her students with an opportunity to explore new avenues, which in turn gave me the courage to tackle challenging assignments, while also helping to overcome any inherent diffidence. Apart from the vast scientific aspect of the doctorate program, the tremendous hands-on component that she entrusted me with has made me grow as an individual, for which I will be highly grateful throughout my professional and personal pursuits.

Also, no amount of thanks would suffice for the support of Raja (Bharadwaja Srowthi), Austin Fox, Chris Jabco, Tim Klinger, Bill Drawl and Jeff Long for helping me during the design and construction of the experimental setup, on which a good amount of this work is based. With regards to the great learning curve that this unique system construction posed, a huge amount of patience would have been required on part of anyone involved, and they made sure I get back to the right path with their vast expertise.

The staff members at the Materials Research Institute (MRI), and at the Materials Characterization Laboratory have been a great resource both in terms of knowledge as well as the research work right from the processing of the thin films, their patterning and their characterization. I would like to especially thank Trevor Clark, Ke Wang, Dan Veghte, Josh Maier for their help with TEM characterization of the samples. Also, very special mention of Beth Jones for helping me with umpteen aspects, including bulk

target processing, sol-gel films, as well as for assisting me to address the problems on the sputter tool whenever they arose.

I would like to extend my gratitude to Huairuo Zhang and Dr. Ian Reaney of the University of Sheffield for their ever-valuable inputs in terms of TEM characterization of the films and the insightful analysis. It has been a pleasure to work with them.

Also, I am highly grateful to Shawna Liff, Feras Eid, and Tom Sounart from Intel Inc., Arizona, for the very encouraging monthly discussions on attempting and attaining an important goal of this program. Their inputs went a long way in the analysis as well as in directing the path of the various challenging tasks.

I would also like to specially thank Albert Queralto for his help with me getting initiated to the thermal finite element modeling using COMSOL. This allowed me to add a theoretical component into the experimental observations.

Well, I have been blessed to be a part of a wonderful group in the form of past and present lab members, Dan Tinberg, Flavio Griggio, Ichiro Fujii, Raegan Johnson, Derek Wilke, Song Won Ko, Aaron Welsh, Charley Yeager, Lauren Garten, Jung In Yang, Dan Marincel, Margeaux Wallace, Ryan Keech, Hong Goo Yeo, Carl Morandi, Smitha Shetty, Wanlin Zhu, Betul Akkopru, Sun Young Lee, Jon Bock, Trent Borman, Lyndsey Denis, Dixiong Wang, Jason Chan. I will be highly indebted to the intellectually stimulating conversations that were held at the Materials Research Lab and Millennium Science Complex corridors and also the various trainings with the instruments, making our research lives a lot easier. I will hope to keep the spirit of discussions and good camaraderie alive wherever I will end up being.

Last but not the least I would like to thank my mom and dad for being very supportive all these years, and also to my various friends in State College: Dheeraj Mohata, Ashkar Ali, Aseem Singh, Sandeep Kumar, Priyanka Mishra, Yogesh Bansal, Arnab Sen Gupta, Michael Abraham, Kshitij Jerath, Jaswanth Mentey, Shashank Sharma, Lavish Pabbi, Riju Banerjee, Alok Bakshi and many others who have directly or indirectly motivated me during times of need.

This work could never have happened if not for the funds from a National Science and Engineering Faculty Fellowship (NSSEFF) from the Department of Defense (DoD) and as well as from Intel Inc., through the Semiconductor Research Corporation (SRC). I thank them for sharing our research vision.

Chapter 1 Background

Recent technological advances have seen the emergence of the Internet of Things (IOT) and improved healthcare facilities [1]. Among other things, these developments dictate the need for embedded electronics and sensors, preferably flexible and stretchable systems, to monitor health in real-time. For versatility, hybrid systems may be necessary, where functional inorganic active elements are integrated onto organic substrates. Two primary ways to realize this assembly are: transfer processes and direct deposition of inorganic films on plastic substrates [1] [2]. The transfer processes have the advantage of integrating microfabricated devices onto organic substrates without imposing any limitations on the high processing temperatures characteristic of inorganic materials. However, this typically adds non-conventional processing steps while also lowering the yield [1]. Direct deposition of the active layers onto the polymeric substrates removes these challenges. However, in this case, restricted processing temperatures need to be addressed.

Localized heating by a laser became popular in 1977 for restoring the crystallinity of silicon after ion-implantation damage [3]–[5]. Laser annealing was used to form low temperature poly-silicon (LTPS) in thin film transistor – liquid crystal displays (TFT-LCD), via melting and recrystallization of the Si layer [6]. Surface heating by this method avoids heating of the entire substrate. The effects of laser annealing are well known in the silicon industry. Extension of this technique to inorganic electroceramic thin films holds promise for

integrating crystalline functional films with temperature sensitive substrates and is discussed in the subsequent sections.

1.1 Ferroelectric Thin Films and Need for Low Temperature Processing

Lead Zirconate Titanate (PZT) ceramics have been the mainstay of highly functional piezoelectric devices for decades, with applications ranging from sensors to actuators, to sonar systems and ultrasonic imaging arrays. Thin films of PZT are attractive for ferroelectric memory devices [7],[8],[9] and microelectromechanical systems (MEMS) [10],[11],[12],[13]. In order to obtain good functional properties in thin films, processing at temperatures in excess of 550˚C is typically necessary, irrespective of the deposition technique. Although there have been reports of low temperature processing by conventional techniques [14], the electrical properties and microstructures are generally compromised.

Direct integration of PZT thin films onto flexible polymers would, however, mean that this processing temperature has to be brought down. Incorporating actuators on low stiffness substrates such as organic polymers leads to amplification of the displacements for an applied voltage, while flexible sensors would allow monitoring of vital health signs [15],[16],[17]. Integration with polymeric substrates also has potential in producing MEMS energy harvesters (Figure 1-1) for use in self-powered wireless sensor network systems [18], [19]. Complex transfer printing techniques have been used in most of these works to obtain the heterogeneous assembly [2]. However, comparatively less work has been reported in the existing literature on direct monolithic integration of PZT films on polymeric substrates.

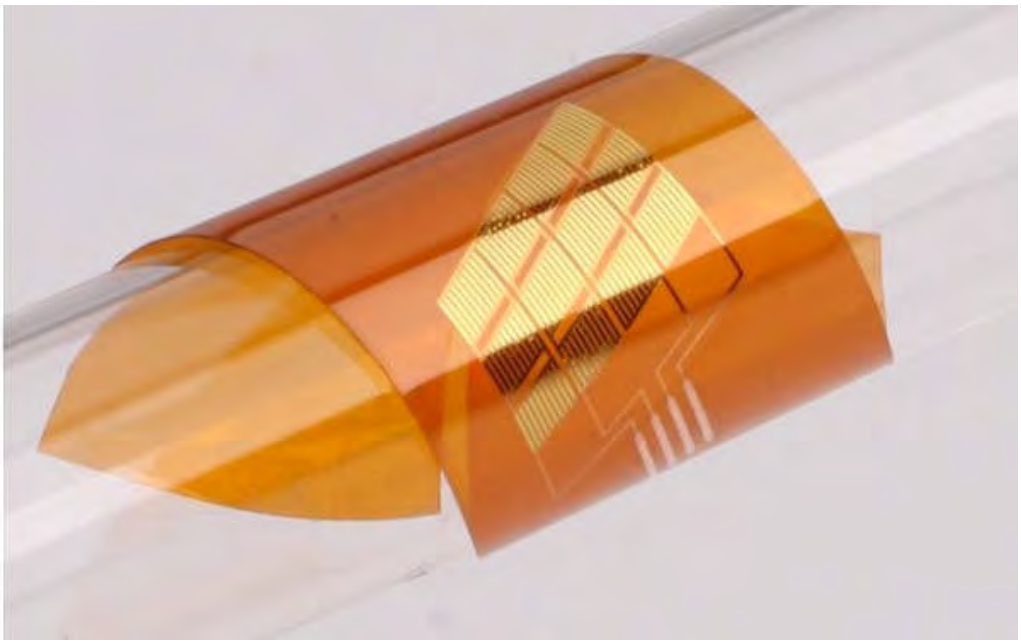

Figure 1-1 Flexible mechanical energy harvesters (MEHs) containing PZT nanoribbons for energy harvesting from organs (from Ref. [19]**). Here, transfer printing was used for the heterogeneous integration.**

Another avenue in which low temperature integration of piezoelectric electroceramics may produce significant value is on integrated circuits [20]. As the aluminum metallization would not survive temperatures higher than about 425˚C, fabrication of piezoelectric based MEMS structures generally requires the active piezoelectric element to be physically separated from the read-out or driving circuits [21][22]. However, direct integration of the piezoelectric thin film with a microchip would improve response times in sensors, potentially coupled with low cost manufacturing [20], and would necessitate lowering of the temperatures required for the fabrication of the piezoelectric/ferroelectric layer. An example of a ferroelectric capacitor integrated with a complementary metal oxide semiconductor (CMOS) transistor is the ferroelectric random access memory (FeRAM). However, in the conventional FeRAM technology (Figure 1-2), in order to avoid damage

to the metal layers, the metallization step is carried out in the back-end-of-the line (BEOL), and after the fabrication of the ferroelectric capacitor on the CMOS transistor [23]. But the post-metal forming gas (H_2/N_2 mixture) anneals (typically done to control the transistor SiO_2/Si interface states) are known to induce degradation of the ferroelectric capacitor performance owing to the deoxidization of the metal oxides. Furthermore, the ferroelectric degradation can also be caused due to the hydrogen-containing precursors employed in chemical vapor deposition (CVD) of various dielectric layers such as SiO_2 and Si_3N_4 as part of the capacitor level dielectric (CLD) (see Figure 1-2). These factors pose process challenges in terms of the barrier layers (against reducing atmospheres) for the ferroelectric capacitor and also the CLD layers [24]. If possible, completing the complementary metal oxide semiconductor (CMOS) microfabrication processes before the fabrication of the ferroelectric capacitor would reduce chances of cross-contamination [6].

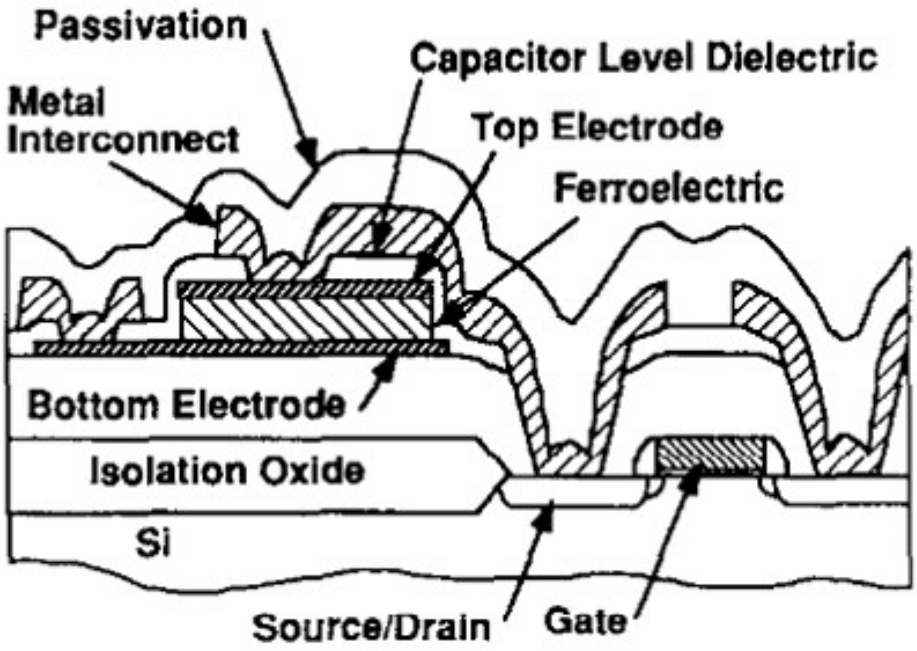

Figure 1-2: Cross-section of an FeRAM circuit (from Ref. [23]**)**

A review of characteristic processing temperatures for crystalline PZT films is found in Ref. [25]; some important points are summarized here. One of the key factors affecting the crystallization temperature of the piezoelectrically active perovskite PZT phase is the characteristic Zr/Ti ratio of the composition. For a given deposition technique, Ti-rich compositions (low Zr/Ti ratios) are known to crystallize at a lower temperature (Figure 1-3) [26]. In ref. [26] the temperature range for complete conversion was seen to be in the range from 475 °C to 650 °C depending on the Ti-content. At lower temperatures, Pb-rich fluorite phases (a disordered pyrochlore; $Pb_{2+x}(Zr,Ti)_2O_{7-y}$) are metastable, while at higher temperatures (above 650-700 °C), the Pb-deficient pyrochlore (e.g. $PbTi_3O_7$) is formed, due to the Pb-loss [25]. Precise Pb-control is necessary for low-temperature processed films, as excess Pb might not evaporate [25]. Also, the Pb valence needs to be controlled, as oxidation of PbO to Pb_3O_4 and PbO_2 occurs at temperatures below ~450˚C [25], [27].

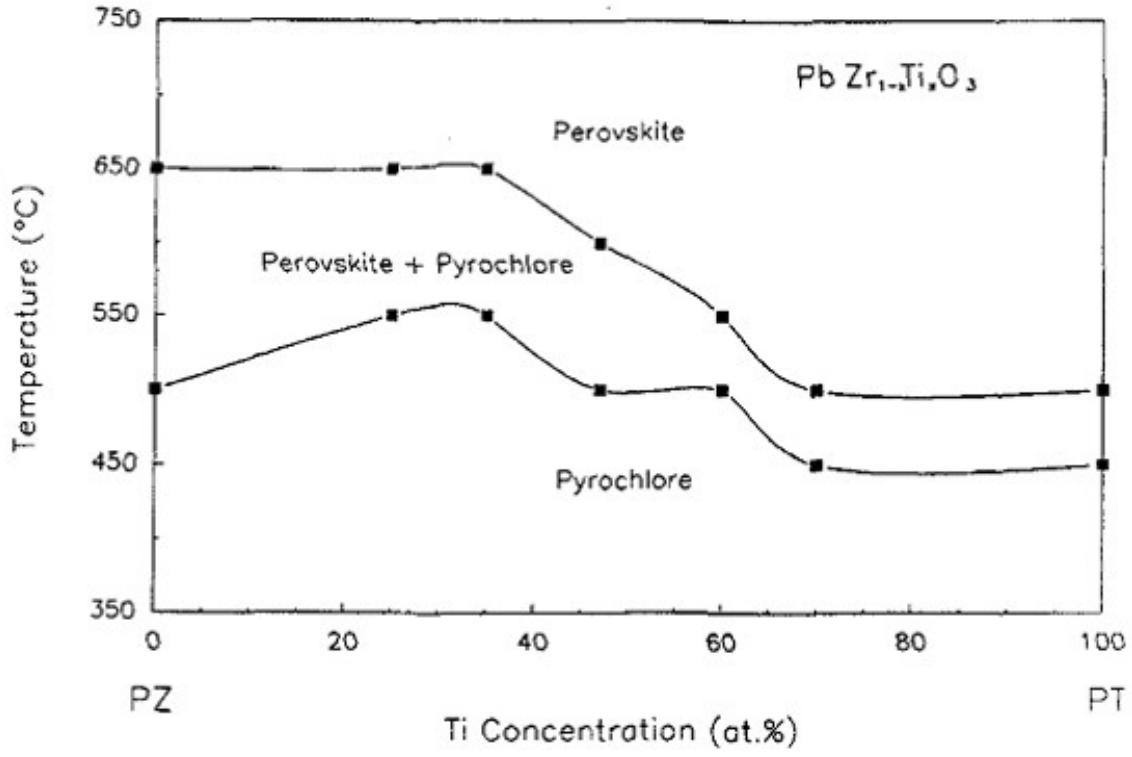

Figure 1-3: Phase transformation as a function of Ti concentration in PZT thin films (The composition is varied in between PZ ($PbZrO_3$), and PT ($PbTiO_3$) end members) (reproduced from [26])

With respect to post-deposition crystallization techniques, various methods of heating have been employed. Two of the most common heating routes include conventional furnace annealing (CFA) and rapid thermal annealing (RTA). RTA has the advantage of lowering the thermal budgets to crystallize the piezoelectric material. It has been generally observed that in comparison to CFA, the high heating rates involved in an RTA cause: (a) reduction in crystallization temperatures of PZT, (b) significantly reduced crystallization time-scales; seconds for RTA vs. minutes to hours in the case of CFA and (c) minimization of interface reactions [28]. The differences can be explained in terms of the variation in crystallization

kinetics, with CFA being dominated by thermodynamics while RTA is dominated by kinetics. For example, the authors in [29] studied the effect of heating rate on the crystallization behavior of PZT thin films. They concluded that high heating rates (several 10's of °C/s), characteristic of an RTA, delays the initiation of perovskite crystallization to high enough temperatures, partially bypassing the intermediate fluorite phase, and reducing the duration required for complete crystallization, as compared to CFA. Furthermore, in the case of RTA, the excess free energy in the amorphous state (Figure 1-4) is stored to higher temperatures where it is released, inducing nucleation and growth of the perovskite phase (termed 'explosive' crystallization). This lowers the temperatures required for complete conversion to the perovskite phase.

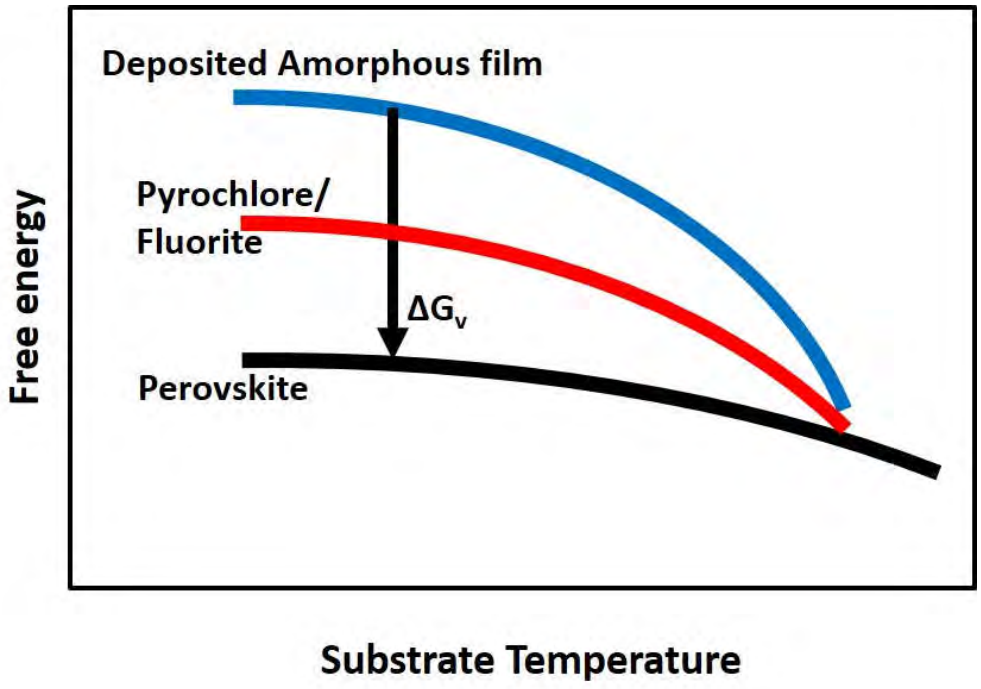

Figure 1-4: PZT free energy as a function of substrate temperature for amorphous, intermediate, and perovskite phases; ΔG_v is the driving force for crystallization (equivalent to the excess free energy release on conversion from amorphous to crystalline state) (adapted from [30]**,** [31]**)**

Lasers are an intense, directed source of energy, and should even further reduce the necessary thermal budget for crystallization of PZT films. At low to medium laser intensities, the laser acts as a heat source via photothermal effects [32]. Laser-induced chemical reactions due to the absorption of photons with high enough energy are also possible and are termed photochemical effects [32]. Laser interaction with the reactive gas should also be considered. Using lasers as a heat source, the heating can be localized to the surface layers, causing minimal heating of the substrate and reducing any chances of film-substrate interfacial reactions. To understand this further, a basic understanding of the laser-material interaction and the ensuing heating is discussed in the following section.

1.2 Laser-Material Interaction

A good understanding of laser-material interactions can be garnered from References [33], [34]. Electromagnetic radiation in the near UV (ultraviolet) to near IR (infrared) has frequencies on the order of THz ($10^{12} – 10^{14}$ Hz). Apart from a material's phonon response in the near IR, only electrons in a material are capable of interacting with such high frequencies, as the nuclei are too heavy to respond in the visible and near UV regions. Core electrons are not affected by these photon energies. Thus, the electrons that respond during laser annealing are the outer-shell bound and free electrons [33]. Interaction with the bound electrons causes change in the phase velocity of the beam (due to the refractive index). Free electrons can gain energy from the beam, which can then be transferred to the lattice by collisions. The oscillating bound and free electrons reradiate some energy, contributing to the reflected beam.

The time (t) dependent oscillating electric field ($\vec{E}$) due to an electromagnetic plane-wave with wavelength λ, frequency ω, and maximum amplitude $\vec{E}_o$ propagating along the direction z can be expressed as [33]:

$$\vec{E} = \vec{E}_o exp\left(i\left(\frac{2\pi}{\lambda}z - \omega t\right)\right) \quad (1)$$

The material reacts to this field by creating an oscillating dielectric polarization ($\vec{P}$). The linear material response on interacting with this field can be expressed as:

$$\vec{P} = \tilde{\epsilon}\vec{E} \quad (2)$$

where $\tilde{\epsilon} = \epsilon_1 + i\epsilon_2$ is the complex dielectric permittivity of the material. The interaction can also be expressed in terms of the complex refractive index ($\tilde{n} = n + ik$) of the material. Here, n is the real part of the refractive index while k is the extinction coefficient and characterizes the attenuation of the electric field amplitude as a result of absorption. The dielectric permittivity and the refractive index are related by the following [33]:

$$\tilde{\epsilon} = \tilde{n}^2 \quad (3)$$

Two main quantities emerge. One is the absorption coefficient (α) which is the inverse of the optical penetration depth $\left(\frac{1}{d_{optical}}\right)$ and is related to the wavelength of the light and the extinction coefficient of the material by the following equation [33].

$$\alpha = \frac{1}{d_{optical}} = \frac{4\pi k}{\lambda} \quad (4)$$

The other important quantity is the reflectivity (R). At normal incidence of the light beam, this quantity can be calculated from the following [33]:

$$R = \frac{(n-1)^2 + k^2}{(n+1)^2 + k^2} \quad (5)$$

A schematic of the absorption of laser light by a material (on irradiation with a photon energy higher than the characteristic bandgap) is shown in the Figure 1-5. This generates free carriers, which in turn can give rise to further absorption of the beam (called the free carrier absorption). These processes happen on the order of 10^{-14} seconds [33]. These excited electrons thermalize, creating a dense electron plasma (shaded region), before eventually losing energy (e.g. by electron-phonon collisions which happens in a time scale of 10^{-12} s), causing heating of the sample.

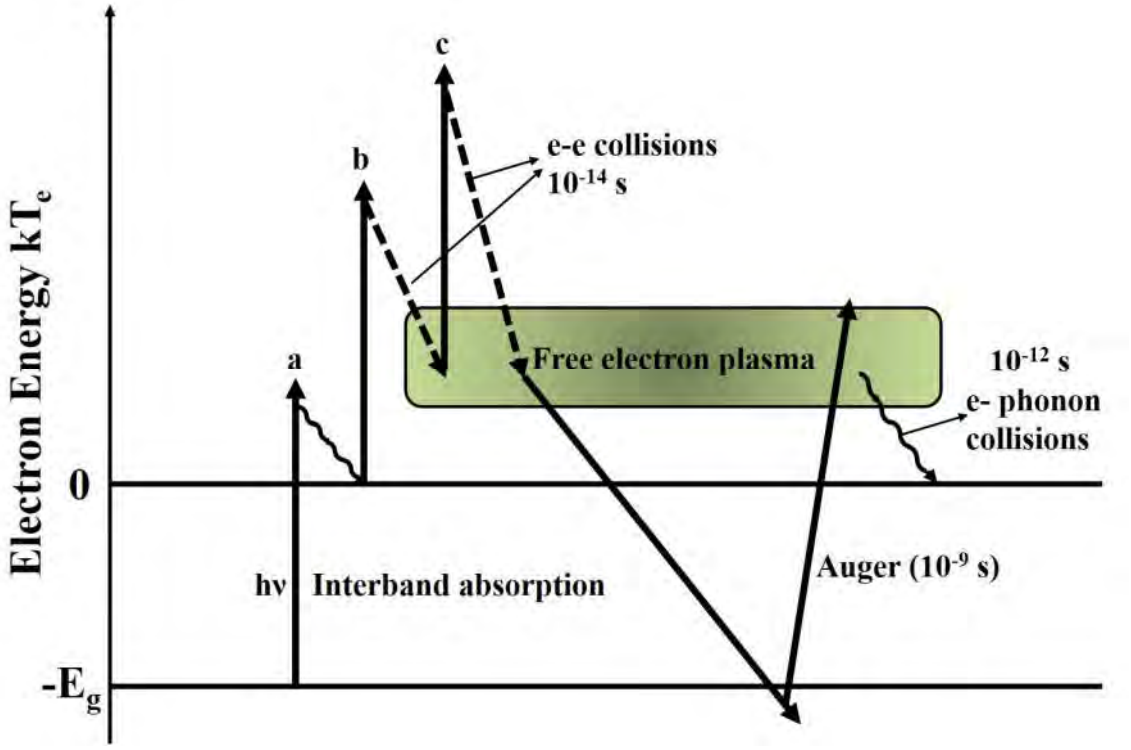

Figure 1-5 Band to band excitation (a) and free carrier absorption (b, c) on irradiation with intense laser light (reproduced from Ref. [34]**; e-e (electron-electron), e-ph (electron-phonon) collisions, hυ: absorption of photon, E_g: energy gap, kT_e: electron energy)**

Laser-Absorption and Heat Conduction

For a uniform laser beam irradiating a sample, laser heating can be modeled using the 1-D heat equation [34].

$$\rho C_p \frac{\partial T(z,t)}{\partial t} = \vec{\nabla}\left(K_{Th}\vec{\nabla}T(z,t)\right) + Q(z,t) \quad (6)$$

Here, ρ: density, C_p: specific heat, T: temperature, t: time, K_{Th}: thermal conductivity. Q is the heat source distribution in the sample as a function of depth (z) which in turn can be expressed in terms of the laser intensity (I_o), the reflectivity of the surface (R) and absorption coefficient of the materials (α) as [34]:

$$Q(z,t) = I_o(t)(1-R)\,\alpha \exp(-\alpha z) \quad (7)$$

The time evolution of the laser pulse intensity profile (I_o) can be modeled with a Gaussian-like function as follows:

$$I_o(t) = \left(\frac{F}{\tau_p}\right)\exp\left[-4\ln 2\left(\frac{t-2\tau_p}{\tau_p}\right)^2\right] \quad (8)$$

where F: laser fluence, τ_p: pulsewidth (Full Width at Half Maximum) of the laser.

These equations can be used to model the temperature profiles inside a material that is undergoing laser processing. The literature on nanosecond laser annealing of Si details the importance of using the right pulse profile for temperature modeling [35]. There, modeling using a Gaussian profile and a rectangular pulse profile (Figure 1-6) were compared and differences in the overall heating profiles and melting durations were estimated (Figure 1-7). Because most of the earlier literature on laser annealing of silicon [33], [34] used a simplified picture of the laser pulse (e.g. it was treated as a rectangular one), the trends in results are much more relevant than the exact values of melt depths and durations.

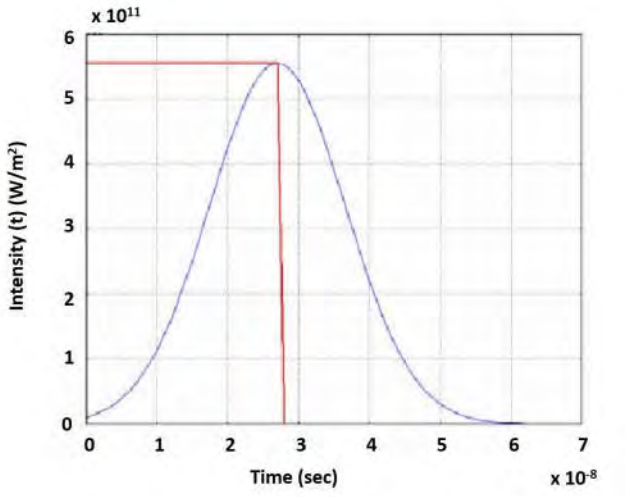

Figure 1-6 Gaussian pulse (blue) vs a rectangular pulse (red) used for modeling transient heat conduction in Ref. [35]

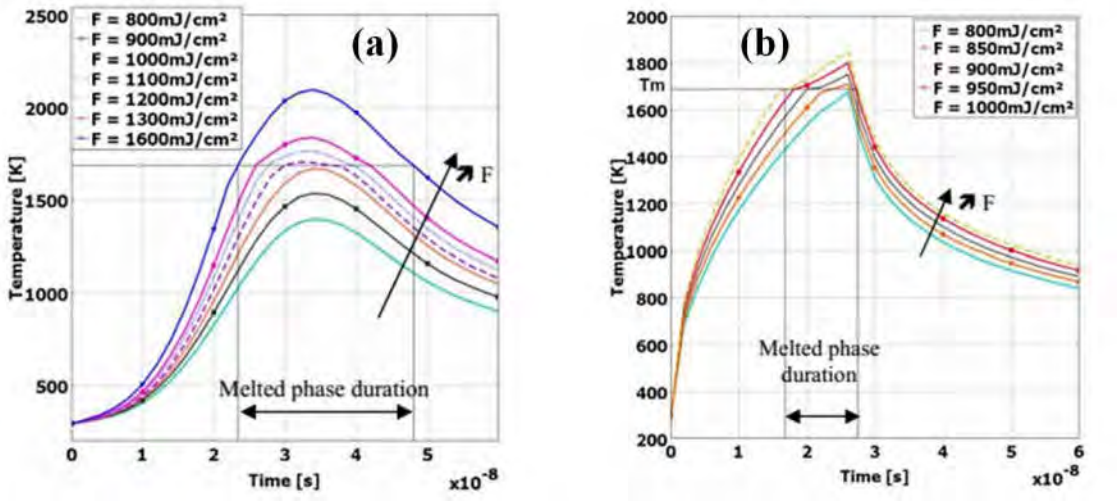

Figure 1-7: Temperature profile modeling on laser annealing of Si for different laser fluences with (a) a Gaussian pulse and (b) a rectangular pulse (from Ref. [35])

Once the laser pulse is absorbed, the heat diffusion into the sample is governed by the thermal diffusivity (D_{Th}) of the material and can be expressed as [34]:

$$\boldsymbol{D_{Th} = \frac{K_{Th}}{\rho C_p}} \qquad \textbf{(9)}$$

The thermal diffusivity, coupled with the time period of the laser pulse, determines the depth to which the material is heated. This can be expressed in terms of the thermal diffusion length (l_{Th}) [32].

$$\boldsymbol{l_{Th} = 2\sqrt{D_{Th}\tau_p}} \quad \textbf{(10)}$$

The thermal diffusion length determines the depth of the heat treatment.

1.3 Phase Transformation: Nucleation and Growth

Most phase transformations proceed with nucleation of the product phase in the parent host and the subsequent growth of these nuclei. Assuming spherical nuclei (treated for simplicity here using isotropic surface energies), the total free energy change (ΔG) for the creation of the nuclei is given by [36]:

$$\boldsymbol{\Delta G = \frac{4}{3}\pi r^3\, \Delta G_V + 4\pi r^2 \gamma} \quad \textbf{(11)}$$

where r: radius of the nucleus, ΔG_V: driving force for nucleation (volume free energy change on phase transformation) and γ: surface energy for the creation of the interface between the parent material and the product nucleus.

Since ΔG_V is negative, this contributes to a decrease in total free energy on phase transformation. However there is a penalty to be paid on creating the new interface, in terms of the surface energy. Hence there is an energy barrier to form stable nuclei. Once stable nuclei form, they grow. The energy barriers are higher for homogeneous nucleation (spontaneous nucleation within the parent matrix), compared to heterogeneous nucleation (nucleation at an existing interface) (equations (12) and (13)) [36]

$$\boldsymbol{\Delta G^*_{Homogeneous} = \frac{16\,\pi\,\gamma^3}{3\,(\Delta G_V)^2}} \quad \textbf{(12)}$$

and,

$$\Delta G^{*}_{Heterogeneous} = \frac{16\,\pi\,\gamma^{3}}{3\,(\Delta G_{V})^{2}}\,f(\theta) \qquad (13)$$

Here,

$$f(\theta) = \frac{1}{4}(2 - 3\,\cos\theta + \cos^{3}\theta) \qquad (14)$$

and is always less than 1, making $\Delta G^{*}_{Heterogeneous}$ lower than $\Delta G^{*}_{Homogeneous}$. Hence, when conditions permit, heterogeneous nucleation is preferred over homogeneous nucleation.

Isothermal crystallization kinetics can be monitored using the Johnson-Mehl-Avrami-Kolmogorov (JMAK) approach [37],[36], where, $\alpha(t) =$ crystallized fraction at time t, can be expressed as:

$$\alpha(t) = 1 - \exp(-K\,(T)\,t^{n}) \qquad (15)$$

Here, n is the growth exponent, and K(T) is the temperature dependent rate; it follows the Arrhenius equation with an activation barrier [36]. Using this equation, the activation barriers can independently be ascertained for nucleation as well as growth. The growth exponent, on the other hand, depends on the growth geometry and the mode of nucleation. For an increasing rate of nucleation with time, n can be greater than 4, while for a decreasing rate of nucleation with time, n is usually between 1 and 4. For a 3-D nucleation and growth, n is 4 in case of a constant nucleation rate, and 3 for growth with pre-saturated nuclei; while, n is 2 for a two-dimensional growth (e.g. lateral and axial growth of a cylindrical rod), and 1 for a one-dimensional growth (radial growth of a plate) [37], [38]. The JMAK equation can be re-written as follows:

$$Ln\left(Ln\left(\frac{1}{1-\alpha(t)}\right)\right) = Ln\left(K(T)\right) + n\,Ln(t) \quad (16)$$

Which yields a straight line between Ln(Ln(1/1-α)) and Ln(t), and the values of K(T) and n can be extracted from the intercept and slope of this line, respectively. PZT crystallization is known to be nucleation limited. Kwok and Desu [26], [39] reported that the nucleation and growth activation barriers for MPB PZT (53/47) are 441 kJ/mol of nuclei (~4.6 eV/nucleus) and 112 kJ/mol of nuclei (~1.2 eV/nucleus) respectively. Furthermore, the nucleation barrier decreases with increasing Ti-concentration (which in turn manifests as decreasing grain size with higher Ti content Figure 1-8).

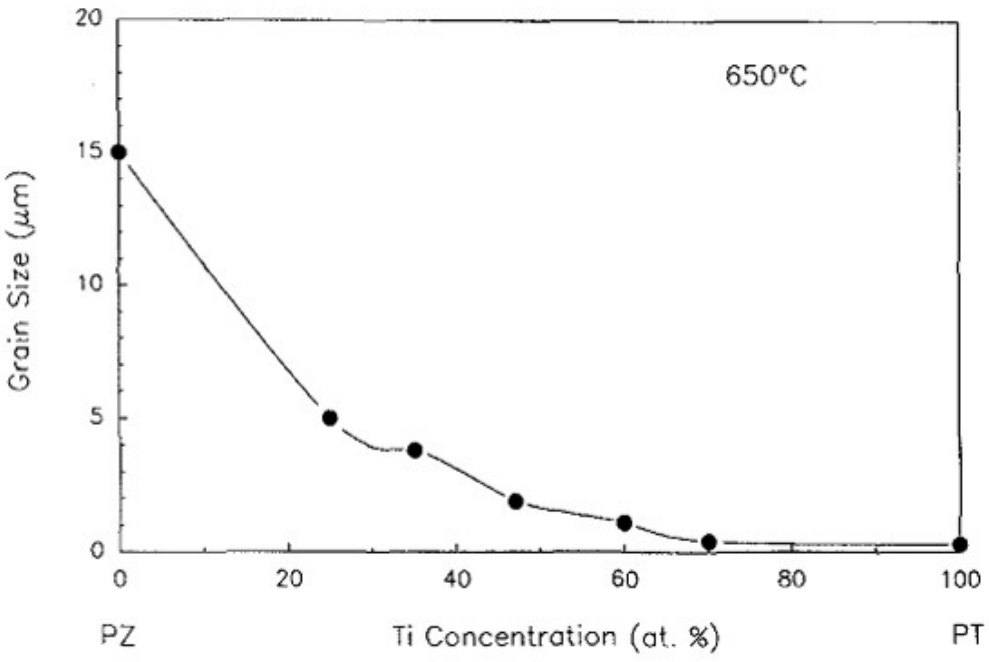

Figure 1-8: Grain size as a function of Ti concentration in PZT thin films prepared using sol-gel technique on $PbTiO_3$ seeded sapphire substrates (reproduced from [26]**)**

1.4 Review of Laser-Induced Crystallization in Multi-component Oxides

Laser processing of silicon thin films has been well studied since the 1980s. Of late, laser irradiation as a means to crystallize amorphous thin films has been extended to multi-component oxide thin films such as lead zirconate titanate (PZT) [40],[41], barium strontium titanate ($(Ba,Sr)TiO_3$; BST) [42],[43], lanthanum manganite ($LaMnO_3$; LMO) [44],[45] bismuth zinc niobate ($Bi_{1.5}Zn_{0.5}Nb_{1.5}O_{6.5}$; BZN) [46], to name a few. In this section, mechanisms involved in laser-induced crystallization will be discussed primarily from the point of view of PZT. Learnings from other material systems will be considered at times, in the absence of the corresponding literature on PZT.

1.4.1 Laser-annealing using Various Laser Wavelengths

As discussed in the section on laser-material interaction, the optical properties of the material at the laser wavelength determine the absorption characteristics. This is an important metric in choosing the right wavelength for the laser processing. The dielectric dispersion in case of crystalline PZT for three different Zr/Ti ratios from Ref. [47] is shown in Figure 1-9. The corresponding optical constants n, k can be extracted using equation (3). The absorption edge for crystalline PZT is around 3.5 eV; thus it is transparent in the visible wavelength range. It is also apparent that PZT has strong absorption at the energy corresponding to the KrF excimer laser, i.e., 4.99 eV (248 nm), which is the photon of primary interest in this work.

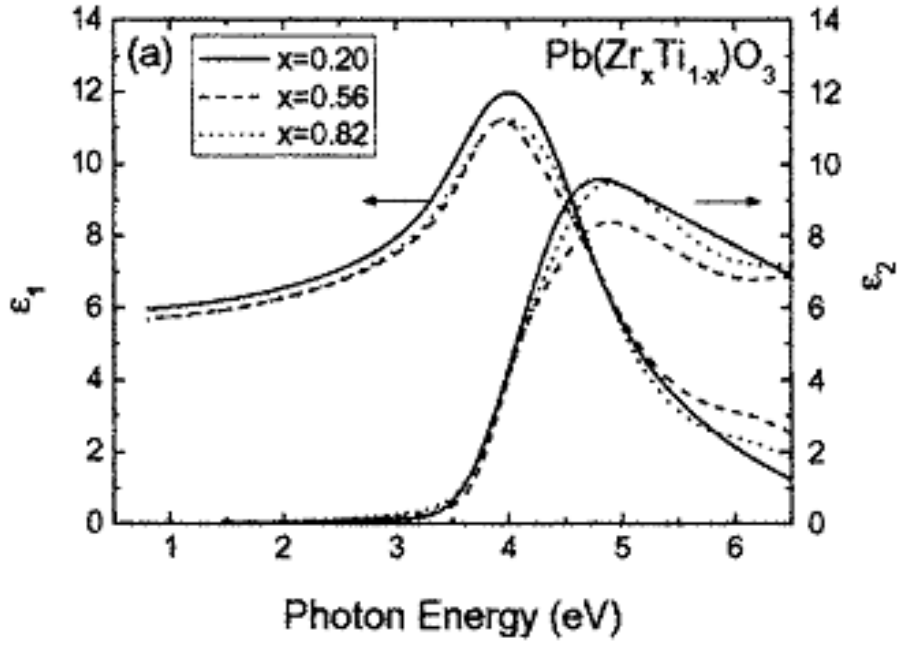

Figure 1-9: Dielectric functions for PZT (various compositions) from Ref. [47]

Excimer lasers are, in general, attractive for laser-induced crystallization of electroceramics as heat treatment is possible for large areas, which increases the throughput [34]. Furthermore, the duration of the heating cycle is small (10's of nanoseconds), which should reduce heating of the underlying substrate. In early reports on laser annealing of PZT films with KrF excimer laser (wavelength: 248 nm), [40], the authors opined that obtaining the perovskite phase directly from amorphous/pyrochlore phase is difficult because of the following reasons:

- There is a low ablation threshold for PZT (of the order of 1 J/cm^2. In contrast, Si is known to be annealed at much higher energy densities)
- PZT has a thin absorption depth for 248 nm wavelength, and hence prevents crystallization of large thicknesses

- As already discussed, there is a high nucleation energy barrier for PZT compared to the growth barrier

In that work, the films were first furnace annealed in the temperature range: 470˚C to 550˚C (the lower temperature for PZT (20/80) composition while higher temperature for PZT (53/47)) to nucleate the perovskite phase, and grain-growth was accomplished using laser annealing at room temperature. A KrF excimer laser was also used by the authors in Ref. [48] where a 600 nm PZT film was reported to have been crystallized to a depth of about 120 nm (Figure 1-10). It has to be kept in mind that increasing the laser energy density above a certain threshold value can cause melting [6]. This would be expected to be particularly problematic in PZT since the melting is incongruent [49].

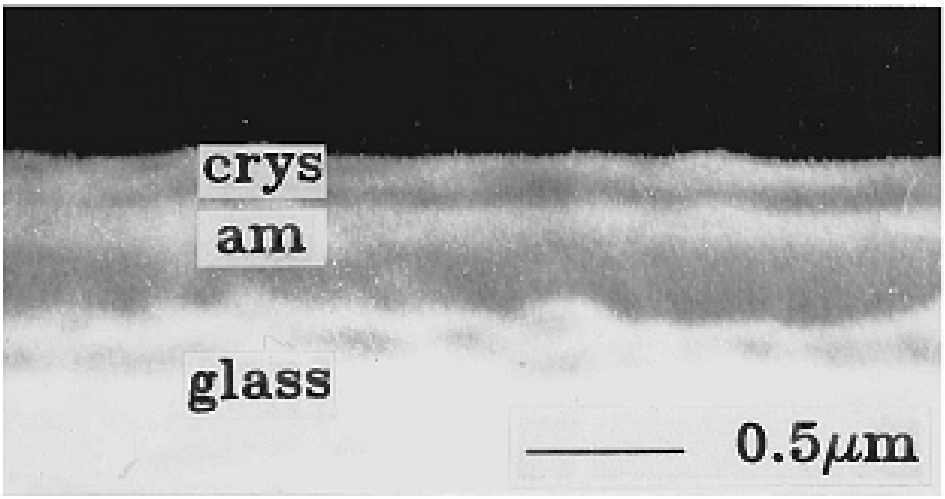

Figure 1-10: Cross-section of a ~600 nm PZT (44/56) film crystallized using a KrF excimer laser (from Ref. [48]**). The crystallized thickness is 120 nm (crys: crystallized layer, am: amorphous layer).**

There are reports of utilizing longer laser wavelengths (to increase the penetration depth). In Ref. [50], PZT (44/56) thin films were crystallized on glass substrates maintained at room temperature by scanning with an Ar laser (488 nm wavelength). Although crystalline

PZT is known to be transparent at this wavelength (see Figure 1-9), their amorphous PZT films had a transmittance of around 30%. Thus, part of the energy could be absorbed. The utilization of longer wavelengths partially overcomes the limited thickness crystallization achievable using excimer lasers and will be further discussed in the later part of this chapter.

1.4.2 Transient Temperature Profiles Due to Laser Heating

The limited crystallization depth observed for PZT crystallization with excimer lasers can be explained in terms of the transient temperature profiles experienced due to the pulsed laser heating. The authors in Ref. [41] simulated the temperatures at several depths of a PZT (300 nm thick)/Pt/Ti/SiO_2/Si stack on irradiation with a single laser pulse (248 nm wavelength, 20 ns pulsewidth, and energy density ~40 mJ/cm^2) as shown in Figure 1-11. It is clear that the depths of the material experience lower maximum temperatures, limiting crystallization.

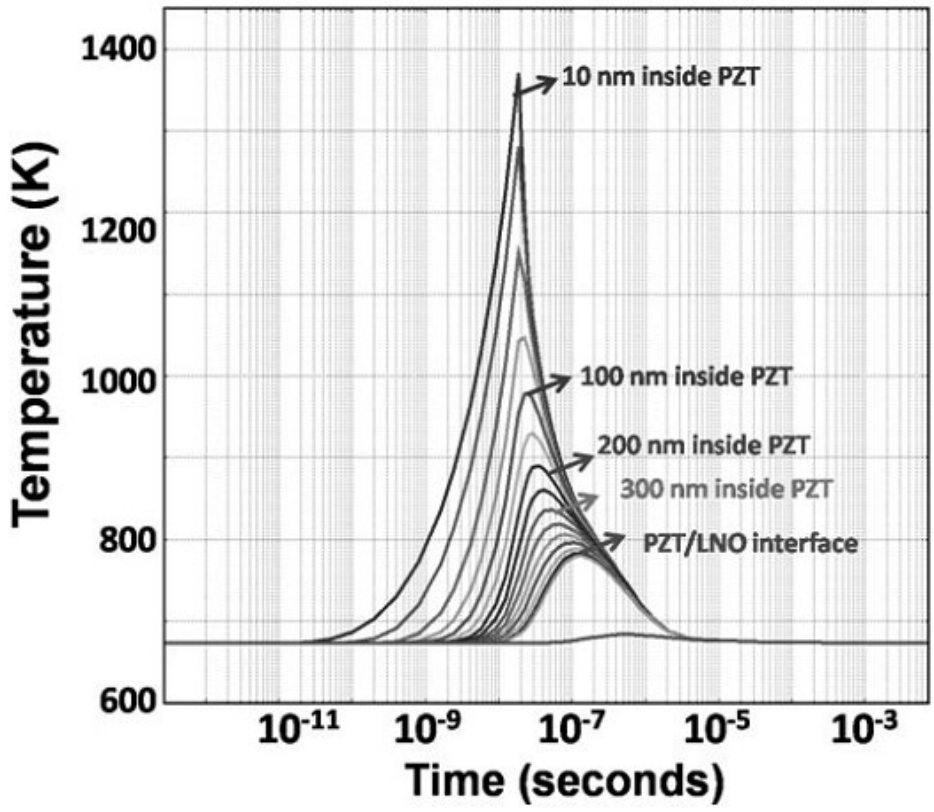

Figure 1-11: Transient temperature profiles at various depths in a PZT (300 nm thick)/Pt/Ti/SiO_2/Si stack for 248 nm wavelength, 20 ns pulsewidth, and energy density ~40 mJ/cm^2 (from Ref. [41]**)**

Owing to the high temperatures achieved at the surface, top-down crystallization of the films is expected. However, if the nucleation energy at the film-substrate interface can be brought down, either by using a suitable substrate with lattice matching or by using a seed layer, then nucleation from the substrate can be preferentially achieved [51]. This is particularly important when control of the film crystallographic orientation is required. In Ref. [51], the authors produced {100} textured 300-350 nm thick PZT (52/48) using pulsed KrF excimer laser annealing by utilizing a 10-15 nm thick {100} oriented $PbTiO_3$ seed layer. Optical absorption by the substrate (if the film on top is either semi-transparent or is

thinner than its optical penetration depth), could also favor nucleation at the substrate –film interface [44].

A set of experiments on laser annealing (with thermal simulations to understand the process) was performed by Waser et al. [42], in the barium strontium titanate (BST) system. The authors deduced that on exposure to a large number of pulses exceeding a certain energy density, the films should crack due to the thermal stresses. Hence, according to authors in [42] there exists a window in terms of the energy density and number of annealing pulses for crystallization that enables high atom mobility, while preventing cracking (Figure 1-12).

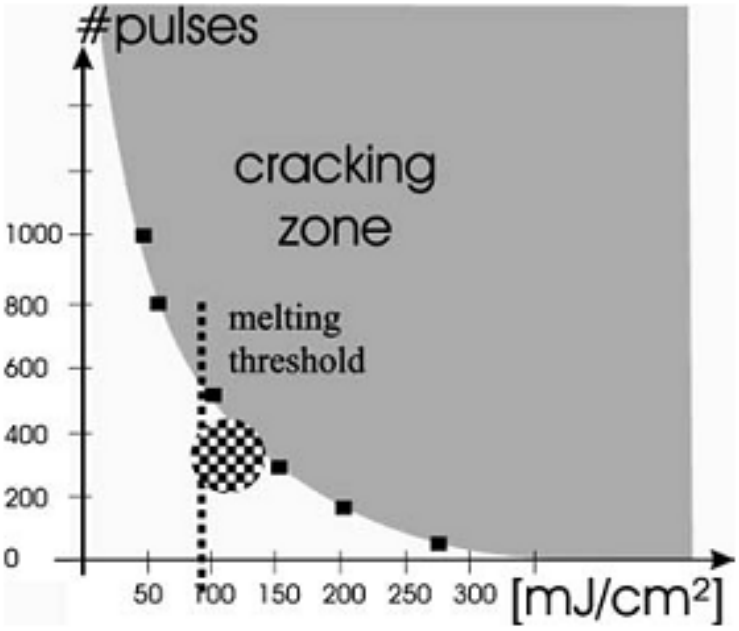

Figure 1-12: Number of pulses vs. energy density showing the melting threshold and the propensity for cracking in case of KrF excimer laser annealed 130 nm thick BST films deposited by chemical solution deposition on platinized silicon substrates (reproduced from Ref. [42]**)**

The effect of film thickness on laser heating of the film was also simulated in [42] (Figure 1-13). It was estimated that, with a reduction in film thicknesses, the film surface temperatures drop (although the interface is exposed to higher temperatures). This lowering of the surface temperatures has been attributed to the underlying thermally conducting substrate (such as Si or a metal electrode) acting as a heat sink. The interface temperatures will control damage to any underlying layers.

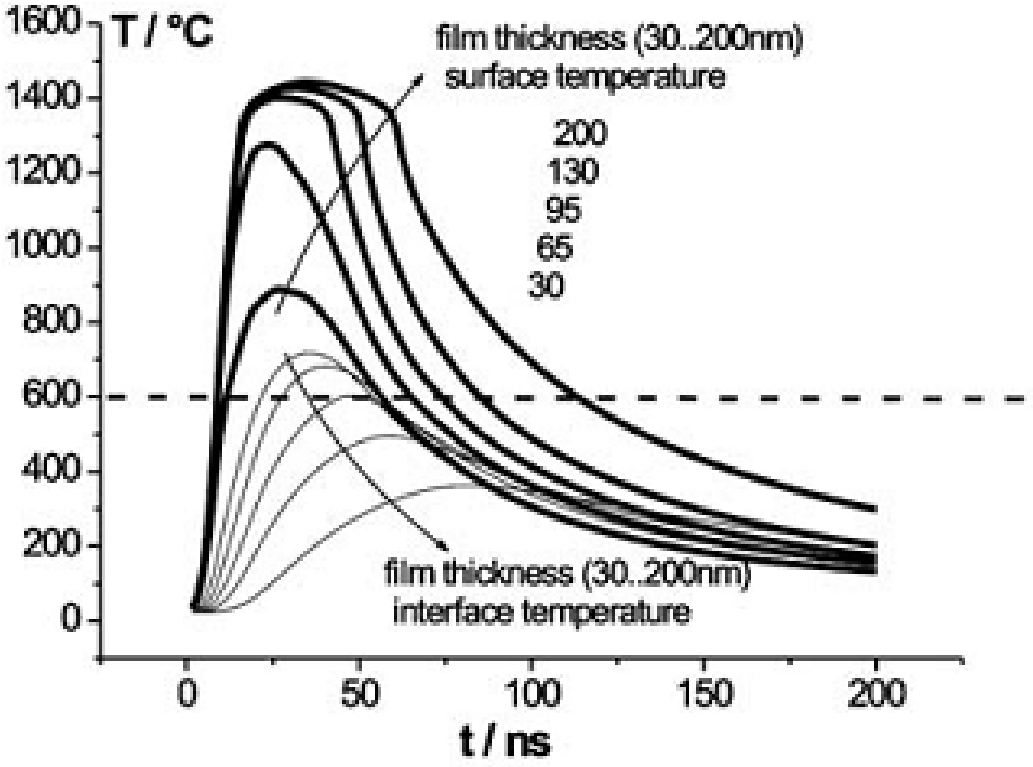

Figure 1-13: Thickness dependence on the surface temperatures in case of laser annealing of BST thin films on platinized silicon (From Ref. [42]**)**

1.4.3 Effect of Photochemical Processes

Photochemical processes can also influence crystallization kinetics by laser annealing when the bond energies are lower than the photon energy. The authors in [52] crystallized

$Ba_{0.8}Sr_{0.2}TiO_3$ thin films using 266 nm radiation (4.7 eV; Nd:YAG laser). The corresponding bond dissociation energies for the various bonds were considered and are as follows: Ba-O: 5.9 eV/bond, Sr-O: 4.7 eV/bond and Ti-O: 6.9 eV/bond. The authors suggested that the dissociation energy of the Sr-O bond was comparable to the energy of the radiation used (the rest were of higher energy than the photon energy), and hence was amenable to direct chemical decomposition by light, contributing to photoelectronic/photochemical mechanisms of laser-material interaction. However, on the other hand, in the case of crystallization $Ce_{0.9}Zr_{0.1}O_{2-y}$ thin films using 266 nm radiation (4.7 eV) [53], the corresponding bond dissociation energies for Ce-O and Zr-O bonds are 8.3 eV/bond and 7.9 eV/bond and are considerably higher than the photon energy. The authors suggest that the bond energies might be lower at defects, and hence photochemical reactions cannot be completely ruled out. Moreover, in [44], the authors speculate that the epitaxial growth of $LaMnO_3$ from the substrate ($SrTiO_3$ or $LaAlO_3$) is initiated by a photochemical effect wherein dangling bonds on the substrate surface are photoactivated, while the photothermal heating gives rise to ion-migration causing crystallization.

For PZT the relevant bond energies are Pb-O: 378 kJ/mol: 3.9 eV/bond, Ti-O: 662 kJ/mol: 6.9 eV/bond and Zr-O: 760 kJ/mol: 7.9 eV/bond [54]. Here, with 4.99 eV photons in case of KrF laser, the Pb-O bonds can be disassociated and may contribute to the crystallization kinetics.

Photochemical reactions with residual carbon in the material should also be considered. In Ref. [55], direct irradiation with ArF excimer laser at high energy densities caused roughened surfaces due to violent photochemical reactions with the metalorganic

compounds. Hence, a two-step process was successfully used to produce "defect free" PZT films:

1. 25 mJ/cm^2 at 25 Hz for 1 min and then
2. 80-90 mJ/cm^2 at 10 Hz for 1 min

1.4.4 Through-Thickness Crystallization by Laser Annealing

Various methods to improve through-thickness crystallization have also been studied to crystallize the whole sample depth instead of just the top surface. Increasing the dwell time of the individual laser pulses by extended-pulse laser annealing [6] has been proposed to increase the depth to which material can be heated. In [6], KrF excimer laser pulses with 25 ns pulsewidth were stretched to 374 ns using pulse-extender optics and were used to completely crystallize PZT thin films on $LaNiO_3$ coated $Pt/Ti/SiO_2/Si$ substrates. The substrate temperature was maintained at room temperature during laser annealing. Simulations of laser heating using extended laser pulses (Figure 1-14) indicated a lowering of the surface temperatures, and an improved uniformity of the temperature distribution through the depth of the film. The authors were, however, unable to nucleate the perovskite phase in amorphous PZT thin films. It should be noted that, however, increasing the pulse-length would also lead to a corresponding increase in the temperatures seen by the substrate, so a balance in thermal budget has to be maintained to minimize the damage to the substrate.

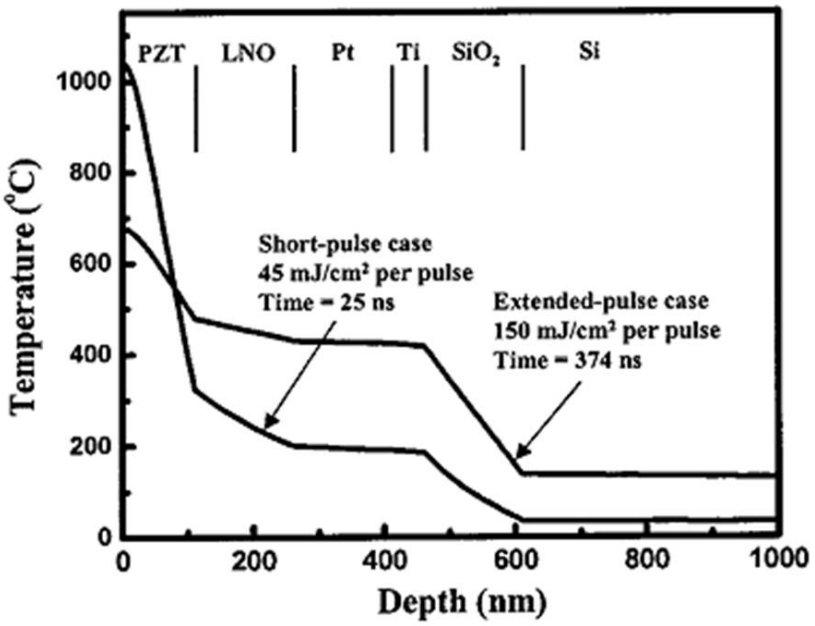

Figure 1-14: Improved uniformity of the heating through the depth of the film by extended pulse laser annealing ([6]**)**

560 nm CW (continuous wave) laser (~2.2 eV) has also been used to crystallize thick PZT films. The starting point was an aerosol deposition (AD) or granule spray in vacuum (GSV) film with coexisting amorphous and nanocrystalline phases [56]. The longer wavelengths imply a higher penetration depth of the beam, although it is not clear what mechanism was used for absorption (Figure 1-15). It is possible that scattering at grain boundaries or inclusions caused absorption in intrinsically transparent materials [33].

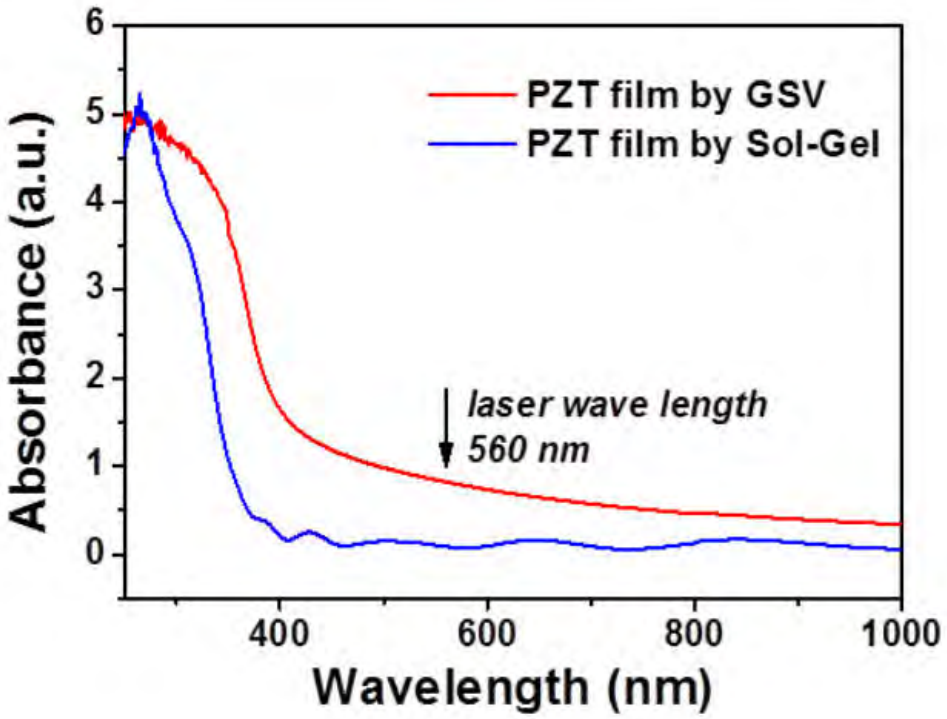

Figure 1-15: Absorption spectra of PZT prepared by two different techniques demonstrating non-negligible absorption in the visible wavelength range for GSV coated films compared to a sol-gel film (From Ref. [56]**)**

1.4.5 *In Situ* Laser Annealing

Laser irradiation during thin-film growth of multi-component oxides has also been utilized. The authors in [57] used ArF excimer laser irradiation on a growing $YBa_2Cu_4O_7$ (YBCO) surface to enhance crystallization. This technique should enable the thickness limitation on crystallization to be overcome, while maintaining low substrate temperatures. Laser-induced crystallization during growth in the lead titanate ($PbTiO_3$) system was attempted by H. Tabata et al. [58], [59] to produce crystalline $PbTiO_3$ thin films at 350°C substrate temperature on $SrTiO_3$ and Pt/MgO substrates. In Ref. [59], the authors used two separate laser sources, one for ablation and the other for irradiation of the sample, the advantage

being that the annealing pulses could be timed with respect to the arriving deposition species (Figure 1-16). Timing the annealing laser pulses to arrive 1 μs after the ablation laser pulse was seen to improve the crystallinity of the sample compared to either 0 μs or 10 μs delay, for the same irradiation energy. The 1 μs delay could be of the order of the time of flight (TOF) of the plume species from the target to the substrate, while the absorption of the laser energy directly by the plume could give rise to improved adatom mobility causing the improved crystallinity [59]. However, since the thermal energy provided by the laser is sufficient to crystallize the films, it's not clear how much more advantage timing the pulses actually provides.

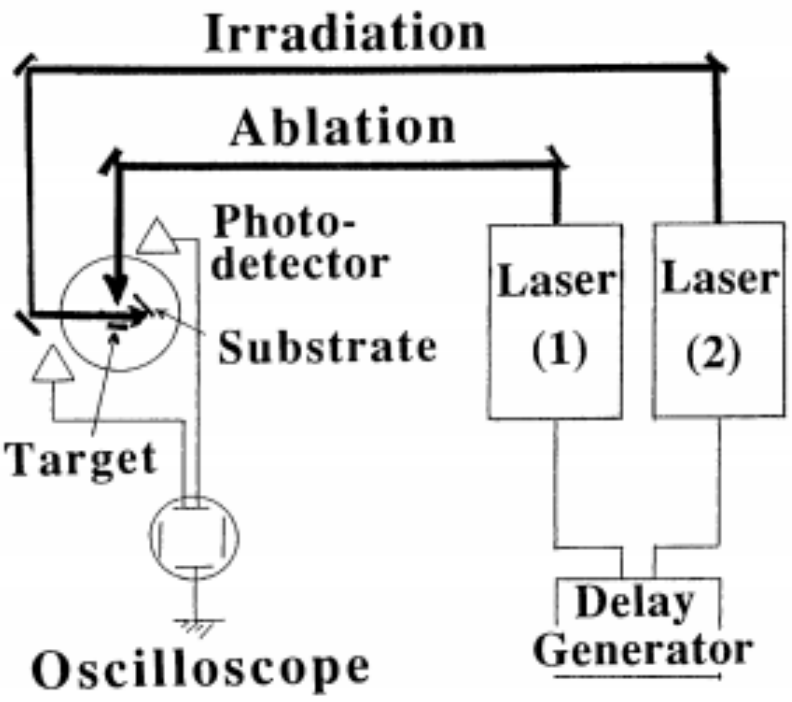

Figure 1-16: Simultaneous laser annealing with two lasers (one for ablation and the other for sample irradiation) (reproduced from Ref. [58], [59]**)**

The goal of this thesis is to develop an understanding of the process and challenges associated with laser annealing of amorphous PZT films in order to integrate crystalline ferroelectric PZT thin films with polymeric base substrates, at substrate temperatures below those causing substrate degradation. At such temperatures (close to 200°C), there are no chances of any pre-existing nuclei in the films due to an earlier processing step (e.g., film pyrolysis at around 350 - 400°C). Furthermore, in order to demonstrate the possibility of low substrate temperature *in situ* crystallization during growth, a pulsed laser deposition system integrated with laser annealing was designed and constructed. A thorough microstructure-processing-property relationship is lacking for most of the low temperature growth techniques. Thus, this thesis aims to establish insights into the integrated process. Chapter 2 provides the experimental details on the various growth and characterization techniques utilized in this work. Accompanying this, a detailed description is provided on the implementation of a system that enables *in situ* laser annealing during growth of multi-component oxides. Chapter 3 establishes laser induced crystallization as a route to obtain ferroelectric PZT thin films on polymeric base substrates, while Chapter 4 provides proof of concept of *in situ* laser annealing of PZT films at substrate temperatures below 400°C, in order to produce films of comparable quality to conventional high temperature processes. Chapter 5 explores microstructures and their evolution mechanism typical of the *in situ* laser annealing process. Chapter 6 concludes the thesis, and suggests directions for future work.

Chapter 2 Experimental Procedure

This chapter describes the procedures used to deposit, crystallize, and characterize lead zirconate titanate, PZT, thin films. Two different physical vapor processes were used to deposit the films (sputtering and pulsed laser deposition (PLD)). Pulsed-laser annealing was utilized to obtain crystallization at low substrate temperatures; this will be explained alongside the simulation method for the associated transient thermal heating. Additionally, the design and setup of a tool which combines pulsed laser deposition and laser annealing processes for growth of crystalline multi-component oxide thin films will be detailed. Characterization of structural/microstructural properties of the thin films using x-ray diffraction (XRD), scanning electron microscopy (SEM) and transmission electron microscopy (TEM) techniques will also be outlined. Finally, optical, electrical and piezoelectric measurements will also be discussed.

2.1 Deposition and Laser Annealing

Two techniques were used to deposit amorphous PZT films for this work: RF magnetron sputtering and pulsed laser deposition (PLD). Conventional crystallization was achieved using rapid thermal processing while crystallization at low substrate temperatures was accomplished using pulsed laser annealing. Chemical solution deposition (CSD) was not used as a primary deposition technique (except for uniform crystalline seed layers used in part of this work), as full removal of organics is difficult at the low process temperatures (<~350°C) utilized in the majority of this work. Finally, a vacuum deposition system with

laser optics to enable simultaneous pulsed laser deposition and pulsed laser annealing was employed.

2.1.1 RF Magnetron Sputtering

RF magnetron sputtering is a physical vapor deposition (PVD) technique for thin film growth of insulating targets such as oxides [60], and was used in this work for the growth of PZT thin films. For growth on polymeric substrates, amorphous thin films were sputtered (using the Kurt J. Lesker CMS-18 system shown in Figure 2-1) from a PZT (30/70) ($Pb(Zr_{0.30}Ti_{0.70})O_3$) target with either 10% or 20% excess PbO at room temperature. The excess PbO was used to compensate for Pb-losses during thermal processing. The primary sputtering parameters used in this work are tabulated in **Table 2-1**. Specific process optimization is given in Chapter 3.

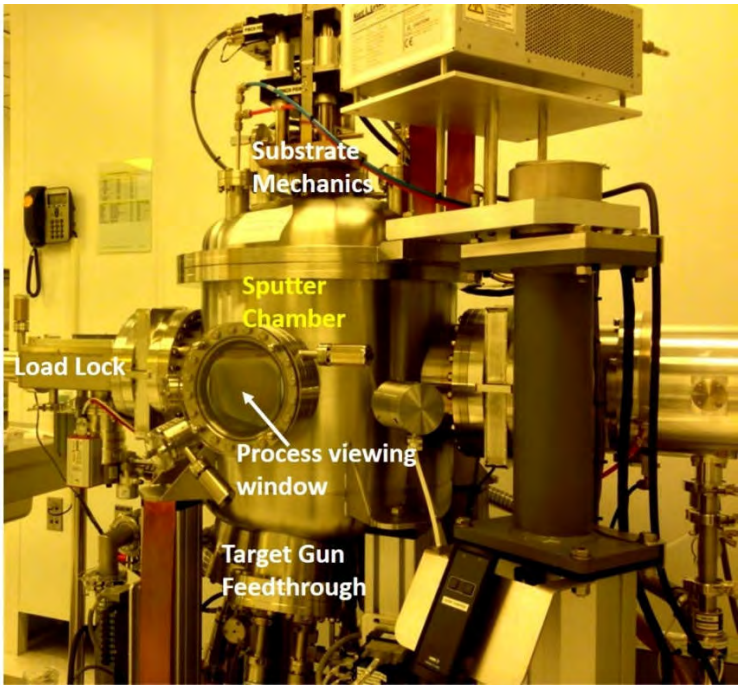

Figure 2-1: RF magnetron sputtering tool used to deposit PZT thin films

Table 2-1: PZT thin film sputtering parameters used in the work

Sputtering Parameter	RF Sputtering Condition
Target Composition	**$Pb(Zr_{0.3}Ti_{0.7})O_3$ + 10% Pb/20% Pb +1% Nb**
RF Power Density	**2.0 W/cm^2**
Target-Substrate Distance	**120 mm**
Substrate Temperature	**25˚ C**
Sputtering Gas	**Ar**
% pO_2	**0**
Working Pressure	**3 -9 mTorr**
Deposition time	**2500 s (~100 nm), 7500 s (~300 nm)**

2.1.2 Pulsed-Laser Annealing

Pulsed-laser annealing of the deposited films was carried out using a KrF excimer laser (COMPex Pro 102F, Coherent Inc., 248 nm wavelength, 20 ns pulse width, maximum energy 400 mJ/pulse). The beam dimensions at the laser output are 2.4 cm (vertical) by 0.8 cm (horizontal). A schematic of the laser annealing setup is shown in Figure 2-2. The horizontal dimension of the laser beam was defocused using a cylindrical plano-convex lens of focal length 10 cm to achieve the required energy densities (range 30 – 80 mJ/cm^2) at the sample surface. The annealing was carried out in a vacuum chamber (described in Ref. [61]). The samples were mounted onto the substrate heating block using the Leitsilber Conductive Silver Cement from Ted Pella, Inc. The silver cement was cured at 100°C for

about 5 minutes. After alignment of the sample with respect to the laser beam, the chamber was first pumped down to a base pressure of <2 X 10^{-5} Torr. Consequently, either a 10% O_3/90% O_2 or a pure O_2 ambient was introduced, while heating the sample to the required substrate temperature (200°C – 375°C). Finally, the laser was pulsed at either 10 Hz or 20 Hz for the required experimental irradiation duration, and at a given ambient pressure (typically 50 mTorr).

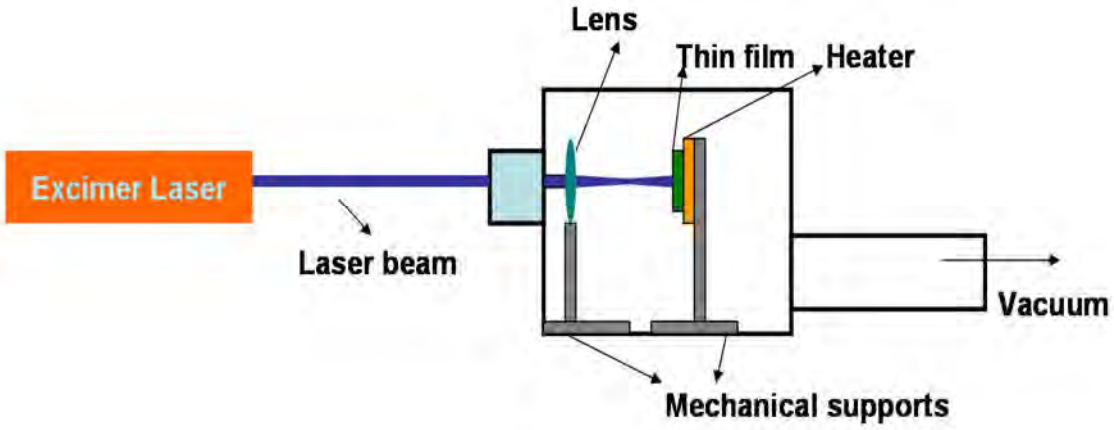

Figure 2-2: Schematic of the laser annealing setup

2.2 Modeling of Transient Heating due to Laser Annealing

Photothermal heating due to a single laser pulse was modeled using the finite element method in COMSOL 5.0 Multiphysics software. Finite element modeling of the laser-induced heating was performed using the 1-D heat equation (1).

$$\rho C_p \frac{\partial T(z,t)}{\partial t} = \vec{\nabla}.\left(K_{Th}\vec{\nabla}T(z,t)\right) + Q(z,t) \qquad (1)$$

Here, ρ: density, C_p: specific heat, T: temperature, t: time, K_{Th}: thermal conductivity. Q is the heat source distribution in the sample as a function of depth (z), which in turn can be expressed in terms of the laser intensity (I_o), the reflectivity of the surface (R) and absorption coefficient of PZT (α) as [33]:

$$Q(z,t) = I_o(t)(1-R)\,\alpha \exp(-\alpha z) \tag{2}$$

The time evolution of the laser pulse intensity profile (I_o) was modeled with a Gaussian-like function as follows:

$$I_o(t) = \left(\frac{F}{\tau_p}\right)\exp\left[-4\ln 2\left(\frac{t-2\tau_p}{\tau_p}\right)^2\right] \tag{3}$$

where F: laser fluence, and τ_p: pulsewidth (Full Width at Half Maximum) of the laser

The reflectivity, $= \frac{(n-1)^2+k^2}{(n+1)^2+k^2}$ and the absorption coefficient, $\alpha = \frac{4\pi k}{\lambda}$ were extracted from the complex refractive index $\tilde{n} = n + ik$ of PZT at the laser wavelength (measured using spectroscopic ellipsometry).

A model of the 2-D stack of the various layers was first constructed using the corresponding layer thicknesses (Figure 2-3(a)). Since, in a 1-D heat diffusion model, the dimensions along the direction perpendicular to the flow of heat are not important, the width of the layers were arbitrarily fixed to 1 micron. Since the beam dimensions (1 - 3 cm) are much larger than the heat diffusion length in material (~169 nm [41]), a 1-D heat flow model is applicable [32]. The material properties listed in Table 2-2 were used for the modeling. Thermal properties for PZT were taken from Ref. [41]. Certain caveats should be mentioned regarding the modeling. The temperature dependences of the various material

properties have been neglected for these calculations (in most cases they are not known), as was any latent heat due to a phase transition. The properties of PZT (52/48) and the PZT (30/70) seed layer were also assumed to be similar. Hence the simulated temperature profiles are only a guide to the actual temperature distributions.

Table 2-2: Material properties (taken from Ref. [41]**,** [62]**)**

	ρ (kg/m^3)	**K_{th} (W/(m.K)**	**C_p (J/(kg.K))**
PZT	7500	1.8	370
Pt	21450	69.1	134
Ti	4500	17	528
SiO_2	2200	1.6	740
Si	2330	152	700

A triangular mesh element was used for the 2D finite element modeling (Figure 2-3(b)). A fine meshing was used for the thin layers while a coarse meshing was utilized for the thick substrate.

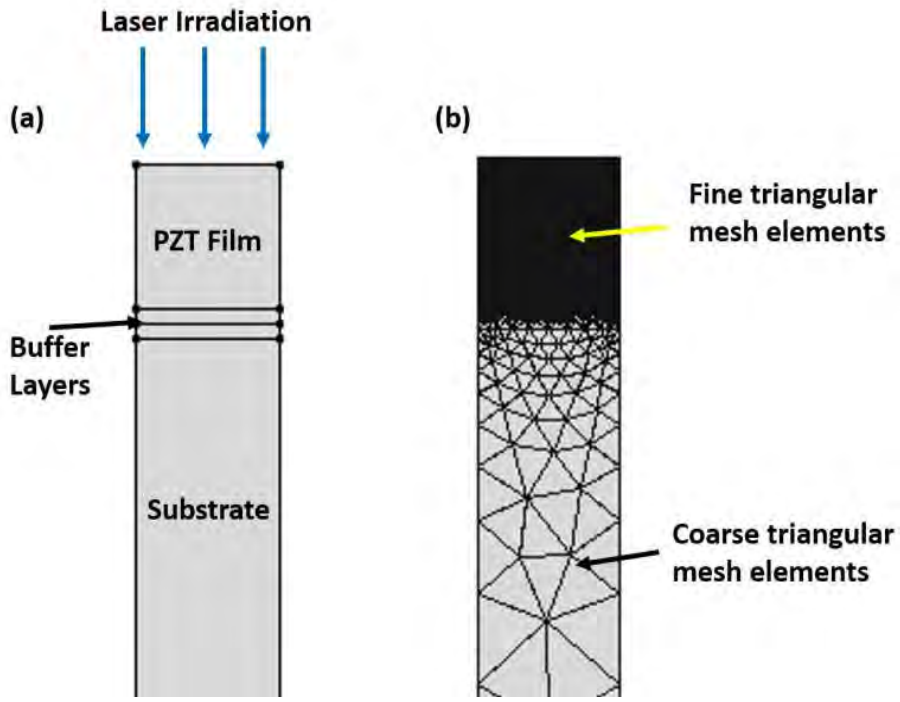

Figure 2-3: Layer geometry (a) and triangular mesh elements (b) for finite element modeling (COMSOL™). In this example, the PZT film thickness was 1 micron.

2.3 *In Situ* Pulsed Laser Annealing System

As discussed in Chapter 1, thin films of various multi-component oxides (such as PZT, BST, LMO, BZN etc.) that typically require high processing temperatures can be crystallized from their amorphous state by laser irradiation at low substrate temperatures, enabling their integration with temperature sensitive systems. However, such an *ex situ* laser processing technique is fraught with limitations in terms of thermal penetration depth. *In situ* crystallization during growth overcomes this constraint. To this end, a pulsed laser deposition (PLD) system capable of simultaneously carrying out the two functionalities of growth and laser irradiation of the growing film was designed and constructed as part of this work. Again, a single 248 nm KrF excimer laser with a 20 ns pulse width, 20 Hz

repetition rate and a maximum energy 400 mJ/pulse was utilized to carry out the two functions of ablation of the multi-component oxide target and annealing of the growing thin film. The following sections describe the design of the vacuum chamber, vacuum system, the substrate heater and the optics. A schematic of the process is shown in Figure 2-4. The design of the system was carried out by Austin Fox.

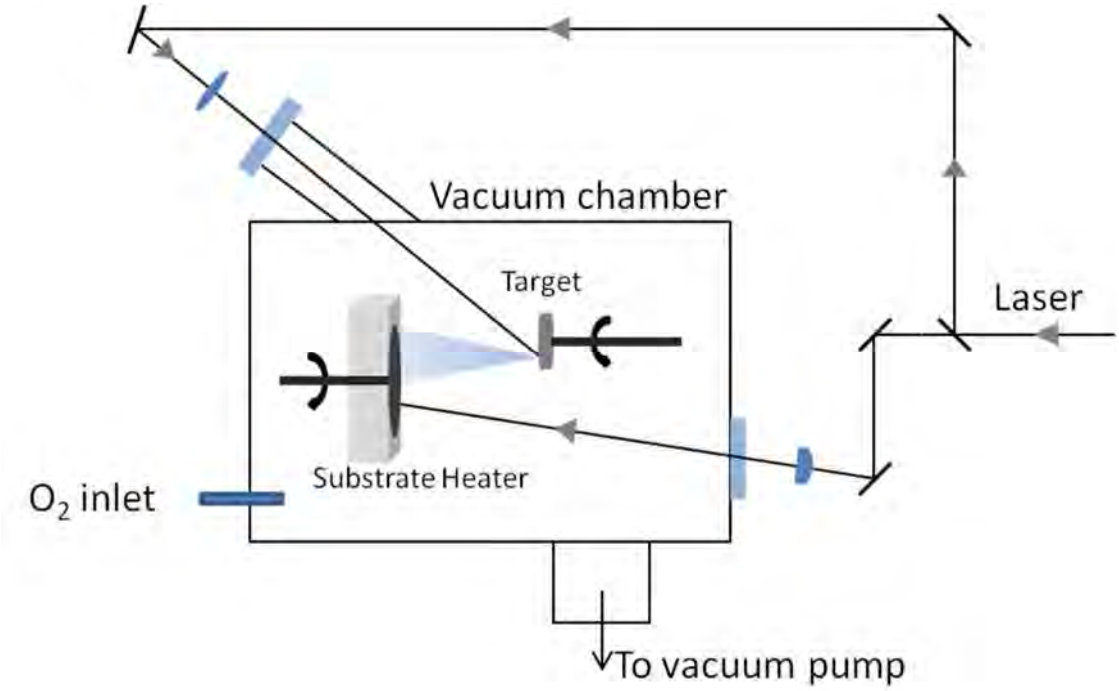

Figure 2-4: Schematic of the *in situ* laser annealing system

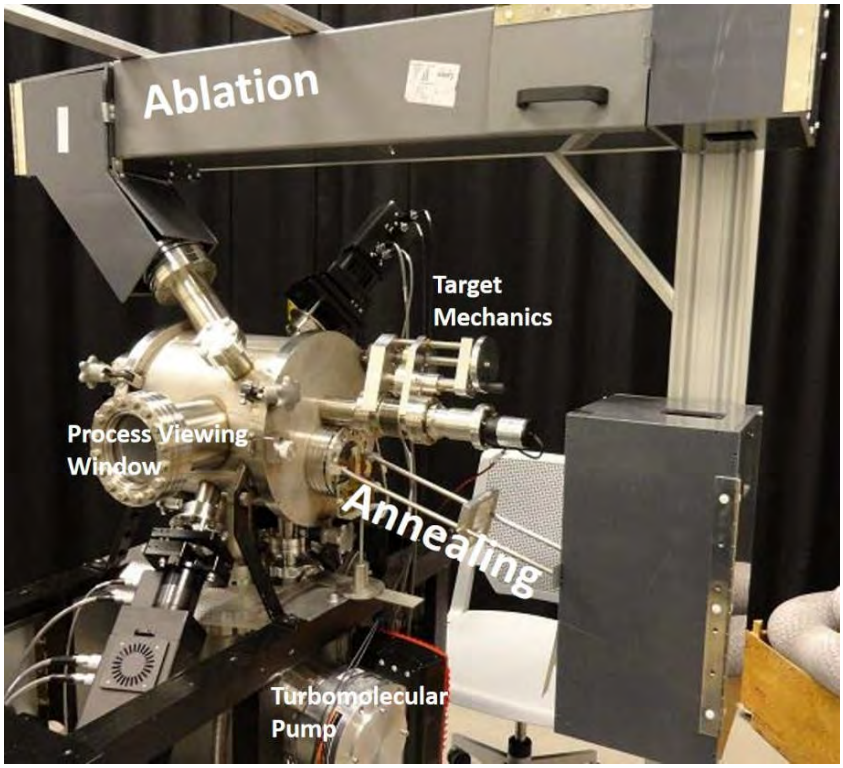

Figure 2-5: The *in situ* laser annealing setup

2.3.1 Vacuum System

A 10" inner diameter cylindrical vacuum chamber with doors on either end (Figure 2-6) was designed and constructed to accommodate the two laser beams (ablation and annealing), and also to allow for system pumping, pressure monitoring, gas delivery, target and substrate mechanics, substrate heating, real time process monitoring and process viewing. Summarized here are the various flanges utilized in the chamber design. The chamber (Figure 2-6 (a)) consists of two hinged doors for access to the interior (substrate alignment/loading, target mounting, laser energy measurement etc.) that are o-ring sealed. Attached to the door on the substrate side of the chamber are five CF (ConFlat) 2.5" flanges in order to facilitate the substrate mechanics feedthrough, the substrate heating power

feedthrough, the cooling lines and a thermocouple feedthrough for temperature measurement. The target side door for the chamber allows for the target mechanics feedthrough (CF 2.5" flange) and a CF 4.5" flange for the annealing laser beam entry port. These two ports are slightly offset from the central axis of the cylindrical chamber. The cylindrical surface of the chamber itself has an ablation laser beam entry port (a CF 4.5" flange aligned at 45° to the surface and pointing towards the target). On one side, (Figure 2-6 (b)) is a CF 6" flange for a glass window used as the process viewport, and a CF 2.75" for shining a flashlight into the system (again, to facilitate process viewing). On the other side, (Figure 2-6 (c)) are lumped together four CF 2.75" ports for gas inlet, vacuum gauges (convection, ionization gauges). Underneath are a CF 2.75" and CF 6" flanges for installation of roughing and turbomolecular pump lines. The chamber is also equipped with two CF 2.75" flanges for the installation of real time spectroscopic ellipsometry (RTSE) tool, in order to enable real time process monitoring. These ports are aligned in such a way that each one individually makes an angle of 75° to the substrate surface plane normal.

An STP-iX455 Turbomolecular pump (TMP) with magnetic levitation (operating at 55000 rpm, pumping speed of 300 ls^{-1}) from Edwards Vacuum, Inc, Hillsboro, Oregon, was utilized to reach a base pressure of about 8×10^{-7} Torr in the chamber. The base pressure was measured using a Bayard-Alpert ionization gauge (IGM400 Hornet^{TM} from Instrutech, Inc., Colorado). The TMP was backed by an XDS-10 Dry Pump (Edwards Vacuum, Inc.) capable of a maximum pumping speed of 11.1 m^3/hr. The backing pressures achieved were of the order of 8×10^{-3} Torr. The roughing of the vacuum chamber was also achieved by the same pump. In order to do this, the dry pump line was split into two (one for backing the TMP, and the other for the operation of the foreline (roughing)). Correspondingly,

backing and roughing valves were also installed for switching between the two lines as required.

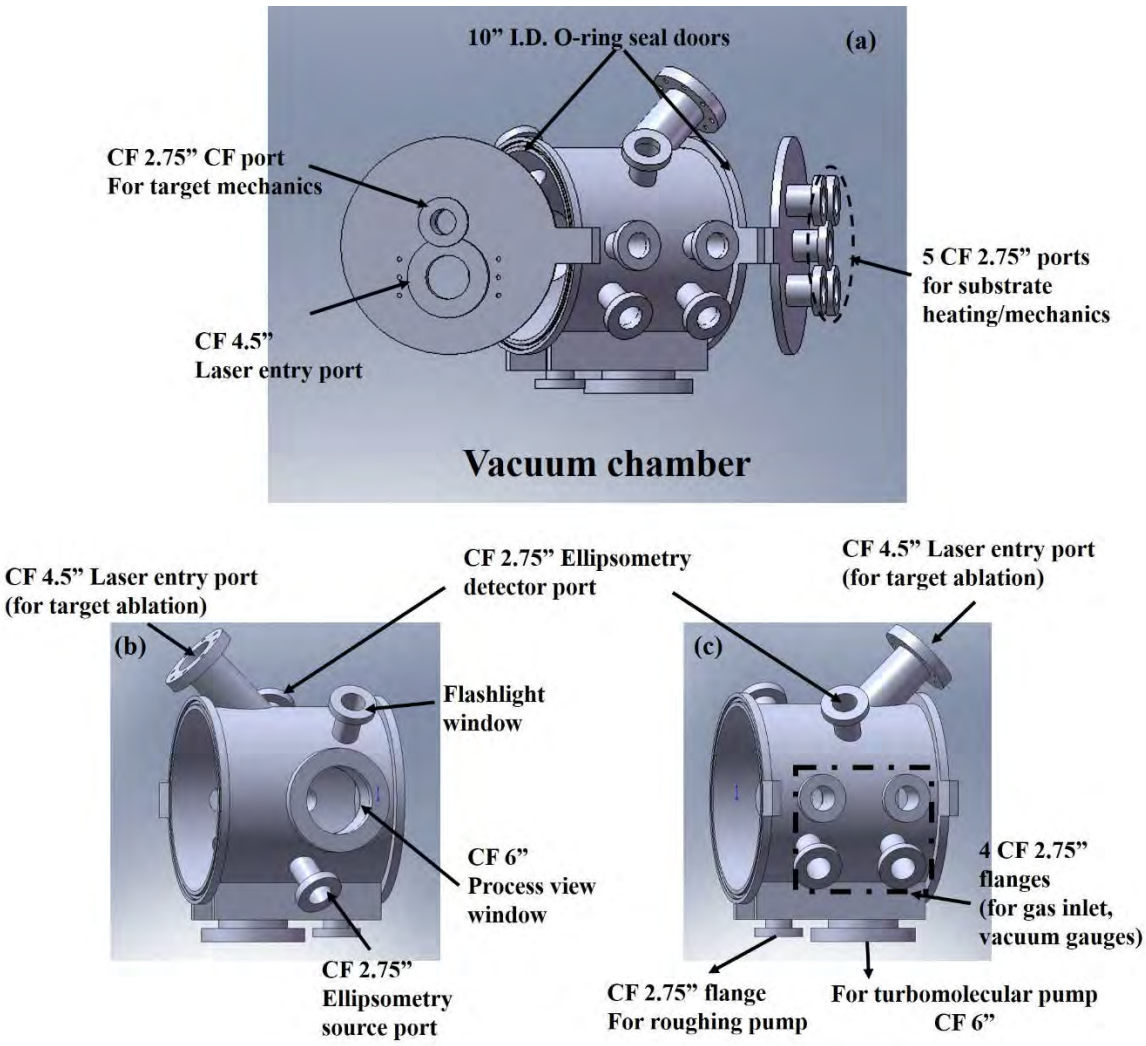

Figure 2-6: Vacuum chamber with ports serving various functionalities. (a) represents the vacuum chamber with the doors attached. (b) and (c) represent the views of the main cylindrical chamber from two different sides. The various ports have been labeled.

The ambient gas to the chamber was fed through an ozone generator capable of producing 10% O_3/90% O_2 (using an ultra-high purity (UHP) oxygen source gas). A flow rate of ~50

sccm was utilized (set using an MKS model 179A mass flow controller from MKS Instruments, Wilmington MA). Deposition pressures were controlled by constricting the gate valve between the deposition chamber and the TMP. A convection Pirani gauge (CVG101 Worker Bee, Instrutech, Inc., Colorado) was used to read the pressure values during the deposition process.

2.3.2 Substrate Heater

A custom substrate heating system was designed and constructed in order to maintain a finite substrate temperature during deposition (design shown in Figure 2-7). The heater case was made from 304 stainless steel, while the reflecting mirror surface was also prepared from a one side polished 304 stainless steel. Type 304 stainless steel was used owing to its oxidation resistance and low concentrations of molybdenum (compared to e.g., 316 stainless steel). The presence of molybdenum would be deleterious, as it can oxidize at high temperatures, forming volatile oxides, compromising the structural stability of the heater [61]. 500W (120V) halogen lamps from USHIO were utilized for the heating, and substrate temperatures up to about 415°C could be achieved. The installed substrate heater assembly (with the rotatable substrate plate) is shown in Figure 2-8. The substrate heating plate could be rotated at 10 rpm. Substrates were mounted using substrate clamps, while the clamps themselves were fastened in place using threaded holes in the substrate plate.

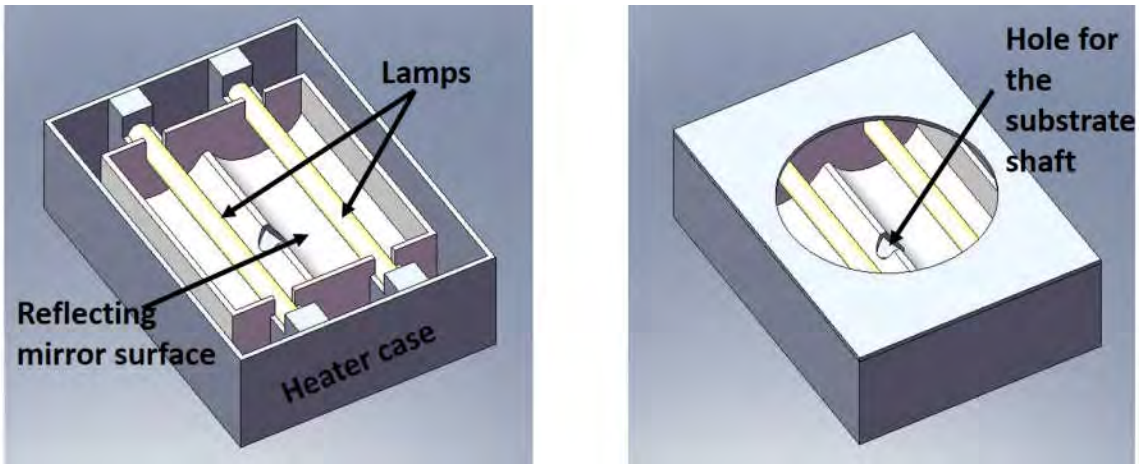

Figure 2-7: Substrate heater design (a) Interior of the heater, (b) Heater, with the covering face, but without the substrate plate

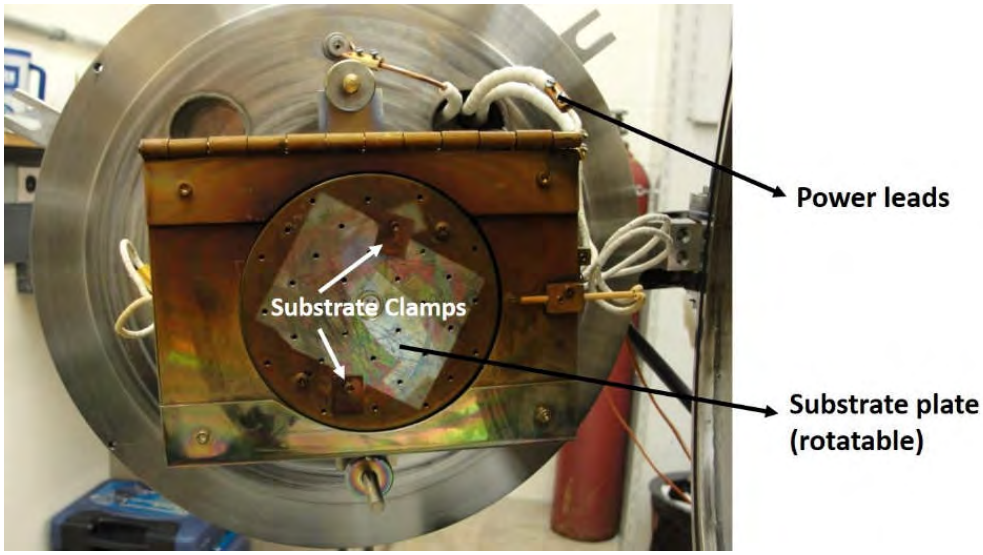

Figure 2-8: Substrate heater assembly

2.3.3 Optics

Rail systems were used to construct the basic structure to mount the various optical elements as shown in Figure 2-5. The laser beam was split into two parts using a 50-50 beam splitter. The reflected beam was focused onto the target for laser ablation (using a biconvex spherical lens), while the transmitted component was directed towards the

substrate, for *in situ* crystallization of the growing film. The target was rotated using a Magidrive from Kurt J. Lesker, Inc. A linear shift mechanism (LSM38-50-H, with 50 mm travel, from Kurt J. Lesker, Inc) was also utilized in line with the target shaft, in order to maneuver the target position (Figure 2-9). The laser annealing energy density was adjusted using two plano-convex cylindrical lenses (substrate material: UV-fused silica, and having anti-reflection coatings for 248 nm wavelength on both sides): one for manipulating the horizontal dimension (10 cm focal length), and the other for manipulating the vertical dimension (30 cm focal length). Highly reflective, standard dielectric mirrors (KRF-2037-45UNP, from CVI Melles Griot) were utilized for 90° reflection, while deep UV aluminum mirrors (DUVA-PM-1225-UV, from CVI Melles Griot) were utilized for non-90° reflection angles directing to the input of the ablation and annealing ports.

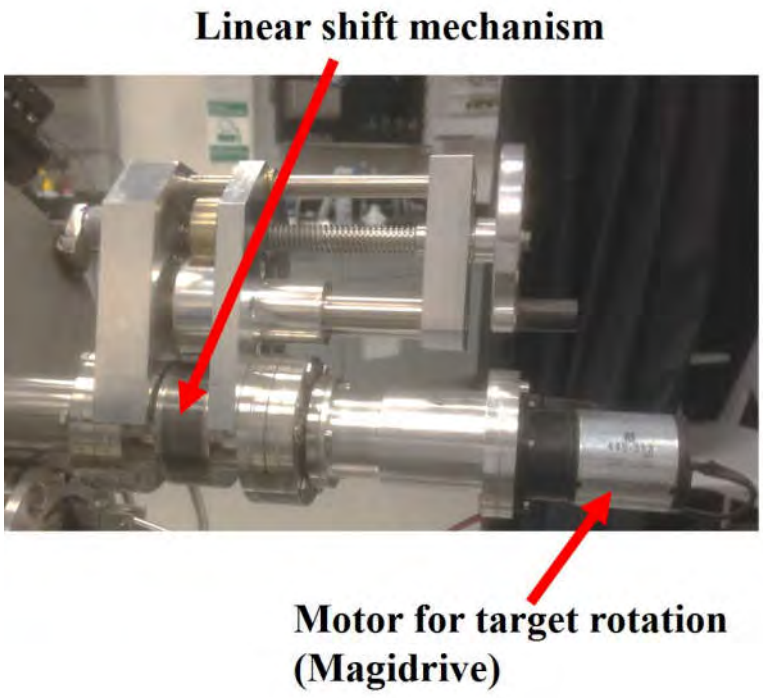

Figure 2-9: Target mechanics (Linear shift mechanism combined with the motor)

2.3.4 *In Situ* Laser Annealing Parameters

The system developed was utilized to grow and crystallize PZT thin films, first as a proof of its applicability and then to understand the microstructure evolution process. The substrates utilized in this work were platinized silicon ($Pt/Ti/SiO_2/Si$; obtained from Nova Inc) or (100) $SrTiO_3$ single crystals (obtained from MTI Corporation, Richmond, CA). Before deposition, the substrates were ultrasonicated sequentially in acetone, ethanol and isopropyl alcohol (IPA) each for 2-5 minutes, and then dried in nitrogen/compressed dry air. The processing parameters with regards to the ablation and annealing processes utilized are tabulated in Table 2-3.

Table 2-3: *In situ* laser annealing parameters

Growth and *In Situ* Laser Annealing Parameters	
Laser Wavelength	248 nm (KrF Excimer Laser)
Laser Pulsewidth	20 ns
Pulse Repetition Rate	20 Hz
Target	PZT (52/48) + 20% PbO
Laser Ablation Fluence	1-2 J/cm^2
Target-Substrate Distance	6-7.2 cm
Substrate Temperature	350 – 380 °C
Ambient Pressure	50 - 120 mTorr (10% O_3 in O_2)
Growth Rate	~0.1 Å /pulse
Annealing Energy Density	50 – 60 mJ/cm^2

2.4 Structural/Microstructural Characterization

2.4.1 X-ray Diffraction

A Philips Analytical X-ray Diffractometer (PANalytical B. V., Almelo, The Netherlands) was used to assess the crystallinity and out-of-plane orientation of the thin films. Cu-Kα radiation (wavelength = 1.5406 Å) was used with the XRD generator settings at 45 kV and 40 mA. The typical scan range was from 20° to 72° with a 0.02 step size and a 1 sec count per step. A quartz zero background holder (ZBH) was used between the sample and the sample stage. The various phases were determined using the PDF card numbers tabulated in Table 2-4.

Table 2-4: PDF cards for various materials used in this work

Material	PDF #
$Pb(Zr_{0.52}Ti_{0.48})O_3$	01-070-6602
$Pb(Zr_{0.30}Ti_{0.70})O_3$	01-070-4055
$Pb_2Ti_2O_6$ (Pyrochlore)	00-026-0142
Pt	00-004-0802
Si	00-027-1402
$SrTiO_3$	00-005-0634
Cu	00-004-0836

The relative fractions of the various orientations were determined by integrating the area under the curve of the various peaks. For this, the peaks were fit using the Lorentzian function [63]:

$$I = A_o \frac{2}{\pi} \frac{w}{4(x - x_c)^2 + w^2} + C \quad (4)$$

where, A_o: amplitude, w: full width at half maximum, x_c: center position, C: constant.

A Philips X'pert Pro MRD 4-circle diffractometer (PANalytical Inc., Tempe, AZ) was used to determine the off-axis orientation and ascertain the epitaxial quality of the films grown on (100) $SrTiO_3$ single crystalline substrates. The equipment collimates Cu $K_{\alpha 1}$ radiation using a hybrid graphite monochromator.

2.4.2 Scanning Electron Microscopy (SEM) and Transmission Electron Microscopy (TEM)

A Leo 1530 Field Emission Scanning Electron Microscope (Carl Zeiss, Oberkochen, Germany) (FE-SEM) was used to examine the microstructural features of the specimens. The secondary electron mode (using the through-the-lens detector) was utilized to study either the surface grain structure or the cross-sectional morphology of the various thin films. SEM cross-sectional samples were prepared by fracture (cleaving of the silicon substrates).

For the TEM characterization, cross-sectional specimens were prepared by dual beam focused ion beam (FIB) milling (using a FEI Helios NanoLab 660). TEM analysis was carried out using a JEOL 2010F scanning transmission electron microscope (STEM/TEM) equipped with a high angle annular dark-field (HAADF) detector and an Oxford Instruments energy dispersive X-ray spectroscopy (EDS) system and Gatan Image Filter

(GIF) system. Compositional uniformity measurements were performed by EDS in STEM mode with an electron probe of 1 nm diameter. A C-s corrected Titan was also employed in the bright field mode to obtain the crystallization depth in the films. Nanobeam diffraction was used to identify the amorphous vs crystalline regions in the samples.

2.4.3 Spectroscopic Ellipsometry

Spectroscopic ellipsometry was utilized to study the optical properties of the films and to determine the reflectivity and absorption coefficient of the as deposited films at the laser absorption wavelength (248 nm). The optical characterization was carried out at room temperature using a rotating compensator spectroscopic ellipsometer (M-2000 XI, from J. A. Woollam Co., Lincoln, NE) at three angles of incidence (θ_i = 55°, 65° and 75°) and over the spectral range of 245 nm to 1690 nm.

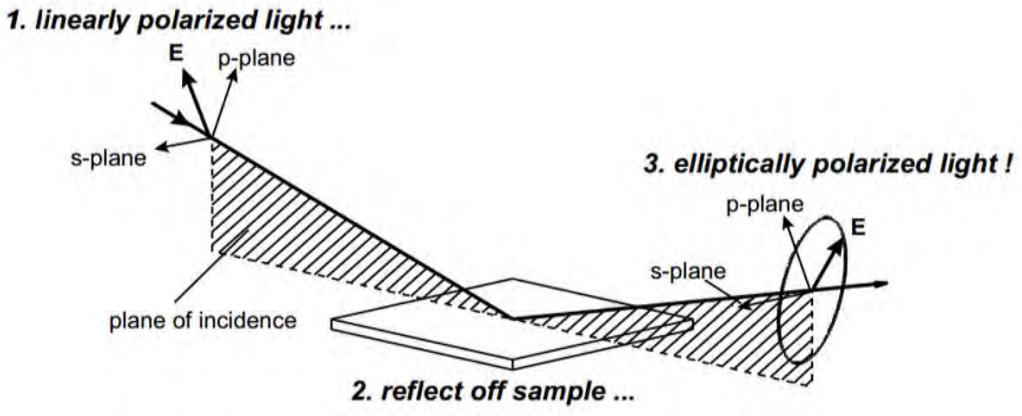

Figure 2-10 Principle of ellipsometry (from Ref. [64]**)**

An ellipsometer (schematic of the measurement shown in Figure 2-10) measures the change in the polarization state of the incident beam on reflection by the sample in terms of the ellipsometric parameters: Psi (ψ) and Delta (Δ) (defined in equation (5)) [65].

$$\tan(\Psi) \cdot e^{i\Delta} = \rho = {}^{r_p}/_{r_s} \quad (5)$$

where, ρ is the ratio of reflectivity for p-polarized light (r_p) divided by the reflectivity for s-polarized light (r_s).

A least squares regression analysis was used alongside a weighted root Mean Squared Error (MSE) [66] to fit the experimentally obtained ψ and Δ parameters (with the aid of CompleteEASE® software provided with the tool). Consequently, the various material parameters such as the complex index of refraction (N = n + ik), and also microstructural parameters such as layer thickness, surface roughness thickness and void fraction in the material can be extracted.

2.5 Electrical Characterization

Dielectric, ferroelectric and piezoelectric measurements on the films were carried out on capacitor structures. The process will be delineated in this section.

2.5.1 Top Electrodes by Lift-off Process

Capacitor structures with Pt top and bottom electrodes, with the insulating PZT material sandwiched in between was used for the electrical measurements. A photolithographic lift-off process was used to obtain the top electrodes. The samples were first heated on a hot plate at around 150°C for about 5 minutes to remove moisture. This was especially necessary for the polymeric substrates. The sample was then spin-coated with LOR 5A (lift-off resist from MicroChem Corp. MA) at 4000 rpm and for 45 seconds and then cured. The curing conditions were 180°C for 2 minutes. The sample was then spin-coated with a

layer of photoresist (SPR 3012) and at 4000 rpm for 45 s. A soft-baking step was then carried out at 100°C for 1 minute. The photoresist was then UV exposed (Hg vapor lamp) through a mask pattern consisting of circular electrodes in the range 10 μm – 400 μm diameter, using a Karl Suss MA/BA6 contact aligner for about 12 s. The exposed pattern was then developed using a base (CD 26) for about 1.5 minutes, after which the samples were rinsed with DI water and blown dry using compressed nitrogen. After the developing step, the samples were then cleaned in oxygen/helium (3:1) plasma using an M4L tool from MetroLine. 100 nm thick Platinum deposition was then carried out using a Kurt J. Lesker CMS-18 sputter tool. Subsequently, lift-off process to remove the photoresist/LOR5A covered regions was performed using acetone (to remove the photoresist) and CD26 (to remove LOR5A).

Access to the bottom Pt electrode was provided either by masking off a certain area of Pt during the growth, leaving a certain region uncoated, or alternatively, in cases where this was not possible, the bottom Pt was exposed by etching through the PZT using BOE 10:1 and 36% w/w HCl solutions (for about 1 to 2 minutes).

2.5.2 Dielectric Measurements on PZT Films

Low field dielectric properties (permittivity and loss) were obtained for the capacitor structures using a Hewlett-Packard 4284A impedance analyzer over the range from 100 Hz to 10 kHz, at an oscillating voltage of 30 mV_{rms}.

The permittivities (ϵ_r) of the films were calculated using:

$$\epsilon_r = \frac{Ct}{\epsilon_o A} \tag{6}$$

where, ϵ_o is the permittivity of the free space, while C, t and A are the measured capacitance (in Farads), thickness and area under the top electrode, respectively, for the film.

2.5.3 Ferroelectric and Piezoelectric Characterization

Polarization-Electric Field hysteresis measurements were carried out at 100 Hz frequency in the virtual ground testing mode using either a TF Analyzer 2000 tool (Aixacct) or the Multiferroic tester (from Radiant Technologies Inc., Albuquerque NM). Maximum electric fields to the order of 600 kV/cm were applied.

For the piezoelectric charge measurements ($e_{31,f}$), the wafer flexure method was used [67],[68]. The method has been explained in detail in Ref. [68]. The strain in the sample is modulated at 4 Hz using a periodic pneumatic force generated by a speaker. The strain values were measured using Pt thin film strain gauges (part of the electrode pattern created by lift-off). The produced piezoelectric charge across a circular top electrode and the bottom electrode (electrically grounded) was measured by reading the voltage developed on a charge integrator (using an SRS830 lock-in amplifier from Stanford Research Systems).

Chapter 3 Pulsed-Laser Crystallization of PZT Thin Films on Polymeric Substrates

One of the goals of this dissertation is using pulsed laser-induced crystallization as a means to explore integration with temperature sensitive substrates such as polymers. A promising application for a piezoelectric on a polymer is a mechanical energy harvester (MEH) in biological implants or wearable electronics [19], [69]. Powering an implanted biomedical device such as a heart rate monitor, pacemaker etc., using an embedded battery would require regular replacement of the battery, and might require a surgical procedure that would drive up the cost, while also making it unsafe. Alternatively, biomechanical energy from the natural and periodic heart and lung motions can be harvested using piezoelectric generators and utilized to power these devices. This should however be done in a non-invasive manner, i.e., without imposing any constraints on the functions of the organs and hence would dictate the use of a piezoelectric with a high electromechanical coefficient, such as PZT. However, the thermal processing incompatibility for piezoelectric/ferroelectric oxide on polymers dictates the use of complex thin-film transfer methods [19], [17], [70], [71] and involves fabrication of the piezoelectric layer on a host/sacrificial substrate before eventually transferring onto the actual device. The transfer generally relies either on a laser lift-off [69], a physical peel-off process or etching of a sacrificial layer [17], [70], [71] onto substrates such as poly-dimethylsiloxane (PDMS), polyimide (PI), or polyethylene terephthalate (PET). The complexity of these methods arises from a low transfer yield and high costs [17]. On the other hand, use of an organic polymer ferroelectric such as polyvinylidene terephthalate (PVDF) to overcome the need for higher processing temperatures are not attractive due to low piezoelectric coefficient of

the polymer [70]. Attempts have also been made for direct crystallization of the piezoelectric films on the polymer substrate at low temperatures. In [72], authors used a chemical solution deposition technique, wherein the low substrate temperature crystallization of PZT was achieved by a combination of seeded diphasic sol-gel (SDSG) precursors and photochemical solution deposition (PCSD). Here, the presence of crystalline nanoseeds in a photoactive sol provided pre-existing nuclei, effectively reducing the crystallization temperature.

This chapter describes the crystallization of PZT (30/70) thin films on top of Pt/Ti/SiO_2/Si (platinized silicon) and Pt/Ti/EDF (Epoxy-based Dielectric Film) substrates below ~250˚C and their structural/ microstructural and electrical characterization. First, factors affecting crystallization (in terms of laser energy density, annealing time and argon pressures during sputtering) will be discussed using platinized silicon as the model substrate. Subsequently, transfer of the deposition and annealing parameters to obtain crystallization on polymeric EDF substrates are presented. A layer-by-layer crystallization approach was utilized to improve the chances of through-thickness crystallization of the films and will be discussed along with the electrical properties and cross-sectional TEM analysis to understand the crystallization behavior. Finally, an extension of the laser annealing process to various substrates such as glass, EDF, and polyimide substrates will be developed.

3.1 Crystallization

Amorphous thin films were sputtered from a PZT (30/70) ($Pb(Zr_{0.3}Ti_{0.7})O_3$) target with either 10% or 20% excess PbO at room temperature using conditions mentioned in Chapter 2, either on $Pt/Ti/SiO_2/Si$ substrates (from Nova, Inc.) or on Pt/Ti coated polymeric Cu/EDF (epoxy based dielectric film) substrates (provided by Intel, Inc., Chandler, AZ). A Ti-rich PZT composition was chosen to take advantage of the low nucleation energy barrier of such a composition compared to a Zr-rich PZT [26]. Crystallization of the amorphous films was achieved by laser annealing at a substrate temperature of 200-215°C, either in 10% O_3/90%O_2 or a pure O_2 ambient gas. First, to understand the effect of process variables, $Pt/Ti/SiO_2/Si$ substrates were used as model substrates. The parameters were then utilized to deposit and crystallize on the polymeric Pt/Ti coated EDF substrates with exposed Cu pads. The latter limits processing temperatures to <250˚C, and explains the choice of substrate temperatures used in this work.

3.2 Factors Affecting Crystallization

3.2.1 Effect of Ar Sputtering Pressure (Crystallization on $Pt/Ti/SiO_2/Si$ Substrates)

Work was initiated by determining appropriate sputter deposition conditions for amorphous PZT films to facilitate laser crystallization. Figure 3-1 shows the influence of the Ar sputtering pressure used during deposition on the laser-induced crystallization of 300 nm thick PZT (30/70) thin films (grown from a 10% excess Pb target). The crystallization parameters for laser annealing were: energy density ~66 mJ/cm^2, pO_2: 50 mTorr, substrate temperature: 200˚C, annealing duration: 6 min @ 10 Hz. It can be observed that crystallization improved with increasing Ar pressure. An increase in Ar

pressure causes increased scattering of the plasma and hence is correlated to an increased PbO content in the films, due to decreasing bombardment by the depositing species [73],[74],[75]. Since crystallization of PZT is nucleation controlled [26], the excess PbO appears to facilitate nucleation, as has been described elsewhere [76]. Moreover, the very weak dependency of the optical extinction coefficient of these films at the laser wavelength (248 nm) on the deposited Ar pressure (Figure 3-2) shows that the optical absorption of these films doesn't change appreciably with the varying Pb-content, and is not the cause of the observed crystallization behavior.

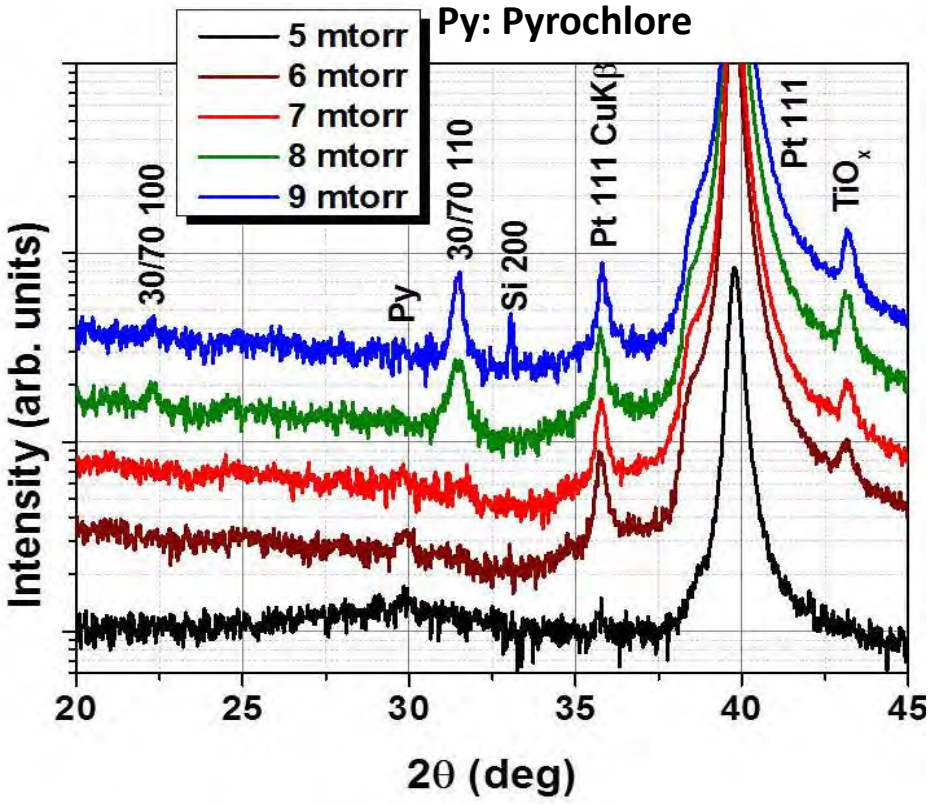

Figure 3-1: Effect of Ar partial pressures during sputtering on crystallization using laser annealing. Curves for different samples are offset for clarity

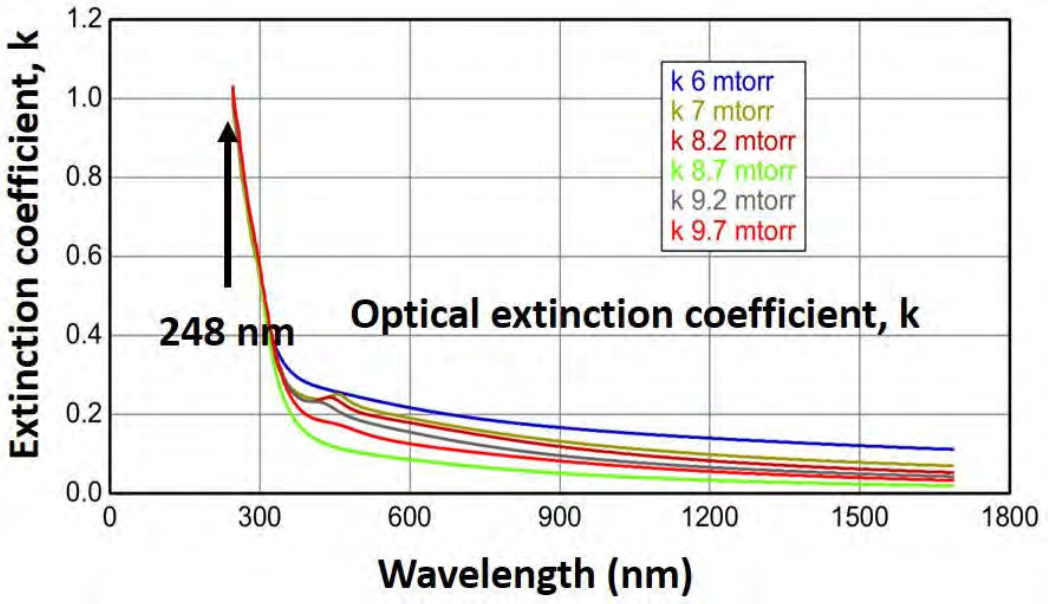

Figure 3-2: Extinction coefficient of as-deposited PZT (30/70) films on single crystalline MgO (001) substrates as a function of the sputtering Ar pressure, obtained by spectroscopic ellipsometry

3.2.2 Effect of Ozone in Oxygen (O_3/O_2) vs Pure Oxygen Ambient (Crystallization on Pt/Ti/SiO_2/Si substrates)

The effect of reactive oxygen during laser annealing was also studied. Figure 3-3 shows the influence of laser annealing energy densities on 300 nm thick PZT (30/70) thin films either in 10% O_3/O_2 (a) or in pure O_2 (b). In both cases, the pressure in the chamber was maintained at 50 mTorr, and the substrate temperature was ~200˚C. In ozone, an intermediate low temperature pyrochlore phase is formed at energy densities between 36-66 mJ/cm^2 and PZT crystallization is apparent only above these energy densities (with residual pyrochlore). However, the low temperature pyrochlore is not observed on annealing in pure O_2 (Figure 3-3(b)). Moreover, the perovskite PZT phase formed at a lower energy density of ~57 mJ/cm^2 in the case of pure O_2 compared to ~66 mJ/cm^2 for O_3/O_2. (Note: a film soaked at 200˚C for 30 minutes but not exposed to the laser beam didn't show any crystallization as evidenced by the black curve in Figure 3-3(a)).

Considering this, it can be hypothesized that an ozone ambient renders the surface highly reactive. It is known that photodissociation of O_3 under 248 nm radiation could give rise to highly reactive O radicals [77]. O_3 apparently stabilizes the low temperature pyrochlore phase, delaying the conversion to perovskite to higher laser energy densities. This might be due to the oxidation of Pb^{2+} (characteristic of metastable pyrochlore $Pb_2(Zr,Ti)_2O_6$) to Pb^{4+} ions (characteristic of the stable pyrochlore $Pb_2(Zr,Ti)_2O_7$) [78]. Furthermore, O_3 is also known to cause some absorption of the 248 nm wavelength, which could also reduce the energy density at the film surface.

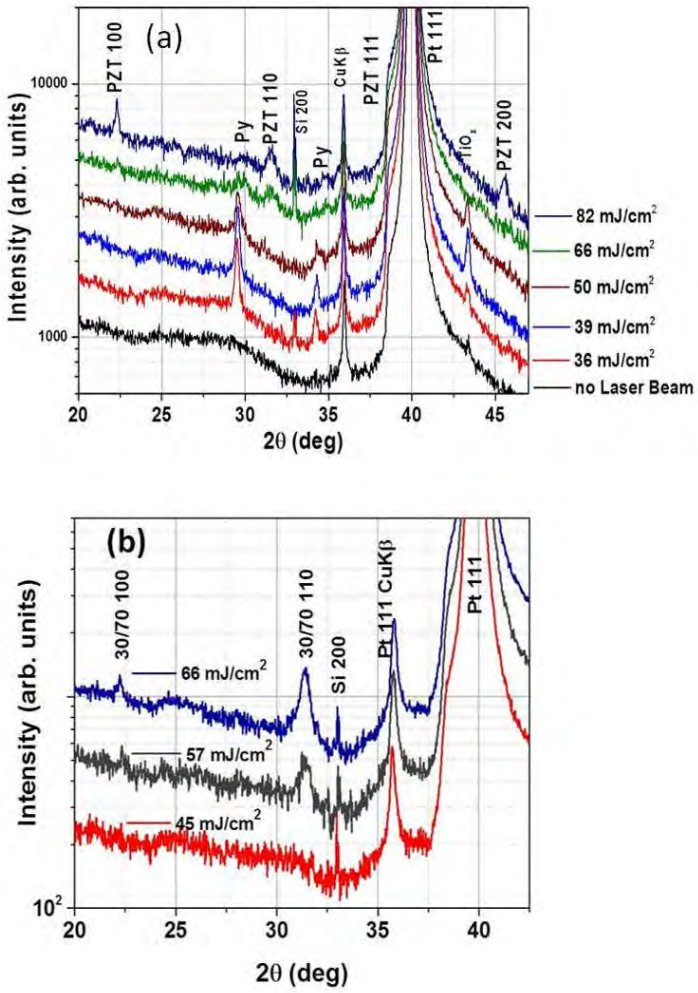

Figure 3-3: Crystallization as a function of annealing laser energy density in (a) 10% O_3/O_2 and (b) pure O_2 ambients. Py=pyrochlore

3.2.3 Crystallization as a Function of Time

Figure 3-4 shows the surface crystallization as a function of irradiation time (or equivalently, the number of laser pulses) for ~300 nm thick PZT 30/70 films grown on platinized silicon exposed to several laser pulses with energy density ~66 mJ/cm^2. On irradiation, it can be seen that nucleation of perovskite grains is initiated on the surface, and the nuclei grow laterally until they impinge. There seems to be an induction period [36] until about 300 laser pulses (~6 μs of laser exposure, given the 20 ns pulsewidth for the laser), after which, time-dependent nucleation events are observed (as evidenced by

films exposed to 600, 1200 and 1800 laser pulses) and the surface transformation is complete by the end of 2400 pulses (~48 μs). Between 2400 and 12000 pulses, no further grain size changes are evident, pointing to the fact that grain boundaries are presumably immobile under the laser annealing conditions studied; however, at 12000 pulses, some surface structure is evident, possibly due to the evaporation of Pb from the surface. The percentage of phase transformed surface area can be tracked as a function of cumulative pulse-time and has been graphed in Figure 3-5. Johnson-Mehl-Avrami-Kolmogorov (JMAK) transformation kinetics describes isothermal kinetics [36]. In the absence of rigorous mathematics to characterize kinetics due to the non-isothermal nature of laser heating, a fit to JMAK kinetics was nevertheless attempted as shown in Figure 3-5. The results have a growth exponent of 5.2, which is unrealistic unless the nucleation rate increased with an increase in time [36]. For a better estimation of growth kinetics, a more plausible time at temperature values should be considered (rather than just the pulsewidth of the laser, considering the temporal lag between the end of the laser pulse, and the heating time). Furthermore, the non-isothermal mode of heating should be factored into the analysis.

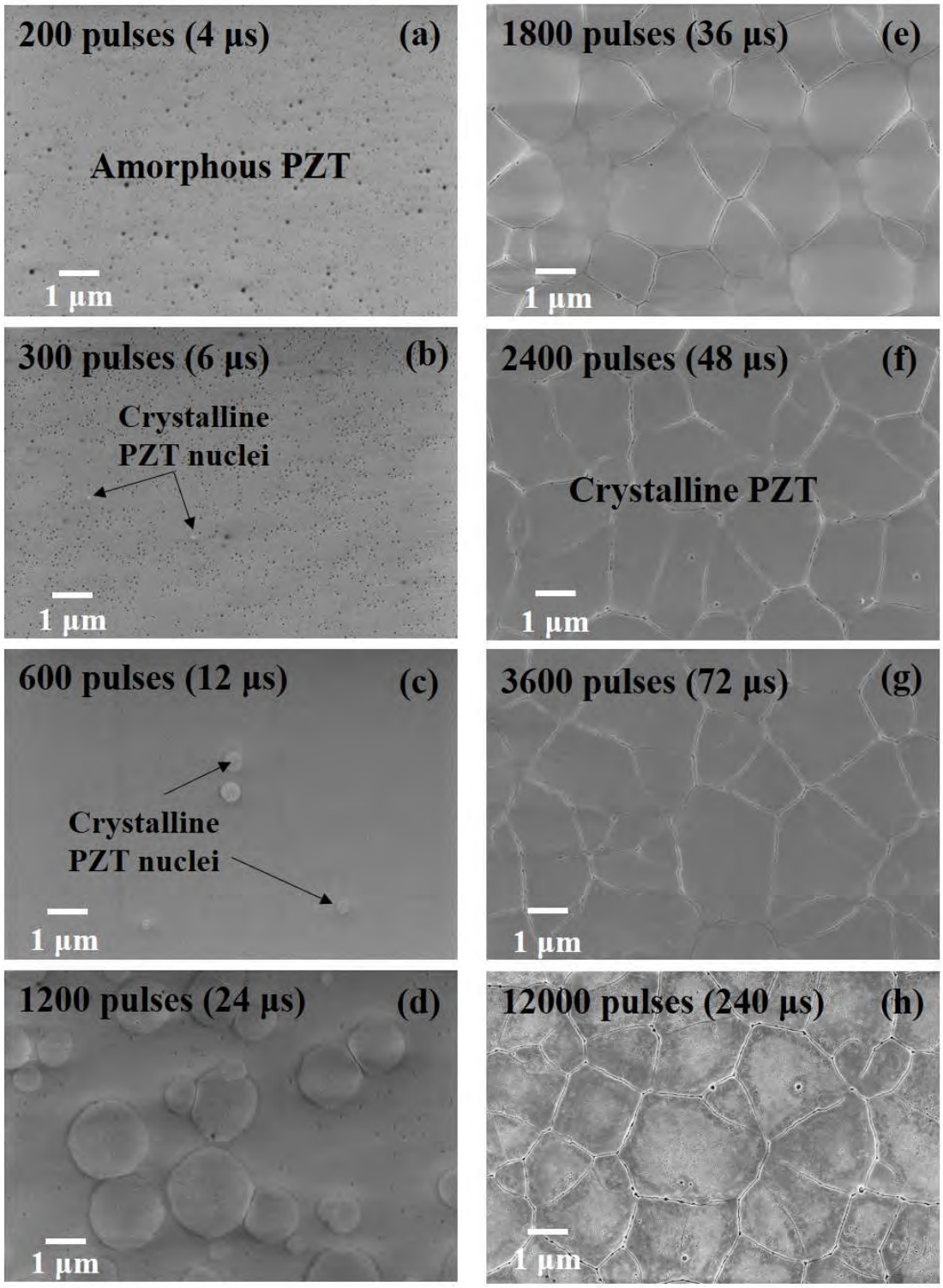

Figure 3-4: Surface nucleation as a function of number of laser pulses @ 10 Hz; (a) 20 sec (200 pulses), (b) 30 sec (300 pulses), (c) 1 min (600 pulses), (d) 2 min (1200 pulses), (e) 3 min (1800 pulses), (f) 4 min (2400 pulses), (g) 6 min (3600 pulses and (h) 20 min (12000 pulses). The laser energy density used in all cases was about 66 mJ/cm^2

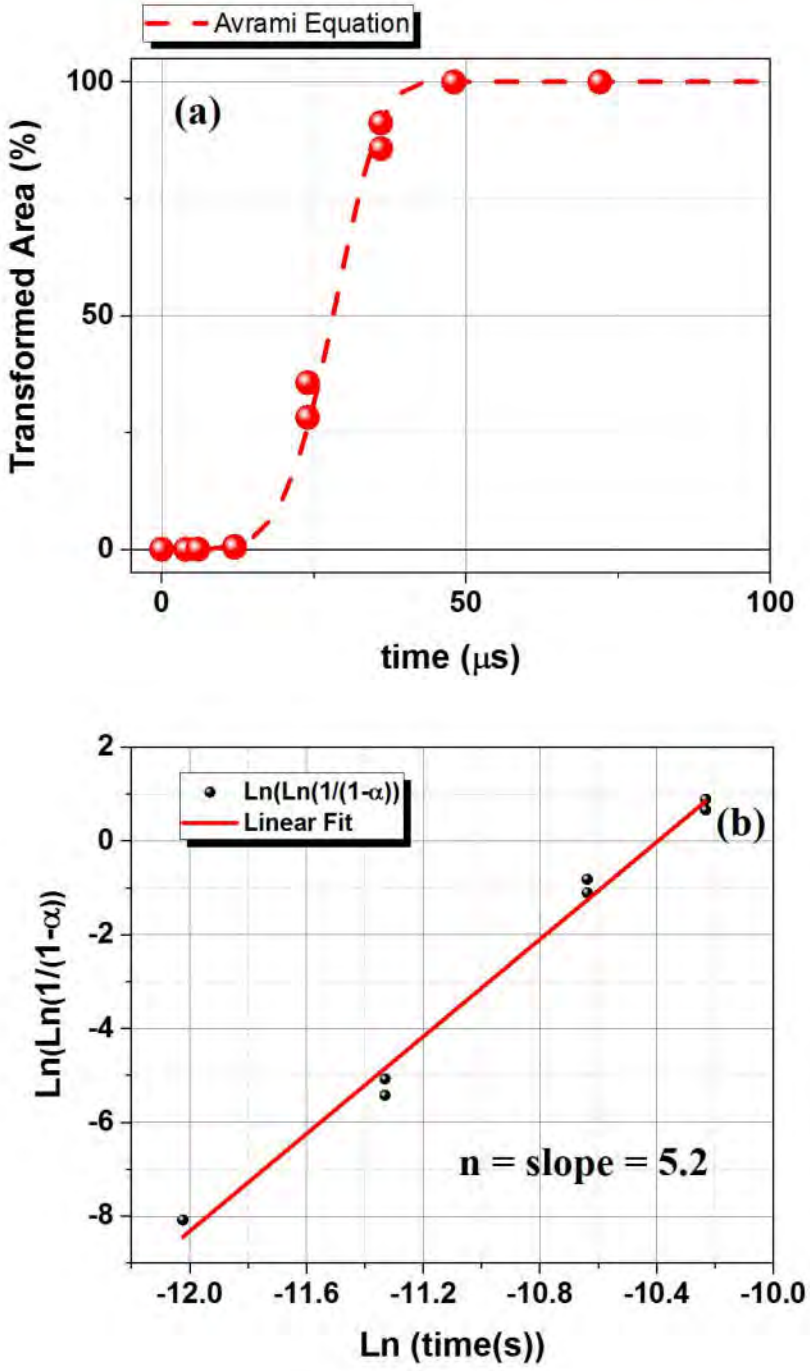

Figure 3-5: (a) Percentage of transformed area as a function of cumulative laser exposure duration, with the corresponding fit to Avrami equation, with Avrami parameters extracted from (b)

Cross-sections were studied to determine the extent of crystallization through-thickness. The platinized silicon substrate was cleaved using a diamond scriber in order to carry out these measurements. For the film exposed to 3600 pulses (Figure 3-6), the cross-sectional SEM suggests a layered microstructure across the thickness of the film, with only the top ~100 nm of the thickness being crystallized. Bright Field TEM of the ~300 nm thick PZT films on a platinized silicon substrate were carried out to confirm the crystalline/amorphous characteristics of the two layers. A focused ion beam (FIB) cross-section was prepared (courtesy: Joshua Maier & Trevor Clark, Materials Characterization Lab, Penn State University) to study the through-the-depth crystallization of the PZT on $Pt/Ti/SiO_2/Si$ substrates using TEM (courtesy: Ke Wang, Materials Characterization Lab, Penn State University). The through-thickness crystallization (Figure 3-7(a)) is limited to about 130-140 nm (the variation in this layer thickness compared to the one on cross-sectional SEM could be due to the localized quality of these measurements). Electron diffraction patterns from the surface layer (Figure 3-7(b)) and from the interior layer (Figure 3-7(c)) confirm the crystallinity of the top layer (with some reflections from the perovskite lattice), while the interior is still amorphous.

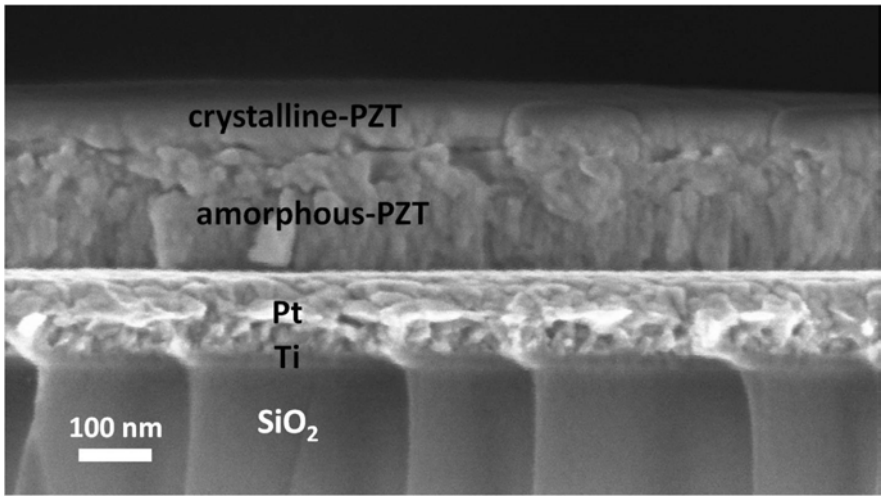

Figure 3-6: Cross-sectional SEM of crystallization of ~300 nm PZT exposed to 3600 pulses of ~66 mJ/cm^2

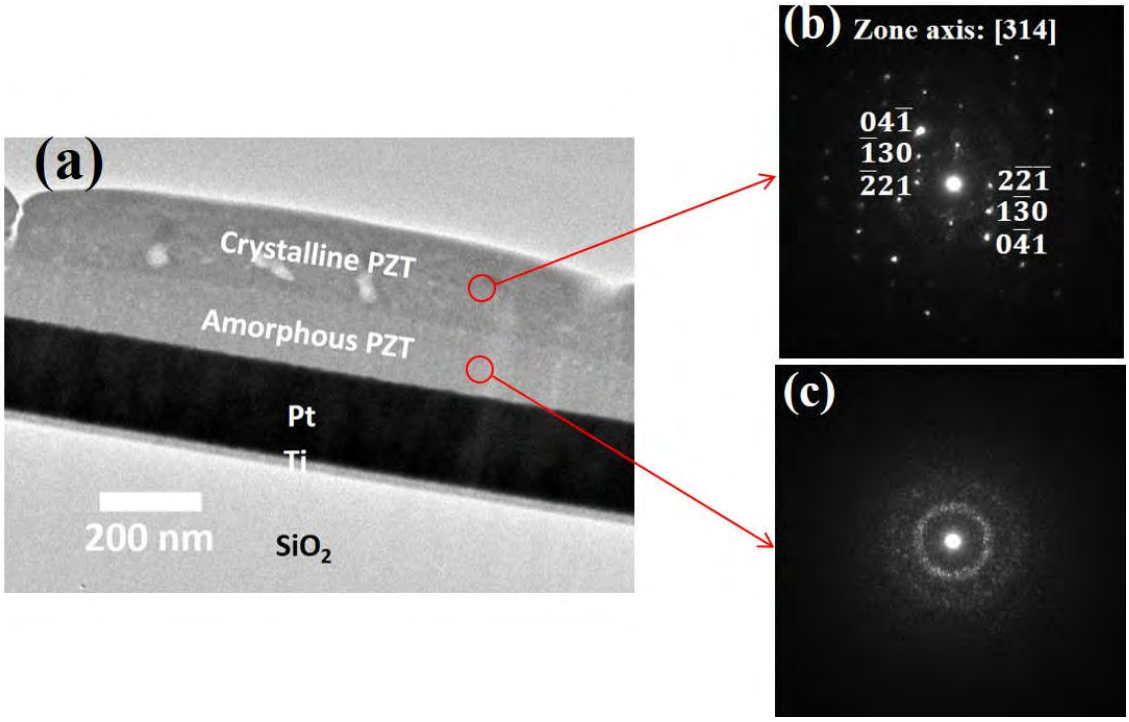

Figure 3-7: Cross-sectional bright field TEM (a) micrographs of 300 nm thick PZT (30/70) on Pt/Ti/SiO$_2$/Si substrate (annealing conditions: ~66 mJ/cm^2 for 6 min @10 Hz). (b) shows crystallization of the surface layer, while (c) shows that the interior is amorphous

Simulated temperature evolution curves for photothermal heating by a single laser pulse (248 nm wavelength, 20 ns pulse-width, energy density: 60 mJ/cm^2, substrate temperature: 200˚C) at various depths for 300 nm thick PZT on Pt/Ti/SiO_2/Si are shown in Figure 3-8. It can be seen that although the surface sees high temperature excursions (~1400˚C) which would cause heterogeneous nucleation from the surface, temperatures exceeding 600˚C (required for crystallization of good quality PZT) are seen only to a depth of about 200 nm inside PZT. This limited thermal penetration depth of the absorbed laser pulse [32] is likely to be the reason for the limited crystallinity through the film thickness. It must be noted that in this case, the temperatures are almost back to the background temperature by the end of about 10 μs from the initiation of the laser pulse, while the next laser pulse arrives after about 100 ms (in case of a pulse repetition rate of 10 Hz). Hence the various pulses can be treated as independent of each other, and the temperature profiles repeat themselves in cycles.

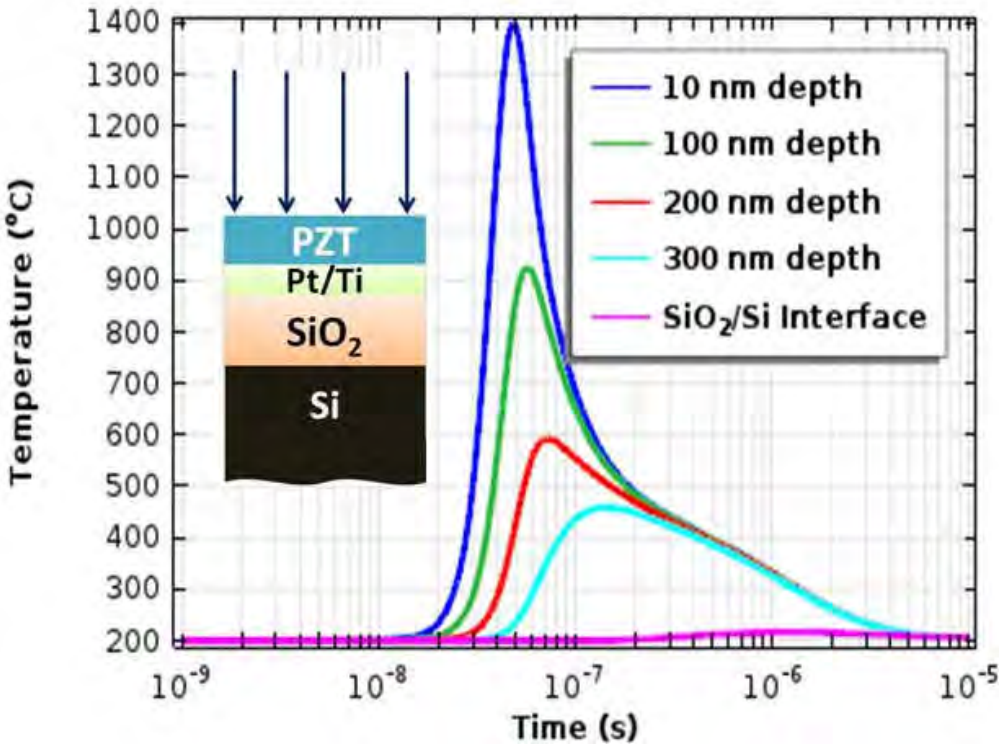

Figure 3-8: Temperature evolution at various depths in 300 nm thick PZT on Pt/Ti/SiO_2/Si

Considering these results, the pulsed laser induced crystallization process through a surface nucleation model can be constructed to understand the extent of crystallized volume. The results are schematically depicted in Figure 3-9. Surface nuclei are formed as a function of time due to heterogeneous nucleation; these then grow laterally and through the thickness. Impingement of the nuclei ultimately produces complete surface coverage. Presumably, the through-thickness growth is limited by the thermal penetration depth. It was found to be difficult to prove this quantitatively, as for very thin layers, a $PbPt_x$ phase was formed, which made it difficult to judge the penetration depth. However, it was found that the surface nucleated grains had similar through-thickness depth at the various substrate temperatures.

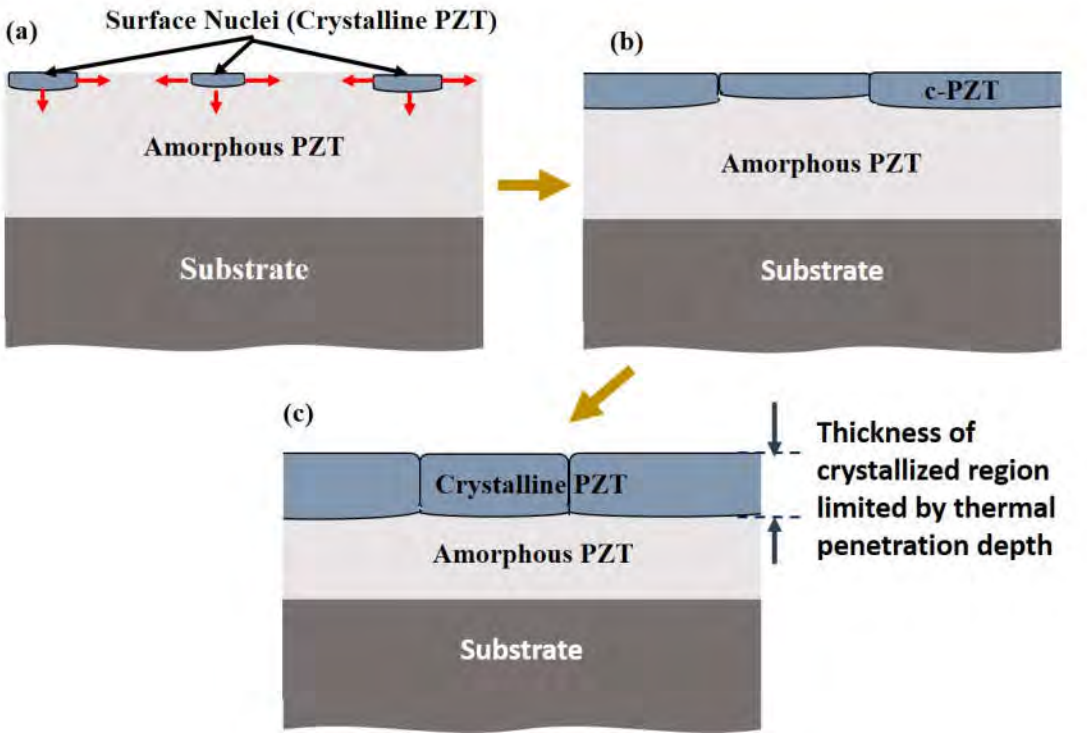

Figure 3-9: Schematic of the surface heterogeneous nucleation and growth of crystalline PZT (c-PZT) from an amorphous film on laser irradiation

3.3 Crystallization on Polymeric EDF Substrates

3.3.1 Roughness of Polymer Substrates

Two types of EDF (Epoxy-based Dielectric Film) base substrates were investigated: 300 nm RMS roughness Cu/EDF, and 100 nm RMS roughness Cu/EDF. The Cu coated EDF substrates were provided by Intel Inc., Chandler, AZ. For clean, unoxidized bottom electrodes, 100 nm Ti and 100 nm Pt were sputter coated using the Kurt J. Lesker CMS-18 tool to obtain the Pt/Ti/Cu/EDF substrates. While Pt/Ti bottom electrodes grown on the rougher of these two substrates were porous (Figure 3-10(a)) (enough to create porosity in the PZT layer grown on top), those grown on the smoother substrates were continuous (Figure 3-10(b)). Also, asperities from surface roughness are known to cause low electric field breakdown of PZT due to field concentration [79]; hence smaller roughness values

should be preferred. Hence, in the subsequent sections, experiments were carried out primarily on 100 nm rms roughness substrates.

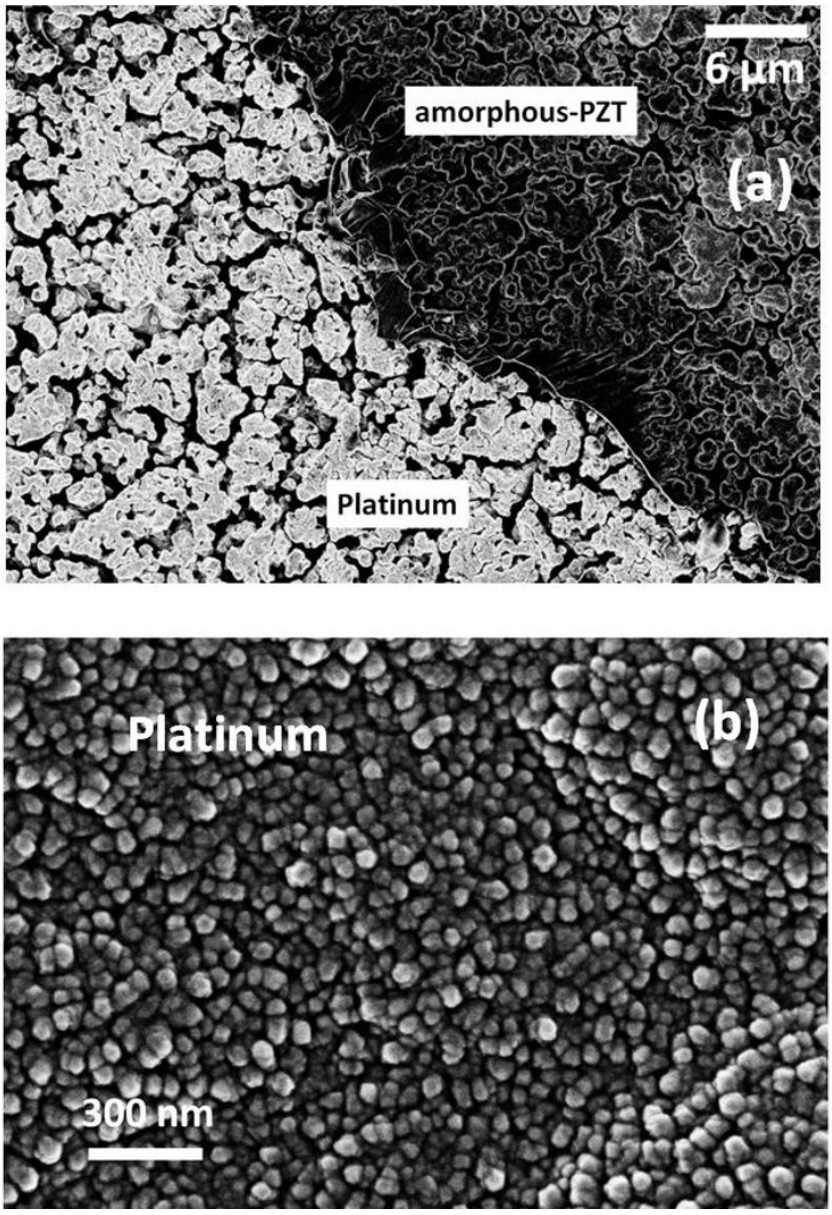

Figure 3-10: Surface FESEM of Platinum on (a) Pt/Ti/(300 nm rms rough Cu)/EDF, (b) Pt/Ti/(100 nm rms rough Cu)/EDF

3.3.2 Crystallization and Thickness Limitation

A similar set of experiments as described in sections 3.2.1 and 3.2.2 was carried on 300 nm thick PZT (30/70) thin films on platinized-EDF substrates. A substrate temperature of ~215˚C was used with the polymeric substrates. The general trends were maintained; i.e., increasing the sputtering Ar pressure improved the crystallization, while annealing in pure O_2 yielded better results than in 10% O_3/O_2. While perovskite PZT crystallization was not evident even at ~82 mJ/cm^2 in 10% O_3/O_2, phase formation was achieved at ~66 mJ/cm^2 in pure oxygen. Having determined this, for any further crystallization experiments, a pure O_2 ambient was utilized.

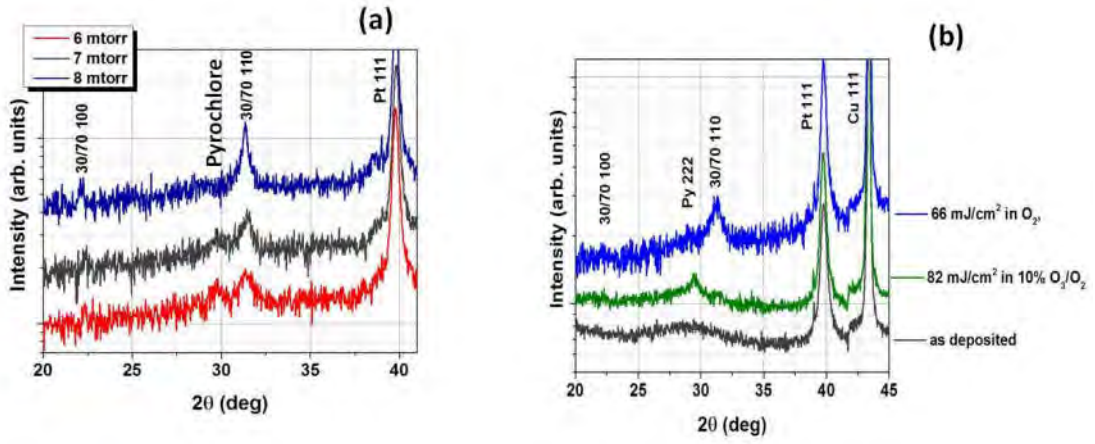

Figure 3-11: Crystallization on platinized EDF substrates. Effect of (a) Ar sputtering pressure and (b) O_3/O_2 vs pure O_2 ambient during annealing. Py = pyrochlore

Figure 3-12 shows the surface FE-SEM micrograph of the ~300 nm thick PZT films on a platinized EDF substrate. PZT grain structure similar to on platinized Si can be seen on the surface. The films were polycrystalline on both platinized Si as well as platinized EDF, without significant texture, as might be expected for heterogeneous nucleation from the

surface. Heterogeneous nucleation from the PZT/Pt interface would have produced a primarily $(111)_{pseudocubic}$ orientation.

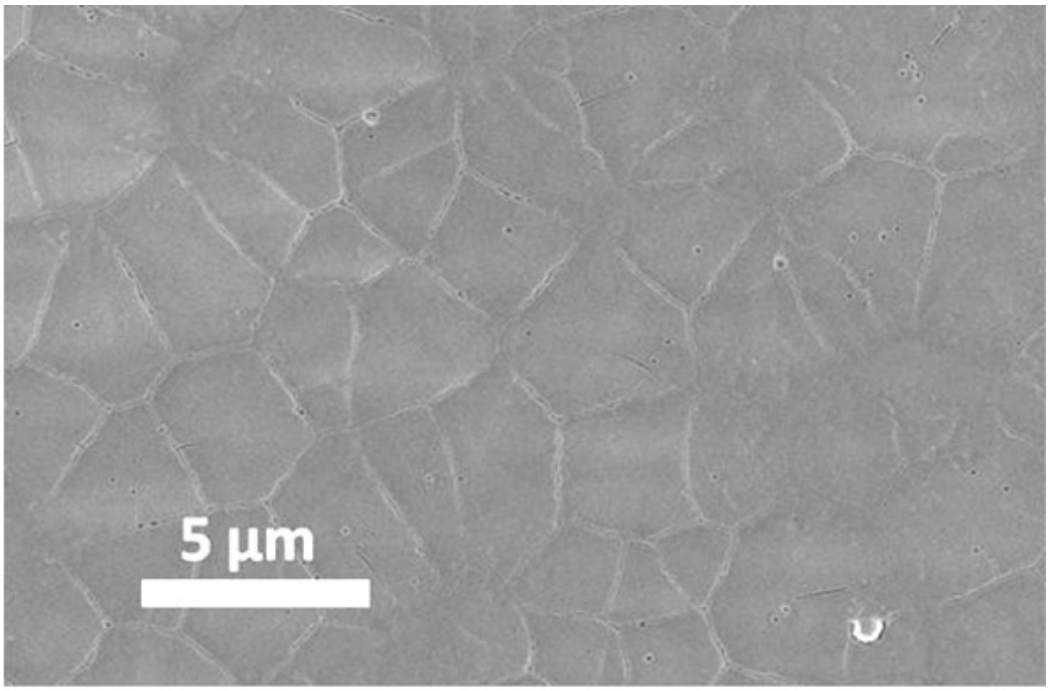

Figure 3-12: Surface SEM micrograph of 300 nm thick PZT (30/70) on Pt/Ti/Cu/EDF substrate showing the PZT grain structure (annealing conditions: ~66 mJ/cm^2 for 6 min @10 Hz).

3.4 Layer-by-layer Growth and Crystallization (on Pt/Ti/Cu/EDF substrates)

Since only a limited thickness of the ~300 nm thick film was crystallized with pulsed laser-heating, a strategy consisting of layer-by-layer growth and crystallization was adopted. To investigate this, three kinds of samples were prepared:

1. ~300 nm thick single layer
2. 3 layers of 100 nm each, up to a total thickness of ~300 nm
3. 4 layers of 75 nm each, again built up to a total thickness of ~300 nm.

The first 100 nm thick layer (3 layers sample amounting to ~300 nm total thickness) or 75 nm thick layer (4 layer sample amounting to ~300 nm total thickness) of PZT was grown using a 20% excess Pb target (to aid nucleation) while the remaining layers were grown using the 10% excess Pb target to reduce porosity and improve the electrical properties. Figure 3-13, shows the XRD patterns of the individual layers after crystallization while Figure 3-14 shows the surface FESEM's after the crystallization of the different layers for the case of 4 layers of 75 nm thickness each. The first layer crystallized from 20% excess Pb target shows a high level of porosity and a significant amount of unconverted regions, possibly due to the evaporation of excess Pb.

The grain sizes as observed from surface FE-SEM after crystallization of each individual layer for the three cases with total stack thickness of ~300 nm are plotted in Figure 3-15. It can be observed that the surface grain sizes decreased in subsequently deposited and laser crystallized layers. This suggests that with reduced thickness of individual layers, nucleation and growth from the bottom and top interfaces can be achieved. In order to confirm this, TEM characterization of the 4-layered film (with each layer being ~75 nm)

was carried out (Figure 3-16) (Courtesy: Ke Wang, Dan Veghte, MCL). Seeding from the interface between the layers was observed by cross-sectional HRTEM, for example, of the 4-layered film (with each layer being ~75 nm). Figure 3-17, for instance, shows the presence of a grain in the third layer which seems to have nucleated atop a grain in the second layer, given the continuity of the lattice fringes. Figure 3-18 shows another case of lattice continuity between the second and the third layers of the same 4-layered film, pointing to an epitaxial nature of the crystallization at the interface. The crystal planes stretched across the entire boundary in Figure 3-18 (a), in this case amounting to a distance of about 110 nm (this is a reasonable fraction of the estimated average grain size of the second layer, which was around 600 nm). Note: The relatively darker regions in Figure 3-16, Figure 3-17 and Figure 3-18 are most likely to be Pb-rich regions, while the blotchy nature of the HRTEM images could possibly be due to redeposition of PbO during sample preparation.

Additionally, the grain size distribution has been compared for the cases of single ~300 nm layer and the 4^{th} layer of the film grown and crystallized layer-by-layer, ~75 nm at a time (Figure 3-19). The almost Gaussian distribution in case of the single layer, compared to the skewed distribution in case of the layer-by-layer grown and crystallized film suggests the possibility of two separate populations of nuclei in the latter. This nucleation model has been schematically represented in Figure 3-20. Figure 3-20 (a) shows the presence of 3 grains (numbered 1-3) in the underlying crystalline PZT layer which grow upwards into the amorphous PZT layer on the top. In addition, surface heterogeneous nucleation also occurs, giving rise to the surface PZT grains. Figure 3-20 (b) shows the scenario where the laser induced crystallization is complete, where the two different sets of nucleation/growth

events gives rise to a larger number of surface grains (in this case, 6), compared to the interface grains (which, in the schematic, was 3). This would account for reducing the surface grain size and effectively increasing the grain density after each additional layer. It should be borne in mind that the two nucleation populations (surface and the interface) have distinct induction periods. The surface nuclei have an induction time corresponding to several hundred pulses, while the interface nuclei can be hypothesized as requiring almost no induction time.

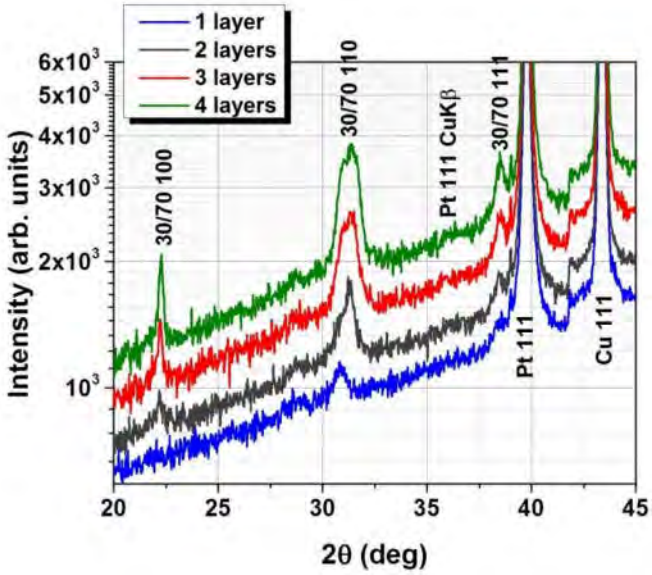

Figure 3-13: Sequential XRD's after the crystallization of each layer on Pt/Ti/Cu/EDF (each layer was about ~75 nm thick, while the total thickness was built up to ~300 nm)

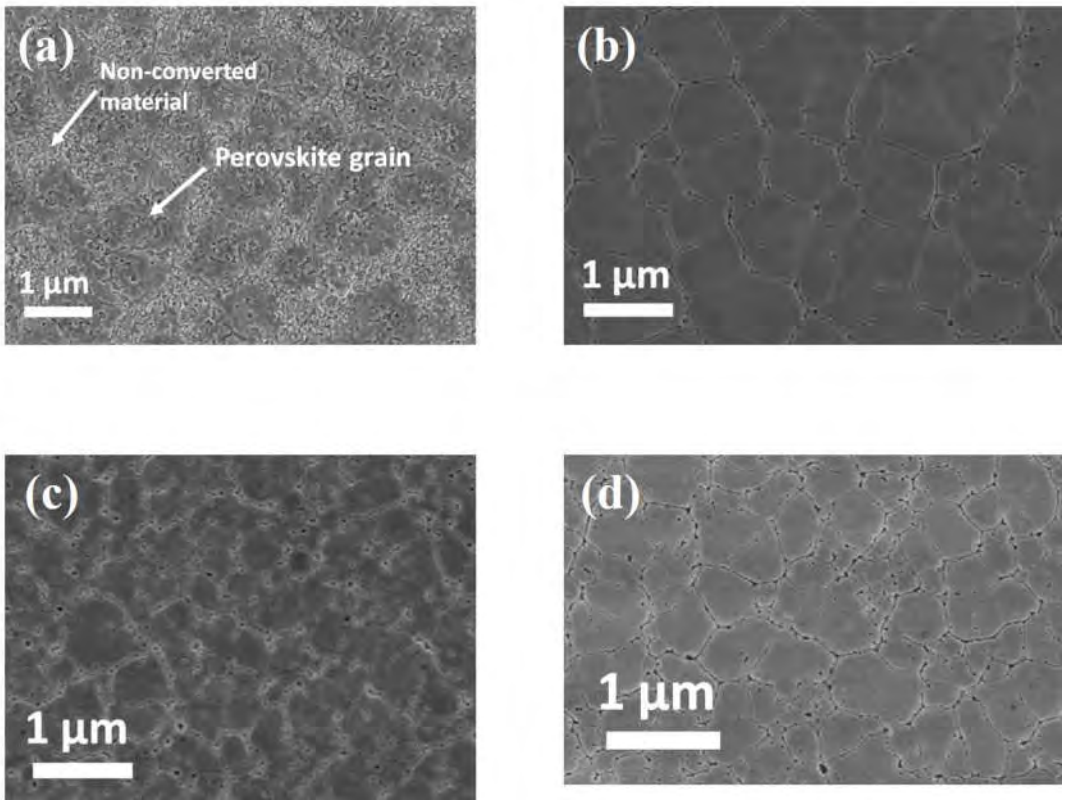

Figure 3-14 surface SEM's after (a) 1 layer, (b) 2 layers and (c) 3 layers and (d) 4 layers each of 75 nm thickness

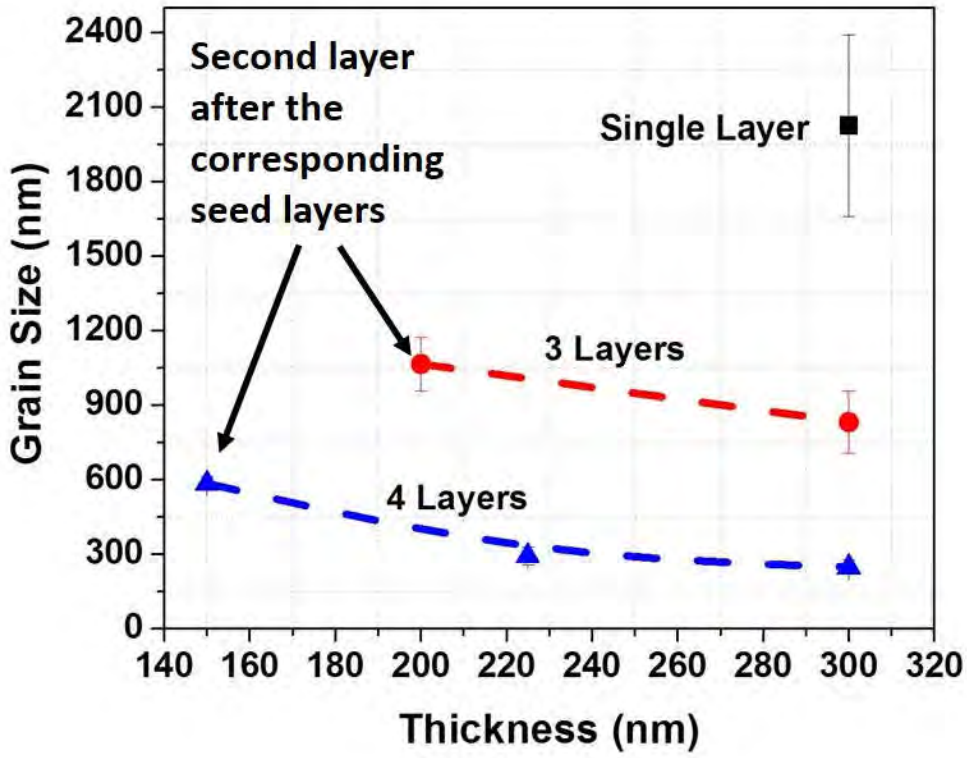

Figure 3-15: Grain sizes after crystallization of individual layers for the films grown up to a total thickness of ~300 nm

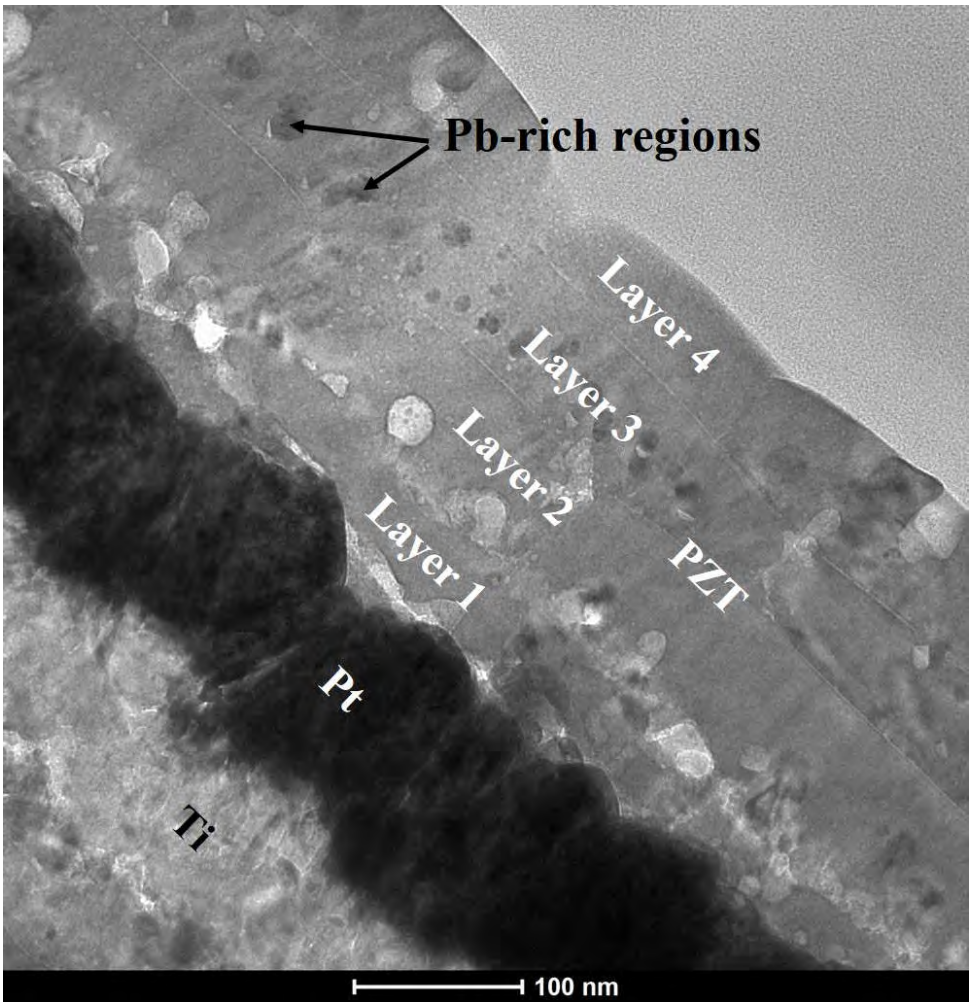

Figure 3-16: Bright field TEM of the layer-by-layer (total 4 layers) grown ~300 nm thick film (with each layer being ~75 nm each). The dark regions are supposedly Pb-rich regions.

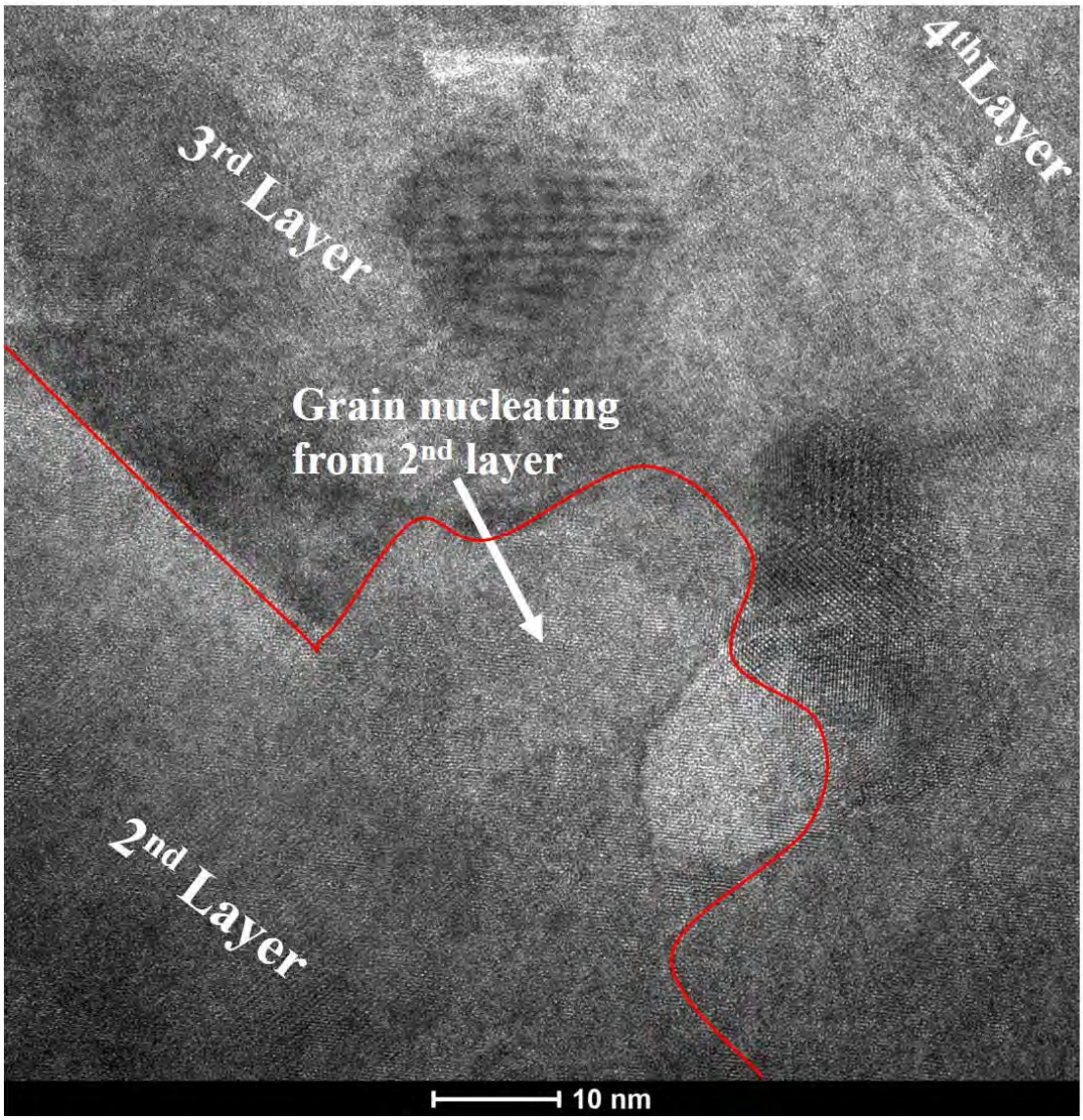

Figure 3-17: HRTEM image of the layer by layer grown ~300 nm film (with each layer being ~75 nm each). This image shows an instance of a grain in the 3rd layer nucleating atop another grain in the 2nd layer.

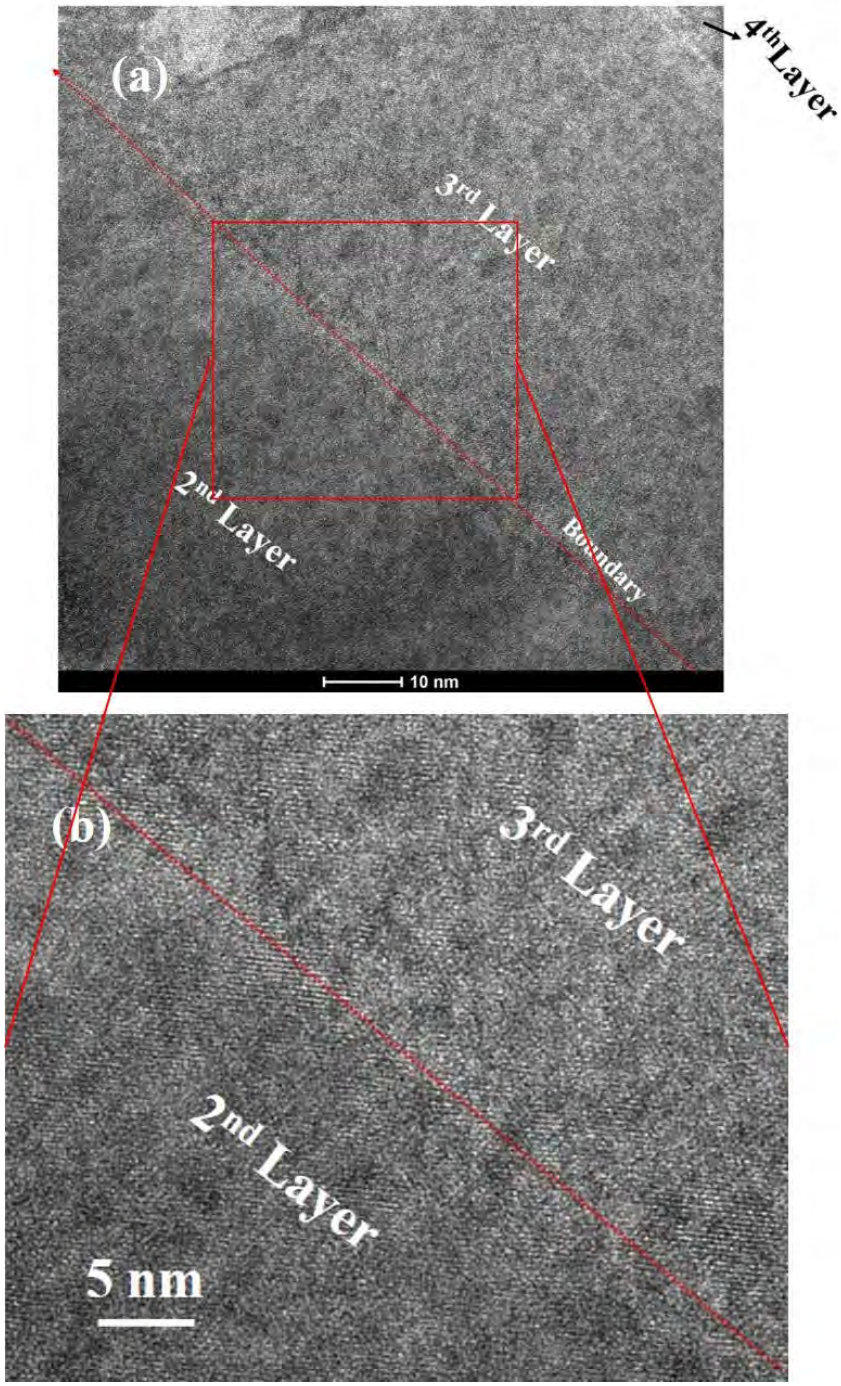

Figure 3-18: HRTEM image of another region in the layer by layer grown ~300 nm film (with each layer being ~75 nm each). Image (a) shows an instance of lattice continuity between 2nd and 3rd layer. A zoomed in area is shown in part (b). Continuity of the lattice fringes was found to stretch across the complete layer boundary in part (a), amounting to a distance at least of about 110 nm.

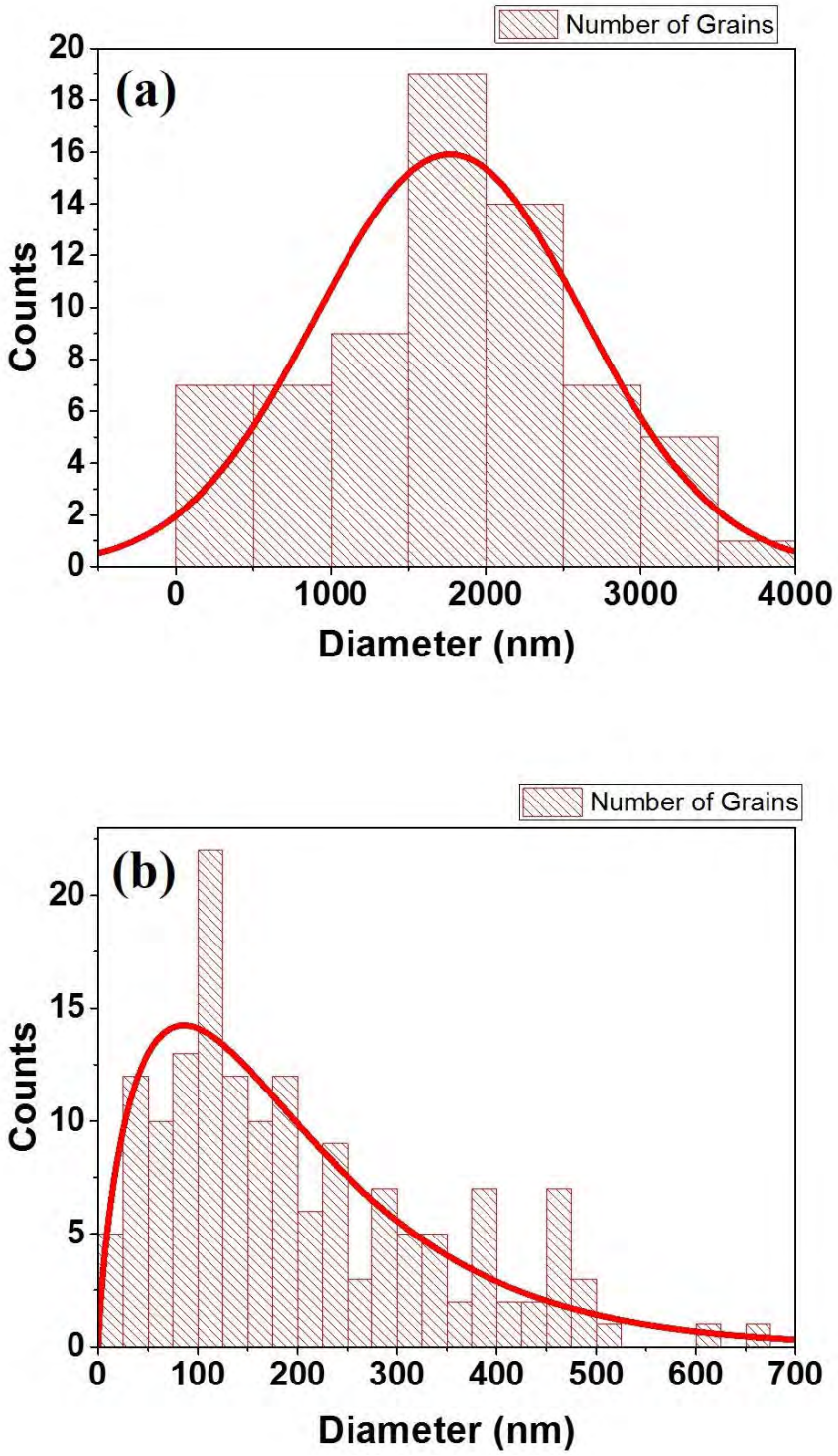

Figure 3-19: Grain size distribution (bar graph) for the cases of (a) single ~300 nm thick layer and (b) 4th layer for layers grown 75 nm each up to a total thickness of ~300 nm. The red distribution curves are a guide for the eyes only.

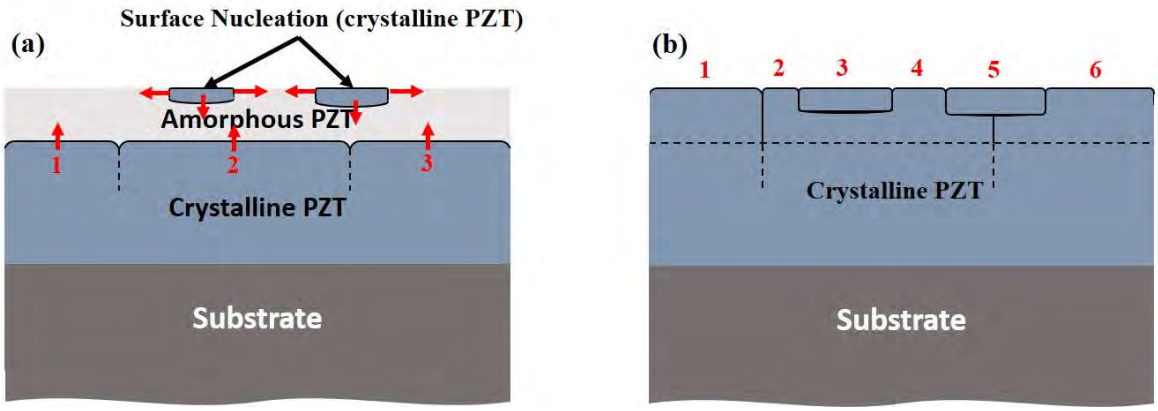

Figure 3-20: Heterogeneous nucleation model with nucleation at both top and bottom interfaces. The interface consists of 3 grains (numbered 1-3, in part (a)), while the surface depicted in (b) finishes with 6 grains on complete crystallization of the amorphous PZT layer.

3.4.1 Electrical Properties

Having achieved crystallization of the ferroelectric PZT phase, the electrical properties of these films were studied. The dielectric properties of films with various layers grown on Pt/Ti/Cu/EDF are summarized in Table 3-1. For the single layer ~300 nm films, a significant amount of amorphous phase is assumed to be present in the depth of the film, as the crystallization mainly occurs top-down in these conditions. An improvement in the dielectric constant values from ~90 to ~167 is seen on moving from single layer to 4-layers (layer-by-layer crystallization) on the platinized EDF substrates. For comparison, PZT (30/70) has a dielectric constant of ~400 – 600 [80]. The measured permittivities of the films grown layer-by-layer are below those of values reported in literature. The polarization-electric field hysteresis curve of the ~300 nm film grown and crystallized in 3 steps is shown in Figure 3-21. The film demonstrated ferroelectric switching, however the loops were rounded, pointing to substantial high field loss. Reproducible switching was not obtained from the other films. The crystallinity of the seed layer and the Pb-content has

to be closely controlled in these films to reduce the porosity and to allow for driving to higher electric fields. Excess Pb remaining in the film could give rise to dielectric loss and breakdown at lower fields, particularly if it is electrically continuous between the electrodes.

Table 3-1 Dielectric properties of laser crystallized PZT (30/70) thin films

Film	**1 kHz, 30 mV**	
	Permittivity (ε_r)	**Loss**
Single 300 nm thick layer	**~90**	**0.2**
3-layer deposition/crystallization (total thickness: ~ 300 nm)	**~139**	**0.02-0.04**
4-layer deposition/crystallization (total thickness: ~ 300 nm)	**~167**	**0.01-0.04**

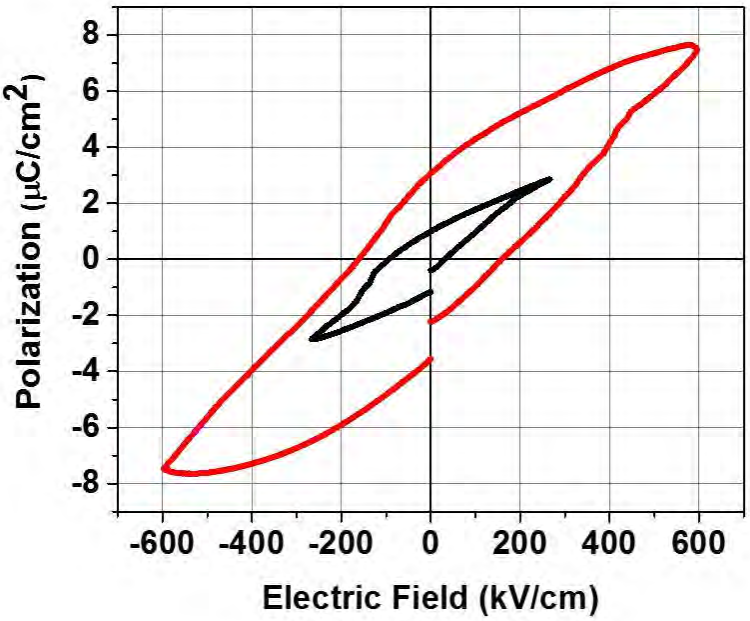

Figure 3-21: Polarization-Electric Field hysteresis loops for ~300 nm thick PZT (30/70) (built with 3 layers of 100 nm each) on Pt/Ti/Cu/EDF (measured at 100 Hz frequency).

To put the permittivity values into perspective, an equivalent capacitance model Figure 3-22 (a) was constructed consisting of a ferroelectric layer and an amorphous dielectric layer in series, to produce a total thickness of 300 nm. A permittivity of 500 for the ferroelectric and 30 for the dielectric were assumed (Caveat: A simplistic model has been considered in this case, wherein the permittivity of the ferroelectric has been assumed to be field independent; however, this permittivity is known to be a function of the dc fields [81]. Furthermore, all of the low dielectric material has been assumed to be at the metal/PZT interface. However, this might not be totally true as the crystalline PZT was seen to be present as an intermix with the low-dielectric constant material as shown in the SEM in Figure 3-14 (a)). In such a scenario, it can be seen that (Figure 3-22 (b)), the permittivity of the stack reduces drastically on increasing the dielectric thickness, such that

a value of 200 is reached for a dielectric thickness of only 30 nm. Equivalently, reduction of the unconverted material thickness steeply increases the total permittivity.

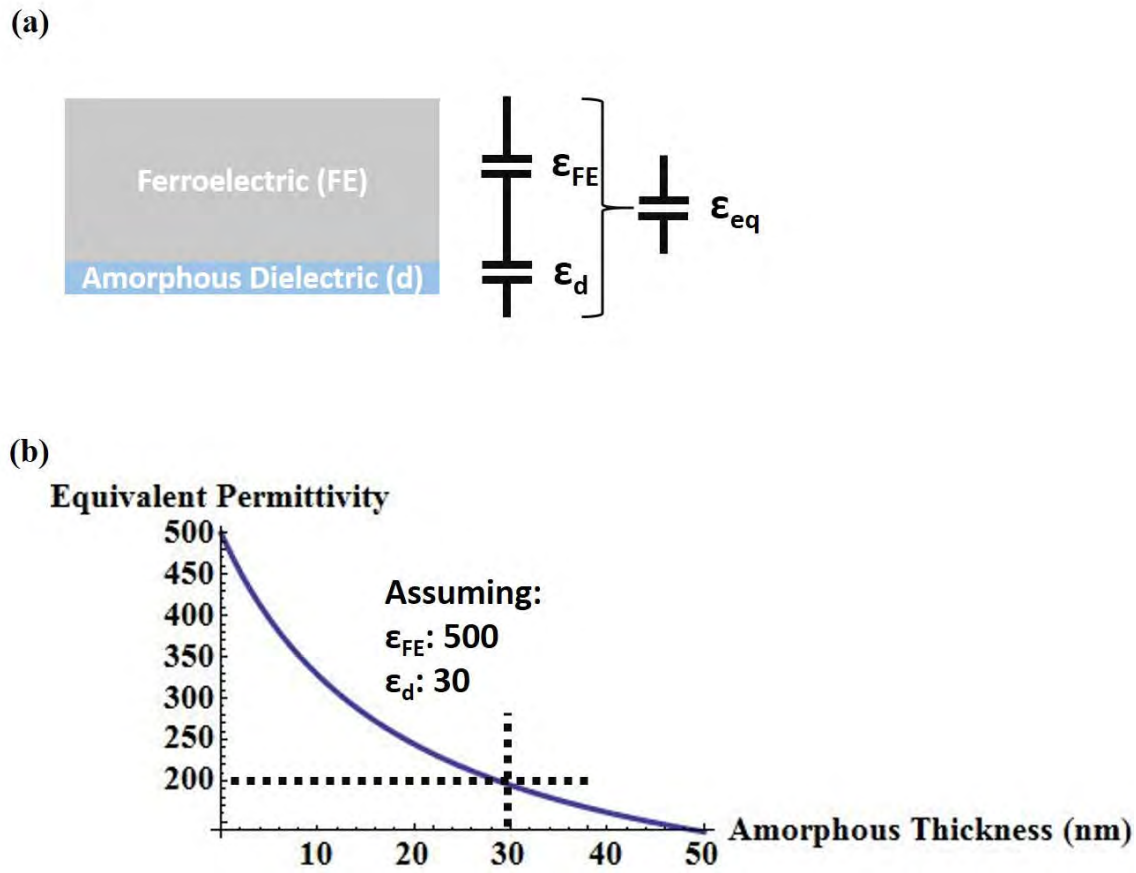

Figure 3-22: (a) Series capacitance model for the ferroelectric stack, and (b) Equivalent permittivity as a function of the amorphous thickness. The total thickness of the stack was fixed at 300 nm.

3.5 Extension of Crystallization to Various Substrates

The crystallization parameters were found to be transferable to different substrate surfaces. Apart from the metallized silicon and EDF substrates considered above, crystallization was also induced in amorphous PZT deposited directly on various amorphous surfaces: uncoated EDF, polyimide and glass substrates. The XRD patterns of laser-induced crystallization in 300 nm PZT 30/70 films on these substrates are shown in Figure 3-23. Note that different X-ray diffractometers with different noise levels were used for these measurements.

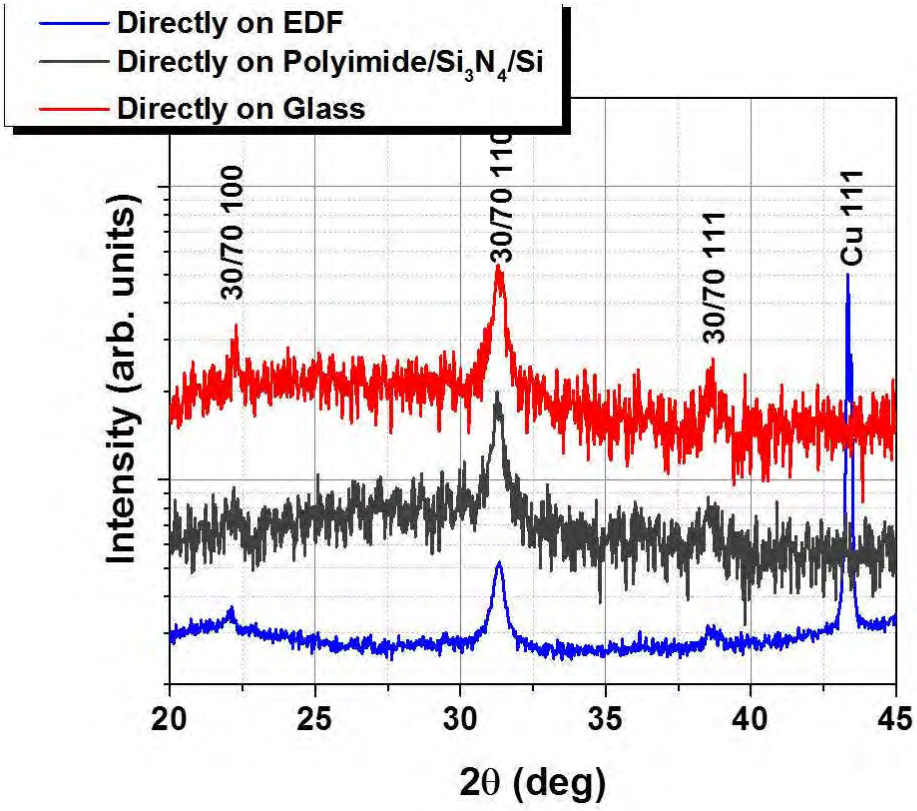

Figure 3-23: XRD patterns of PZT films crystallized directly on EDF, polyimide and glass substrates.

Figure 3-24 shows the surface microstructures of these films. It should be noted that although crystallization was achieved directly on the EDF and polyimide surfaces (i.e., without any metallization and buffer layers), the films cracked heavily; this cracking was not observed for the films on glass.

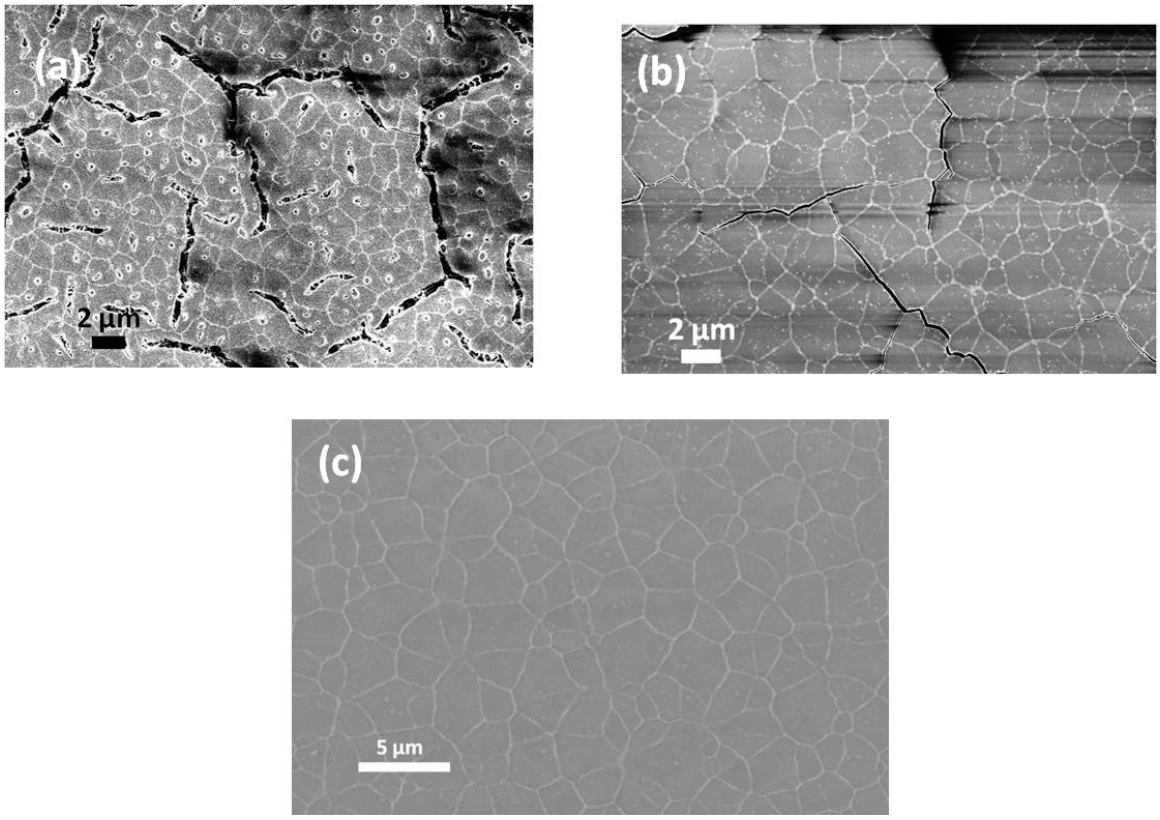

Figure 3-24: Surface microstructures of laser-crystallized PZT on (a) EDF (b) Polyimide and (c) Glass substrates

In order to understand the cracking of PZT films grown directly on polymeric substrates, it may be instructive to consider the differences in the heat flow into the substrate due to varying thermal conductivities of the underlying materials. Silicon substrates, studied in the earlier part of this work has a very high thermal conductivity (152 $Wm^{-1}K^{-1}$ at room temperature) compared to polymeric substrates. For example, polyimide has a room

temperature thermal conductivity of 0.52 $Wm^{-1}K^{-1}$; orders of magnitude less than that of silicon. In addition, the presence of insulating/conducting buffer layers (and their corresponding thicknesses) in between the base substrate and the PZT film also play a role in shielding the base substrate from high temperatures. For instance, in the literature on laser recrystallization of polycrystalline Si on plastic substrates [82], [83], it was hypothesized that irradiation of a film directly deposited on a polymer might cause severe heating of the polymer. This, in turn, may lead to vaporization/ablation of the polymer, or at the very least, a significant thermal expansion. In that work, thick insulating buffer layers (SiO_2) were reported to be necessary to prevent heating of the underlying polymer.

Considering these key factors, a set of thermal simulations were performed and compared to understand the nature of heating response either on a silicon substrate or a polyimide base substrate. The effect of presence or absence of an insulating SiO_2 layer in case of the polyimide substrate was also studied. In particular, pulsed laser heating in these three scenarios were considered (Figure 3-25, Figure 3-26):

1. 300 nm PZT on Pt/Ti/SiO_2/Si
2. 300 nm PZT on Pt/Ti/SiO_2/polyimide
3. 300 nm PZT on Pt/Ti/polyimide (i.e., without the SiO_2 layer)

The thicknesses of the various layers are indicated in Figure 3-25 and Figure 3-26. The SiO_2 buffer layer considered was 1 μm thick. On plotting the evolution of temperature as a function of time at various depths into the sample (Figure 3-25), it can be seen that the maximum surface temperatures reached are the same in all the three cases (about 1400°C), and moreover, temperatures above 600°C are accessible to the same depth as well for all the cases (i.e., about 200 nm). However, the primary differences lay in the time duration

for which the heat stays in the material and the temperature to which the base substrate surfaces are heated to in the three cases. In case of the Pt/Ti/SiO_2/Si substrate, the SiO_2/Si interface is only heated to slightly above 200°C base temperature, however in case of the Pt/Ti/SiO_2/polyimide substrate, the SiO_2/polyimide interface is heated to about 300°C. Without the 1 μm thick SiO_2 layer, the polyimide surface reaches as much as 500°C, highlighting the importance of the insulating buffer layers.

The temperature distribution as a function of depth at various time snapshots was also studied (Figure 3-26). Here again, it can be observed that the temperature distribution inside the PZT layer is more or less the same in the first 50 ns or so of laser irradiation (with the surface temperatures being comparable till up to 500 ns). This is primarily due to the fact that in the first few instants after the laser pulse, heat flow into the substrate is minimal and hence thermal properties of the PZT film play the primary role. However, after about 500 ns, the substrate conduction properties are important and act to keep the heat inside the material in case of low conductivity substrates, such as polyimide. Moreover, it can also be noted that, although the temperatures of the PZT film are roughly back to the background temperature of 200°C in case of silicon base substrate at the end of 10 μs, that is not the case with the polyimide substrates.

These higher temperatures in case of PZT film on the polymeric substrates (without significant buffer layers) would cause large thermal-mismatch stresses between the polymeric layer and the layers above them leading to cracking. Furthermore, gas evolution from the disintegration of the polymeric material could also degrade adherence of the overlying layers [84].

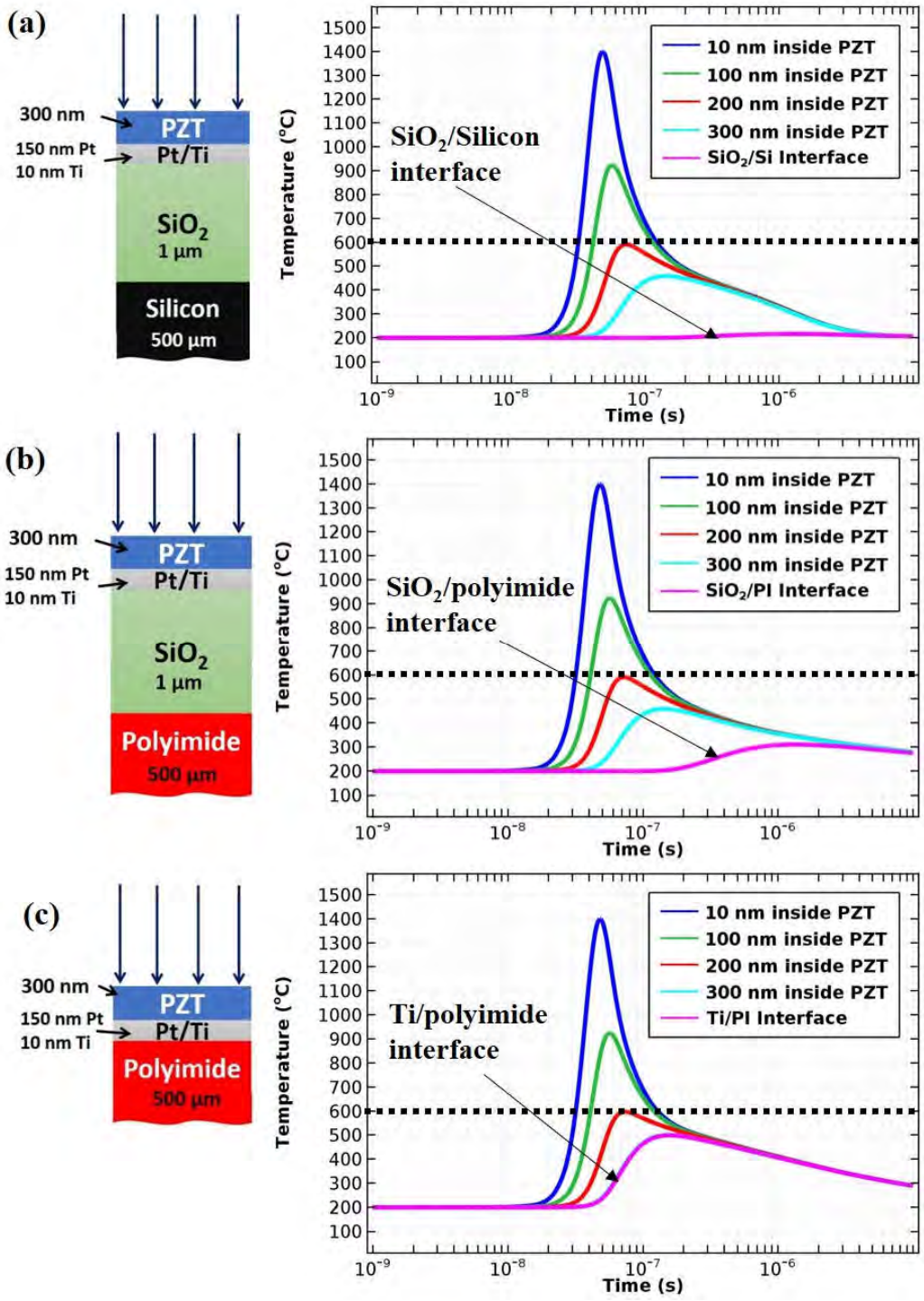

Figure 3-25: Temporal evolution of temperatures at various depths inside PZT film and at the base substrate (Si or polyimide (PI)) surface in case of PZT on (a) Pt/Ti/SiO_2/Silicon (b) Pt/Ti/SiO_2/polyimide and on (c) Pt/Ti/polyimide

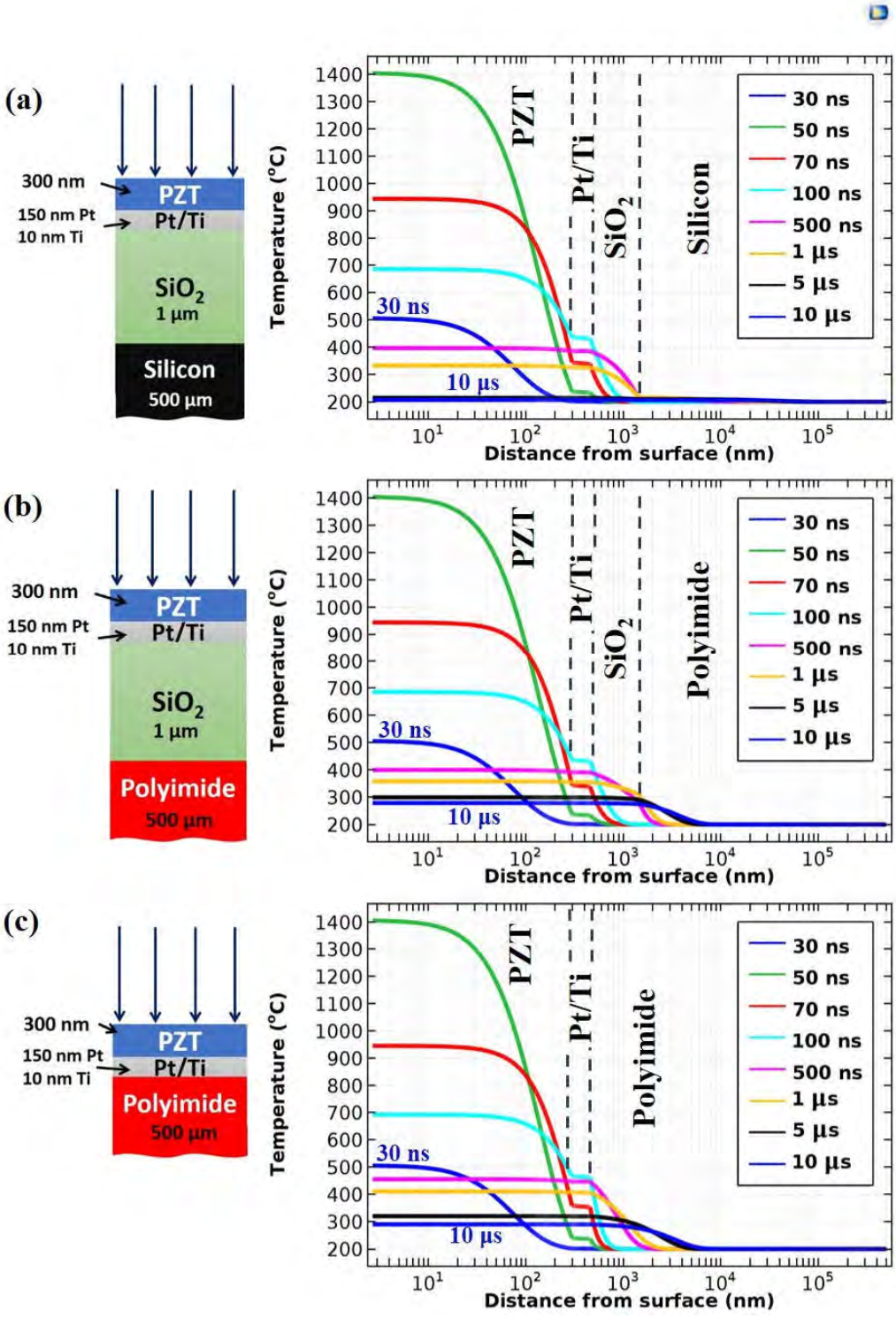

Figure 3-26: Temperature distribution as a function of depth at various time instants after laser irradiation, in case of PZT on (a) Pt/Ti/SiO_2/Silicon (b) Pt/Ti/SiO_2/polyimide and on (b) Pt/Ti/polyimide

3.6 Conclusions

Crystallization of perovskite PZT (30/70) at substrate temperatures of 200 - 215˚C was achieved on polymeric EDF substrates using pulsed laser annealing. Lower roughness of the underlying substrates was a critical parameter in obtaining a continuous PZT film. An ozone ambient was deleterious for crystallization, while an increased PbO content in the films was seen to improve chances of nucleation. Crystallization from the top surface was observed to be thickness limited for 300 nm thick films. Incremental growth and crystallization showed improved through- thickness crystallization. The film Pb content needs to be controlled, coupled with through- thickness crystallization in order to obtain good functional properties.

Chapter 4 *In Situ* Laser-Induced Crystallization of PZT Thin Films

4.1 Introduction

[1]As seen in previous chapters, pulsed laser crystallization allows crystalline $Pb(Zr_{1-x}Ti_x)O_3$ (PZT) based ferroelectric thin films to be prepared at low substrate temperatures [85],[41],[44]. Moreover the limitation of thermal penetration depth can be overcome by carrying out layer-by-layer crystallization and growth. It is notable, however, that, some PZT (52/48) thin film MEMS applications require thicknesses >1 μm [86] and sequential growth and annealing significantly reduces the possibility of high throughput. Simultaneous laser annealing during film growth offers a possibility for *in situ* crystallization of thicker films at low substrate temperatures for a wide range of Zr:Ti ratios in PZT films. This would facilitate industrial scaling of the process. Moreover, *in situ* heat treatment of oxide thin films during growth can also benefit from reduced crystallization temperatures compared to a post-deposition thermal processing [87],[88].

Previous studies by Tabata *et al.* demonstrated $PbTiO_3$ thin films grown on $SrTiO_3$ substrates using pulsed laser deposition (PLD) with *in situ* laser excitation using an ArF excimer laser (193 nm wavelength) at a substrate temperature of 350˚C [58]. However, with an increase in Zr content in the film (as would be required for PZT at the morphotropic phase boundary, MPB), an increase in the growth temperature is expected [89]. In other perovskites, Ito *et al.* reported good optical properties in Co-doped $BaTiO_3$ thin films

[1] Parts of the results in this chapter were previously reported in:
A. Rajashekhar et al., *Applied Physics Letters* 103, no. 3 (2013): 032908

grown by PLD at 650˚C with *in situ* KrF laser annealing on an MgO substrate [90]. This chapter investigates *in situ* laser annealing and growth of PZT thin films below 400˚C (compatible with complementary metal oxide semiconductor (CMOS) read-out/driving circuits, and polyimide polymeric substrates) with good electrical properties. Laser annealing also allows development of texture in $Pb(Zr_{0.52}Ti_{0.48})O_3$ (PZT (52/48)) to achieve excellent piezoelectric properties [51]. Hence, the possibility of orientation control by the *in situ* laser annealing and growth is investigated.

In this work, the pulsed laser deposition (PLD) system with *in situ* laser annealing capabilities described in Chapter 2 has been utilized for *in situ* crystallization of the growing film. *In situ* laser annealing during growth was carried out using a PZT (52/48) target, with 20% excess PbO to compensate for Pb loss during deposition. A 10% ozone, 90% oxygen mixture was used as an ambient gas at pressures between 70 and 120 mTorr. The laser pulse frequency used was 20 Hz, with a target-substrate distance of 7.2 cm, while the substrate temperature was maintained between 350 and 380˚C. The ablation and annealing laser fluence values were respectively ~1.2 J/cm^2 and ~55 mJ/cm^2. With these conditions, the growth rate achieved was about 0.1 Å/pulse. Substrates used included (111) $Pt/Ti/SiO_2/Si$ wafers obtained from Nova Inc., and (100) $SrTiO_3$ (STO) single crystals from Crystec GmbH. In the case of the platinized silicon wafers, three types of template layers were utilized: a crystallized PZT (20/80) layer (a PLD deposited ~60 nm film, laser crystallized at a substrate temperature of 375˚C), a {111} PZT (30/70) layer and a PZT (52/48) layer (both around ~60-70 nm, and prepared by chemical solution deposition [91] and rapid thermal annealed at 650˚C for 1 min). In the first two cases, Ti-rich compositions

were chosen for seed layer preparation owing to easier nucleation as compared to Zr-rich PZT [26].

4.2 Characterization of Pulsed Laser Growth and Crystallization System

In order to characterize the experimental setup, a first set of films was grown without utilizing laser annealing. The system is capable of substrate rotation (with 10 rpm) to facilitate larger area deposition with improved thickness homogeneity. In order to characterize this, the spatial thickness variability in as-deposited amorphous films (coated at room temperature) was compared for growths with and without substrate rotation (Figure 4-1 & Figure 4-2). As can be clearly seen, a smaller percentage variation (average thickness: 383 nm, standard deviation: 16 nm; across a ~55 mm long wafer) is observed for the sample deposited with substrate rotation as opposed to the one without rotation (average thickness: 515 nm, standard deviation: 161 nm; across a ~55 mm long wafer). The average thickness is lower when substrate rotation is utilized as the surface coverage of the substrate is increased, while any single area spends less time in the deposition plume.

The lateral uniformity of the elemental composition for the as prepared films grown with substrate rotation was also studied. Figure 4-3 shows the composition analysis as a function of the lateral distance from the trajectory of the plume. It can be seen that as the distance from the center of the plume increases, the Pb/(Zr+Ti) ratio decreases by about 25% on going away by about 20 mm from the plume center, pointing to the possibility of Zr and Ti species being scattered out of the plume, hence enriching the lighter elements at the periphery, while retaining more Pb near the center [92].

Subsequent crystallization of these films using rapid thermal annealing at ~650°C yielded crystalline films as shown in Figure 4-4(a). The dielectric permittivity (permittivity (ε_r): ~1100, loss tangent (tan δ): 0.02 at 10 kHz, 30 mV_{rms}) and ferroelectric properties (remanent polarization (P_r): 22 C/cm^2, coercive field (E_c): 36 kV/cm) (Figure 4-4(b)) are comparable to those reported in the literature for PZT at the morphotropic phase boundary [80]. Considering these results, for further growth experiments with *in situ* laser annealing, substrate rotation was primarily utilized (unless otherwise required, for microfocus XRD measurements which will be discussed later in a section). A laser fluence in the range 1-2 J/cm^2, a target-substrate distance of 5 cm to 7.2 cm, a pO_2 of 50 – 120 mTorr (with 10% O_3) has been utilized in the majority of the work on *in situ* laser annealing.

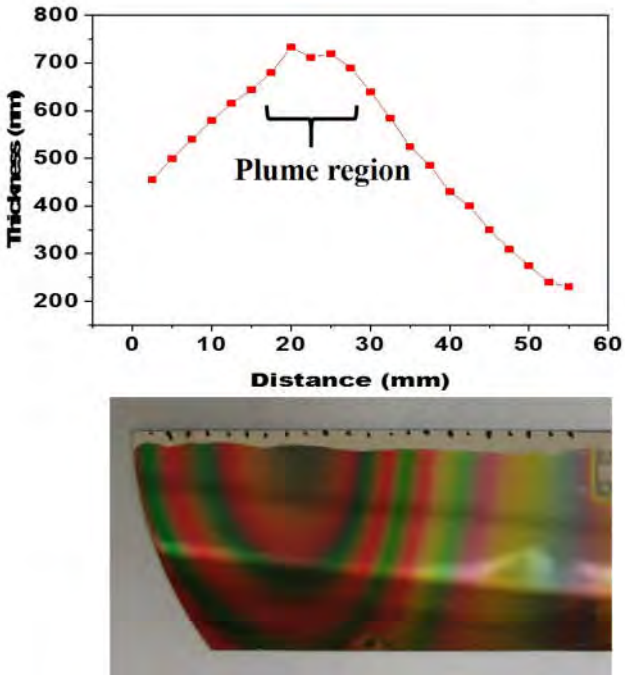

Figure 4-1 Thickness profile of an as deposited PZT (52/48) film (grown without laser annealing and without substrate rotation) (Substrate temperature: 20°C, Fluence: ~1.6 J/cm², Target-substrate distance: 7.2 cm, Freq: 15 Hz, Duration: 25 min, pO_2: 50 mTorr (10% O_3)). The non-circular thickness fringes are believed to be due to a finite wobbling of the target holder. The ticks on the scale are spaced at 2 mm.

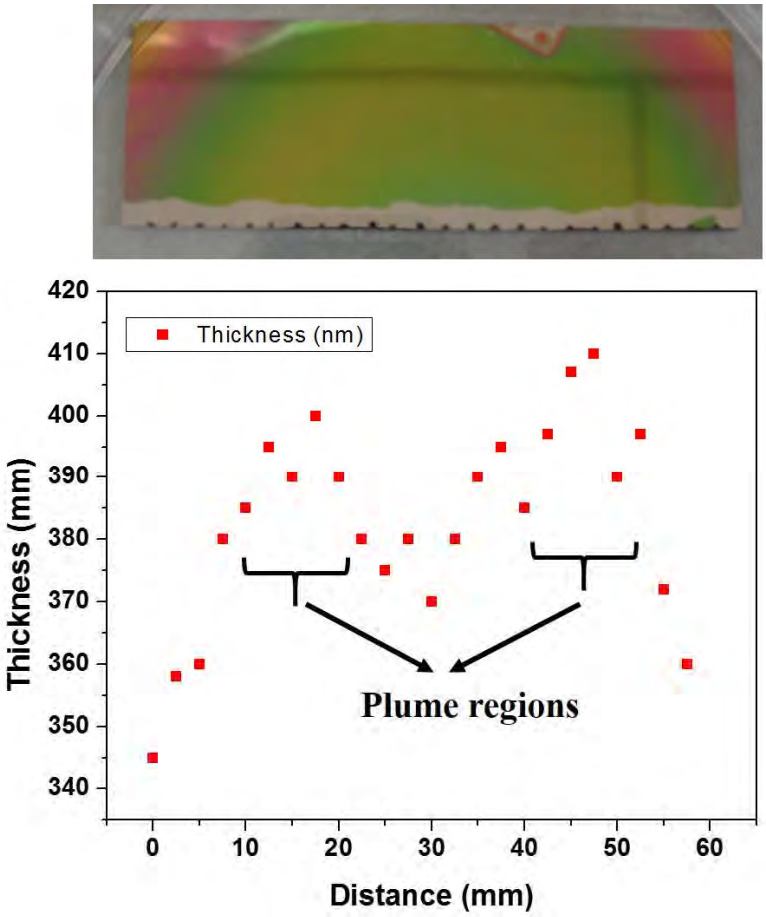

Figure 4-2 Thickness profile of an as deposited PZT (52/48) film (grown without laser annealing but with substrate rotation) (Substrate temperature: 20°C, Fluence: ~1.6 J/cm^2, Target-substrate distance: 7.2 cm, Freq: 15 Hz, Duration: 25 min, pO_2: 50 mTorr (with 10% O_3)). The ticks on the scale are spaced at 2 mm.

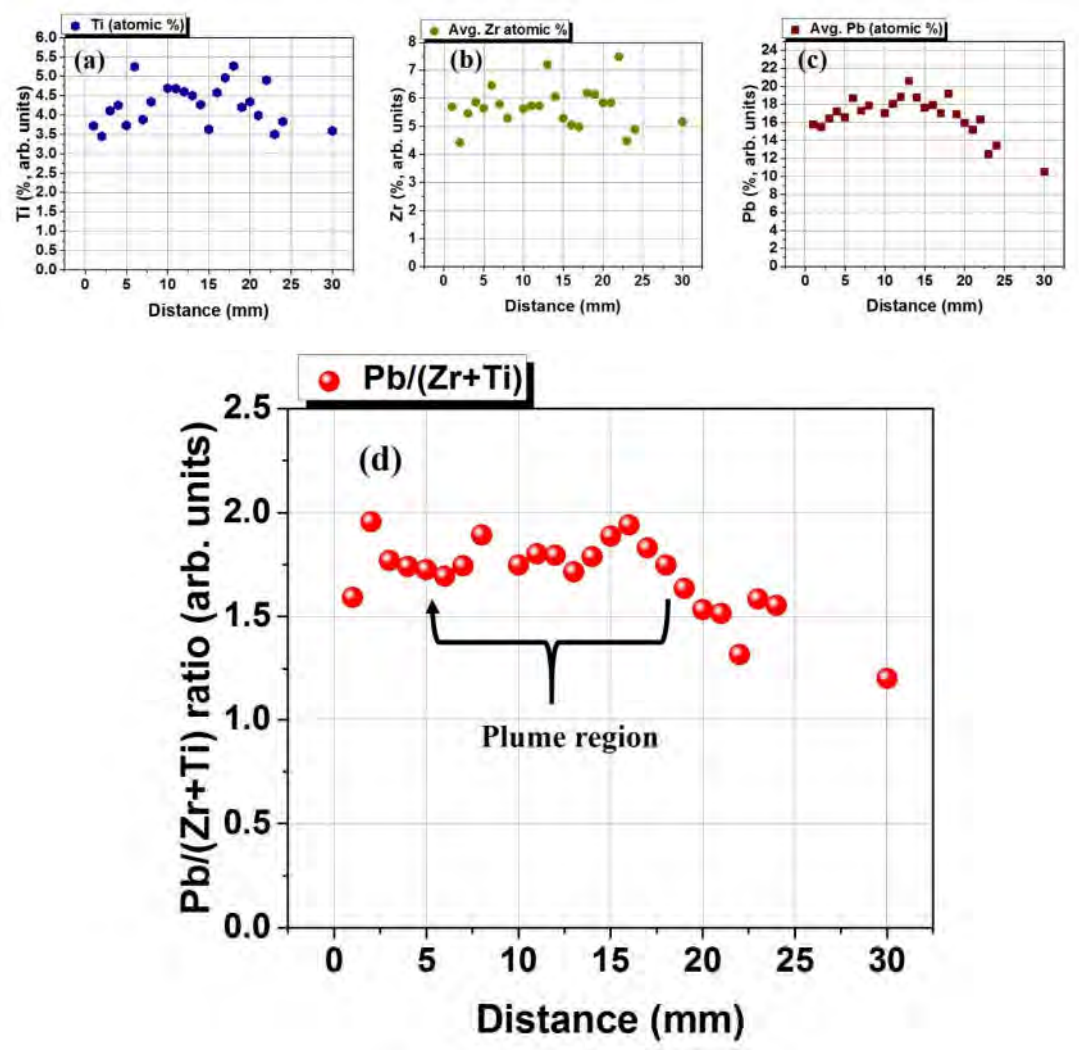

Figure 4-3: Elemental composition (a) Ti, (b) Zr, (c) Pb as evaluated by energy dispersive analysis of X-rays (EDAX). The % values are in arbitrary units. The Pb/(Zr+Ti) ratio is shown in (d). No substrate rotation was utilized. The substrate temperature: 20°C, Fluence: ~1.6 J/cm^2, Target-substrate distance: 7.2 cm, Freq: 15 Hz, pO_2: 50 mTorr (with 10% O_3)

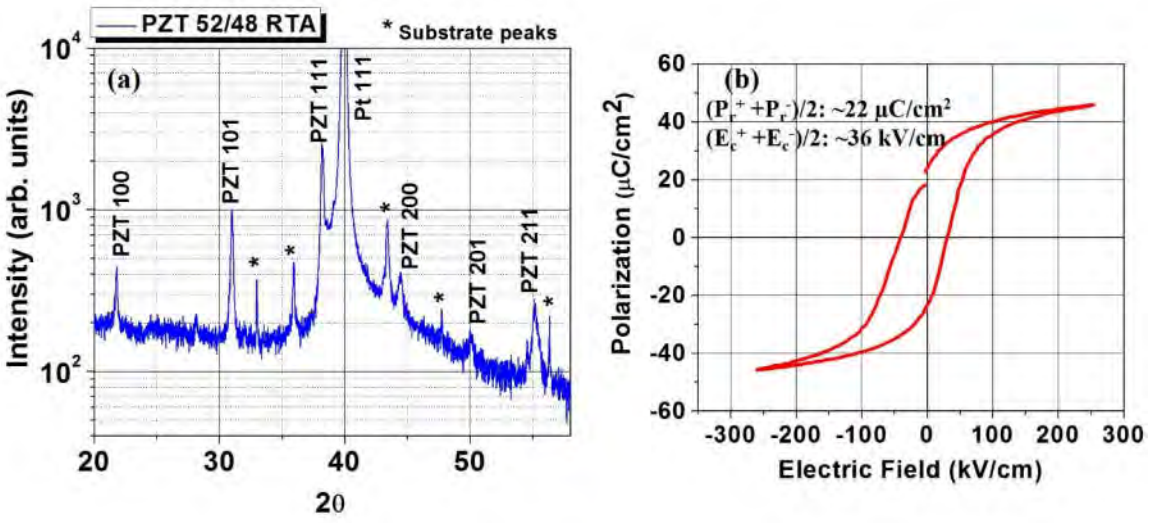

Figure 4-4: (a) XRD and (b) Polarization-Electric Field hysteresis loop (100 Hz) of a PZT (52/48) film deposited at 20°C, and rapid thermally annealed at 650°C. The average polarization ($(P_r^+ + P_r^-)/2$) and coercive field ($(E_c^+ + E_c^-)/2$) are indicated. The dielectric properties of the film measured at 10 kHz, 30 mV_{rms} were a permittivity (ε_r) ~1100, loss tangent (D): 0.02

4.3 *In Situ* Laser Crystallization of PZT (52/48) Thin Films

Growth of PZT (52/48) directly onto (111) Pt coated Si substrates with the *in situ* laser annealing conditions explored in this chapter (at substrate temperatures in the range of 300 - 380˚C) resulted in predominantly pyrochlore/fluorite phases. These films could be converted to a single phase perovskite phase on rapid thermal annealing at 650˚C (as confirmed by XRD and FESEM (Figure 4-5)), suggesting that they are not lead deficient.

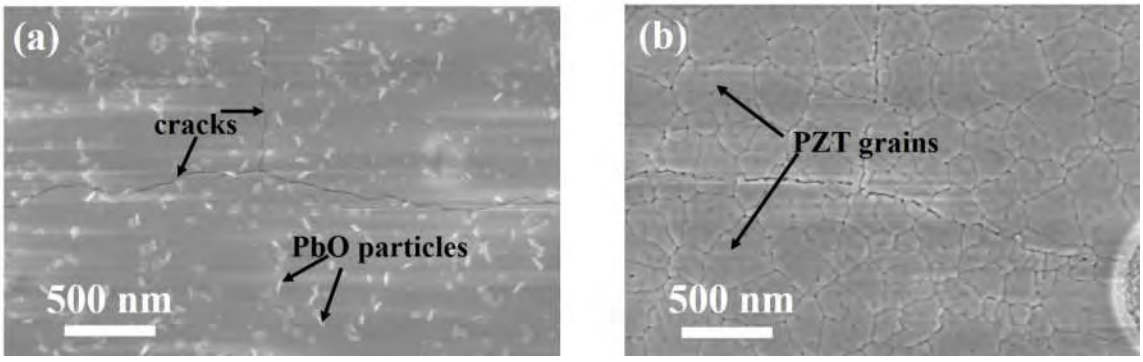

Figure 4-5: PZT films (a) as laser annealed on platinized silicon substrate (ablation fluence: ~1.2 J/cm^2, pO_2: 70 mTorr (10% O_3), annealing energy density: ~55 mJ/cm^2, target-substrate distance: 7.2 cm, substrate temperature: ~370°C and (b) subsequently rapid thermally annealed at 650° C for 1 min, revealing PZT grains. The origin of cracks in the as deposited film is not well understood and could be due to growth stresses as will be discussed in the subsequent chapters.

It is known that crystallization of PZT is a nucleation limited process [93],[41]. Hence a crystallized seed-layer was utilized to aid nucleation during *in situ* laser annealing. For the purpose of maintaining a low process temperature throughout, laser crystallization of the seed layer was adopted. First, an amorphous seed layer of PZT (20/80) (~60 nm thick) was deposited by PLD at ~200˚C. The film was then *ex situ* laser crystallized at 375˚C substrate temperature and a pO_2 of 100 mTorr, by using ~600 laser pulses with an energy density of ~50 mJ/cm^2. The evolution of crystallization of the seed layer with increasing number of laser pulses is shown in Figure 4-6.

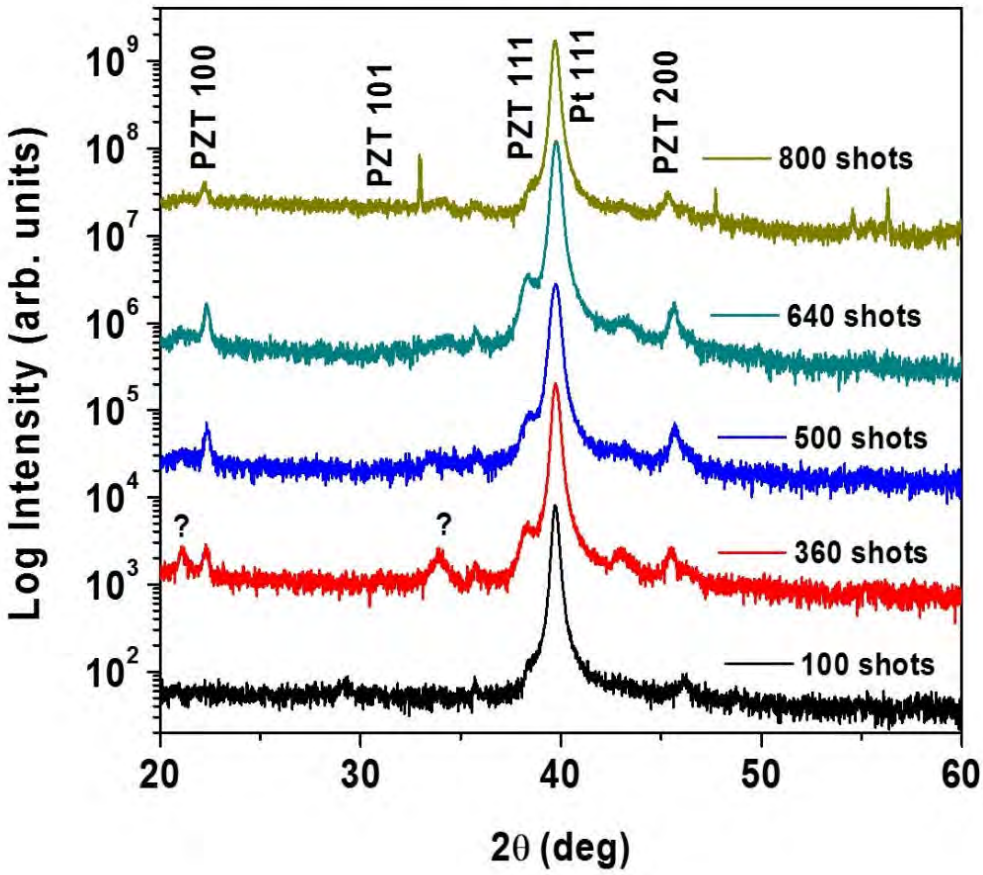

Figure 4-6: Phase evolution of laser crystallized PZT (20/80) seed layer with increased number of laser pulses. A range of 500 to 640 pulses was chosen as the optimum condition (The peaks marked with '?' point to unidentified phases).

Subsequently, a PZT (52/48) thin film was grown on the seed layer under *in situ* laser annealing conditions. Figure 4-7 shows the XRD pattern of an *in situ* laser annealed PZT (52/48) film (~1.1 μm thick) grown on the laser crystallized PZT (20/80) seed layer. The PZT (52/48) thin film is polycrystalline, as was the seed layer. It is clear that the seed-layer enables nucleation and growth of the perovskite phase. Figure 4-8 (a) and (b) show the surface and fracture cross-section FE-SEM images of the film. The surface morphology

showcases extremely fine grain-sizes (on the order of 30 nm), and points to a high nucleation density at the seed layer – thin film interface. In addition, the cross-sectional image reveals columnar growth.

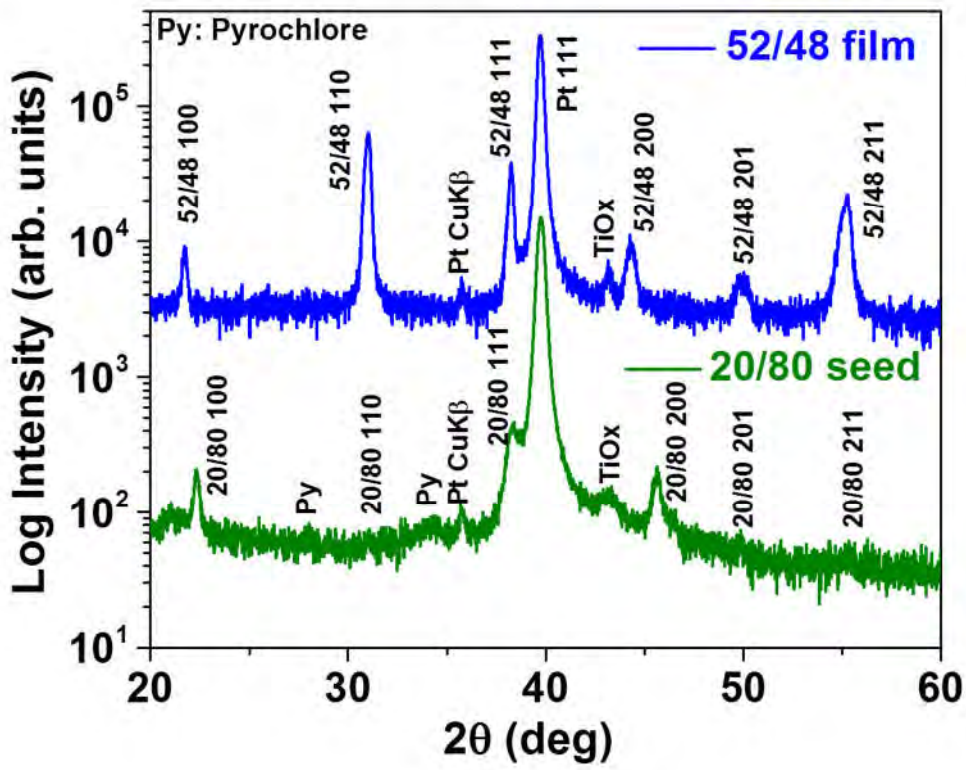

Figure 4-7: XRD patterns of *in situ* annealed PZT (52/48) on a laser crystallized 20/80 seed. The TiO_x peaks are from the Ti layer in the platinized silicon substrate.

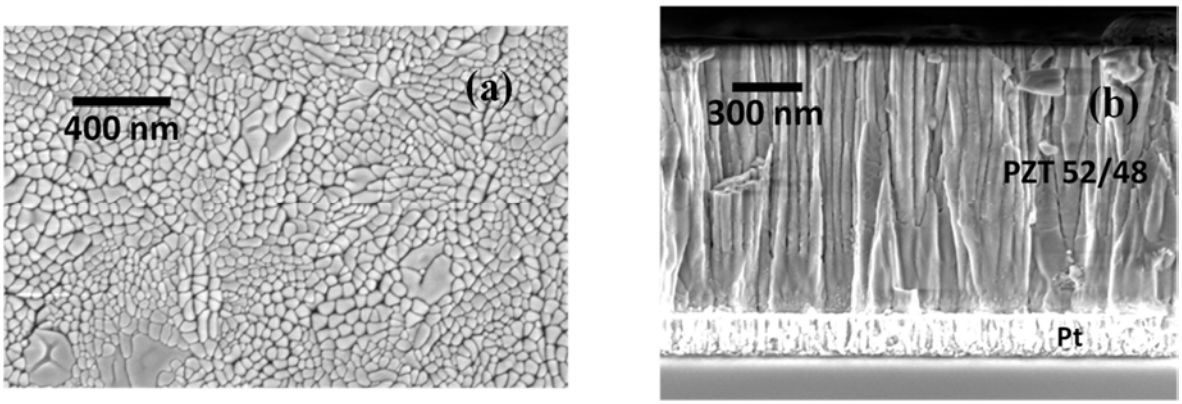

Figure 4-8 (a) Surface FE-SEM of the *in situ* laser annealed PZT (52/48) film on laser crystallized 20/80 seed and (b) the corresponding fracture cross-sectional FE-SEM

4.4 Characterization of the Laser Crystallized Region

The crystallization was characterized using micro-focus XRD in order to understand the effect of the laser pulse as well as the gradation in laser energy density near the periphery of the irradiated area (i.e. on the border of the laser spot which is of the order of 1 cm by 0.8 cm). Figure 4-9 and Figure 4-10 show the micro-focus XRD patterns and the surface FESEM's of a region deep within the laser spot and another at the periphery of the laser spot, respectively. As expected, the central region is well crystallized into perovskite PZT, while the periphery is partially crystallized, with the presence of the pyrochlore phase in the XRD peaks.

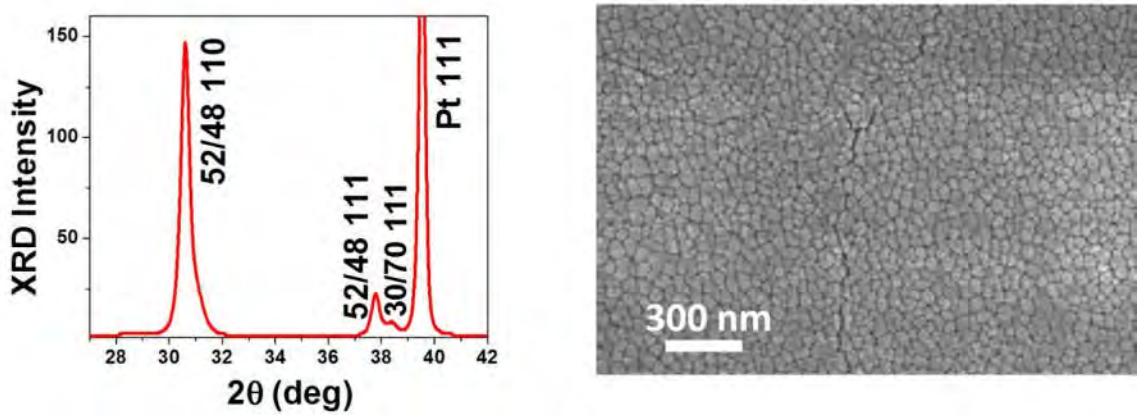

Figure 4-9: Micro-focus XRD from the central laser crystallized region (deep within the laser spot). No substrate rotation was used during the deposition.

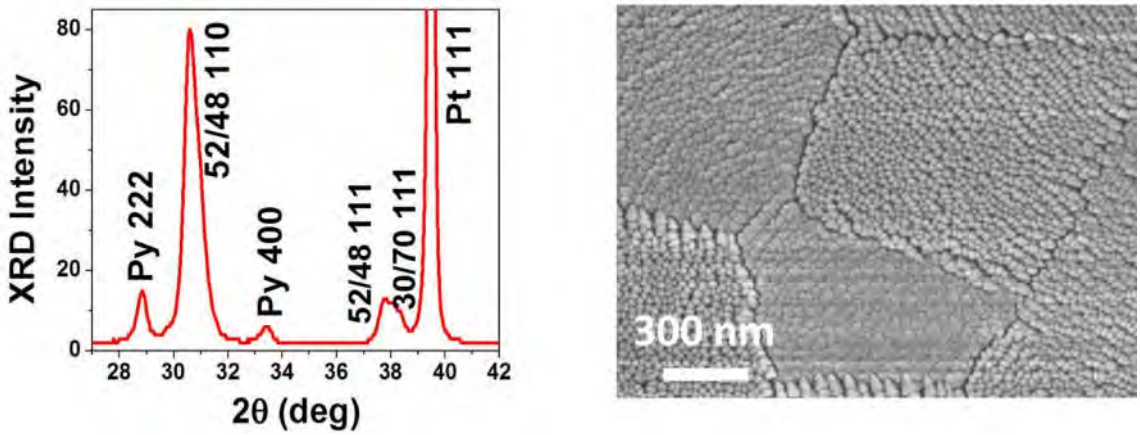

Figure 4-10: Micro-focus XRD from the periphery region of the laser spot. No substrate rotation was used during this deposition. Py = pyrochlore

4.5 Orientation Matching with the Substrate

4.5.1 Crystallization on {111} Oriented PZT (30/70) Seed Layers

The fact that nucleation is preferred at the substrate offers the opportunity to control the orientation of the grown film. As a result, it was found that *in situ* laser annealing during growth on {111} PZT (30/70) seed layers produced {111} oriented PZT (52/48) (Figure

4-11 (a)). Again, the surface and cross-sectional FE-SEMs (Figure 4-11 (b) and (c)) confirm a high nucleation density with fine columnar grains (on the order of ~30 nm diameter) as was noticed in films on laser crystallized seed layers.

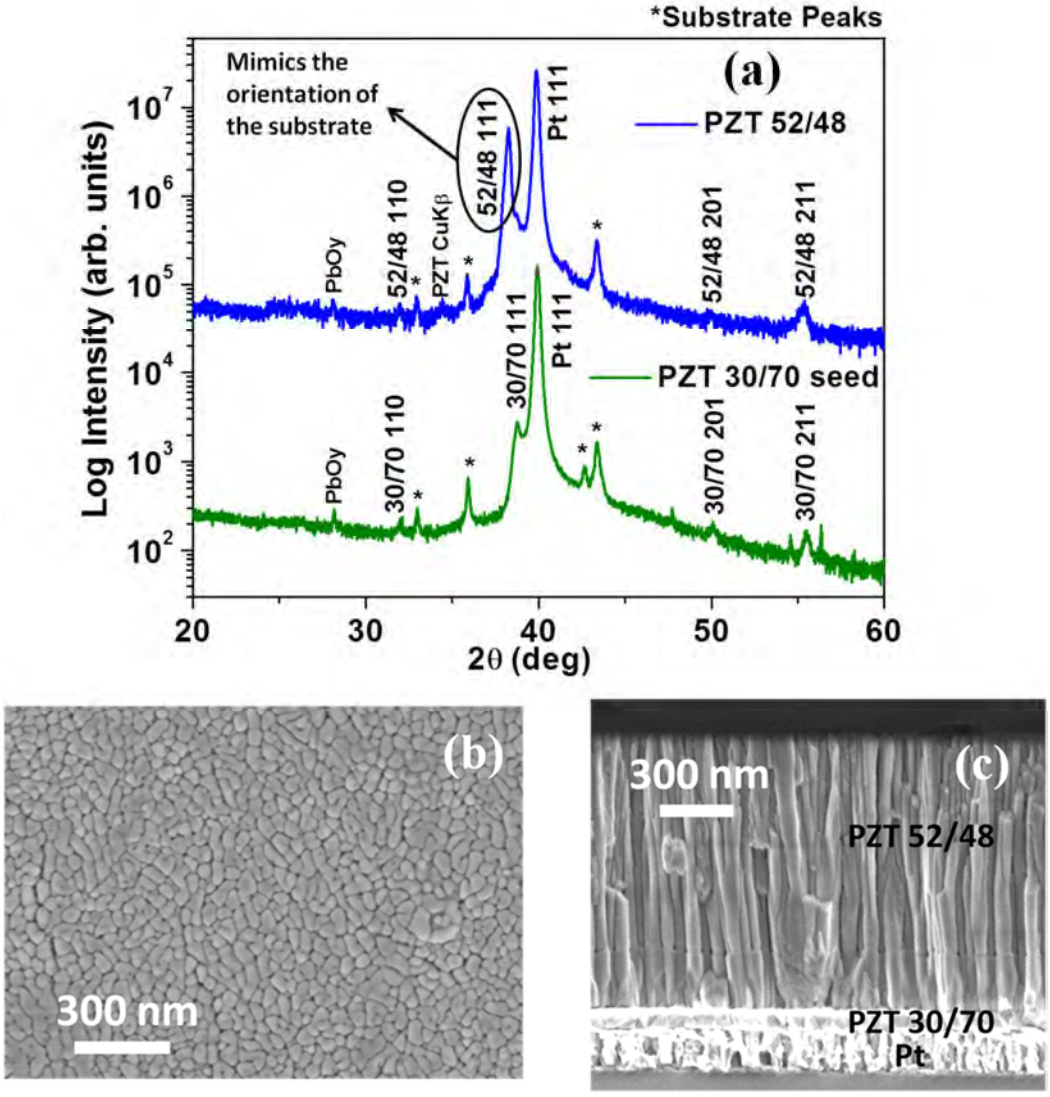

Figure 4-11: (a) XRD of the *in situ* annealed PZT (52/48) on (111) sol-gel (30/70) seed layer. (b) & (c) are the corresponding surface and cross-sectional FE-SEM of the same film

4.5.2 Crystallization on (100) $SrTiO_3$ (STO) Single Crystalline Substrates

In addition, depositions were also carried out on (100) $SrTiO_3$ (STO) single crystal substrates. A two step *in situ* laser annealing process was adopted. First 50 nm of the PZT (52/48) film was grown with an *in situ* laser annealing energy density of 72 mJ/cm^2 (at a pO_2 of 70 mTorr and a substrate temperature of 350˚C) in order to obtain a smooth oriented seed layer devoid of pyrochlore/fluorite phase (Surface FESEM shown in Figure 4-12). Further growth with *in situ* laser annealing at 350˚C yielded dense and epitaxial PZT films (as shown by the XRD scan, rocking curve about the 200 peak and phi scan of the 110 peak depicted in Figure 4-13 and Figure 4-14). However, these films were found to crack at thicknesses of about 200 nm (Figure 4-15 and Figure 4-16). Hence, *in situ* laser annealing and growth of PZT (52/48) was completed on the seed layer at a slightly higher temperature (440˚C) than used in the experiments mentioned above, with an energy density of ~55 mJ/cm^2 and a pO_2 of 110 mTorr. This yielded a crack free, {001} oriented PZT film (Figure 4-17). A ~340 nm crack-free film was grown at 440˚C (Figure 4-17 (b) and (c)). Figure 4-17 (c) shows a dense growth front until about 200 nm, beyond which there seems to be a change in the growth mode, such that the film appears slightly porous and granular. Further optimization is necessary to grow thick oriented films on single crystalline substrates.

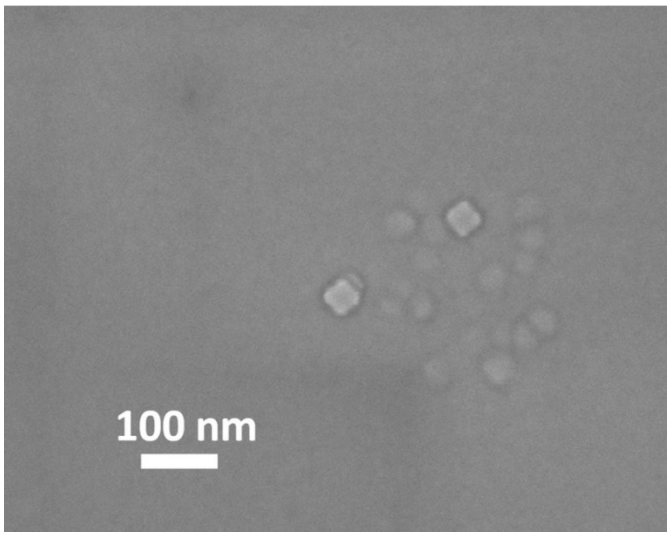

Figure 4-12: Seed layer FESEM plan view for ~50 nm thick PZT on STO (001). The seed layer was smooth, with few surface features.

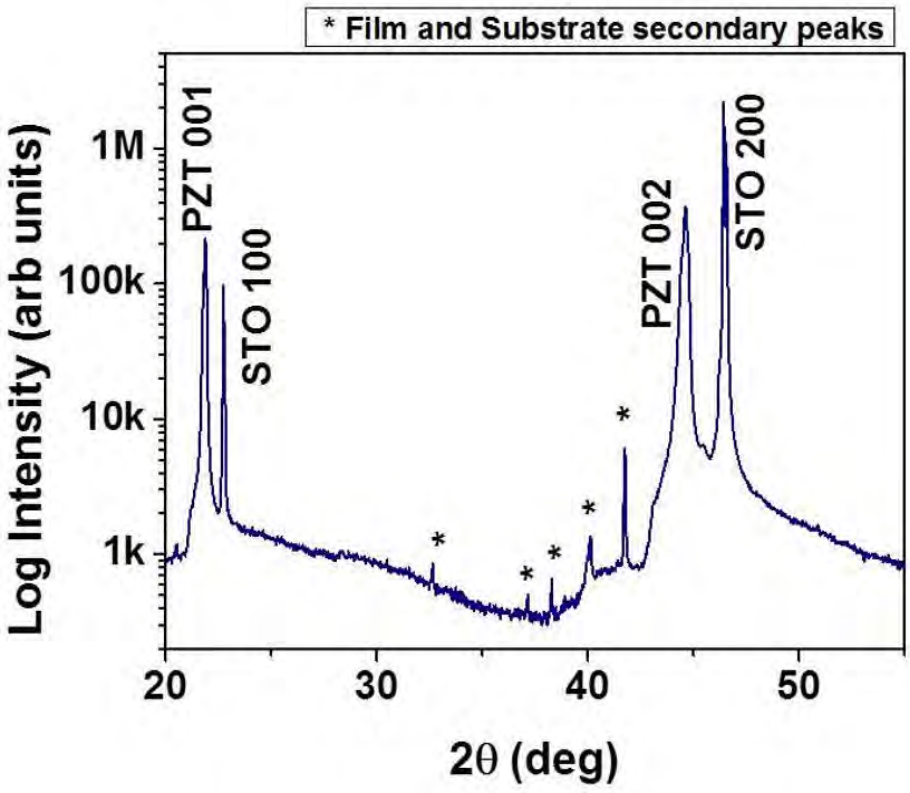

Figure 4-13: XRD of the *in situ* annealed PZT (52/48) on a (100) $SrTiO_3$ single crystal deposited at ~350°C substrate temperature.

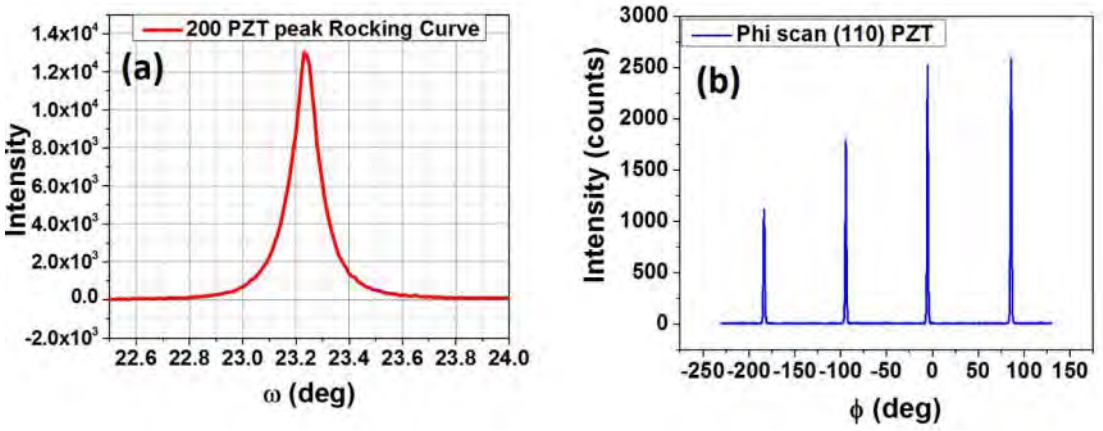

Figure 4-14: Rocking curve about 200 peak (a) and Phi scan of 110 peak (b) of the *in situ* annealed PZT (52/48) on a (100) $SrTiO_3$ single crystal deposited at ~350°C substrate temperature.

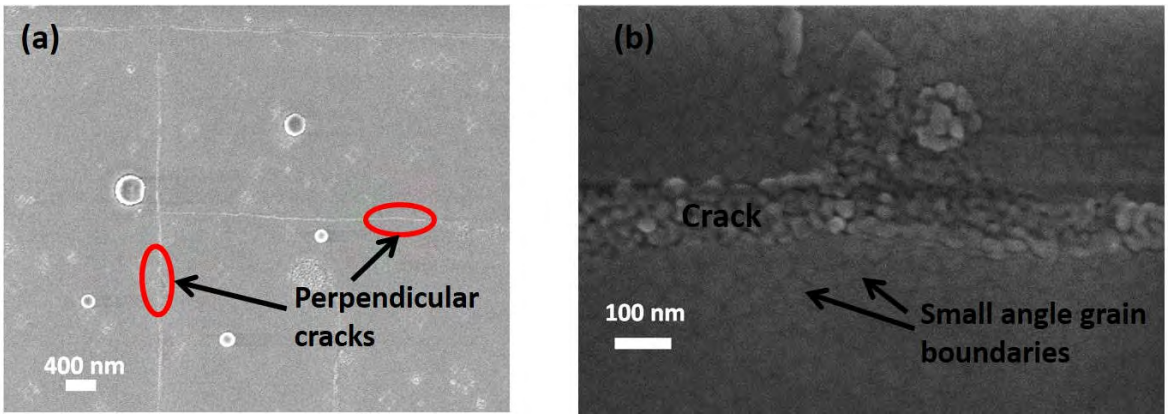

Figure 4-15 (a) & (b) FESEM surface plan view of PZT on STO at different magnifications. The perpendicular cracks are labeled, while small grains and grain boundaries appear, as shown in (b).

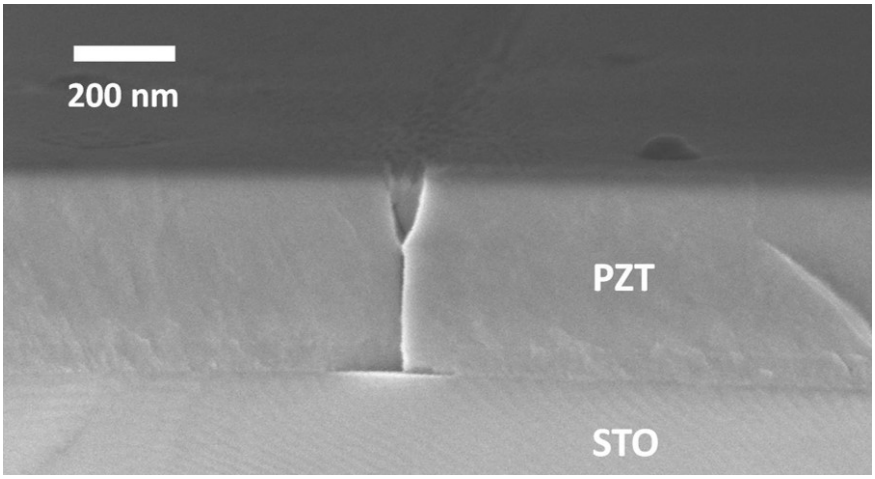

Figure 4-16: FESEM Cross-section of PZT on STO deposited at ~350°C substrate temperature. (Substrate temperature: 350°C, Fluence: ~1.6 J/cm^2, Target-substrate distance: 7.2 cm, Freq: 20 Hz, pO_2: 50 mTorr (with 10% O_3)). Through-thickness cracks develop at around 200 nm thickness.

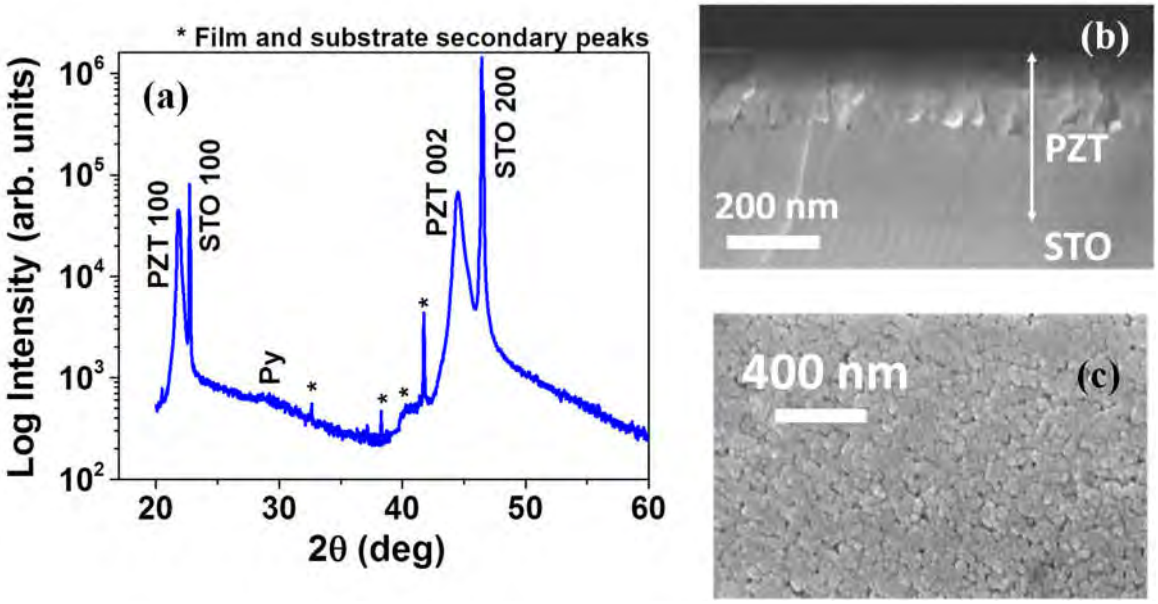

Figure 4-17: (a) XRD of the *in situ* annealed PZT (52/48) on a (100) $SrTiO_3$ single crystal deposited at 440°C substrate temperature. Cross-sectional (b) and surface (c) FE-SEM of the same film

The possibility of cracking due to the large thermal gradient between the laser heated surface and the underlying material was explored. A sputtered 1 μm thick PZT (52/48) film that was crystallized using a rapid thermal annealer at 650°C for 1 min was subjected to ~1000 laser pulses of ~60 mJ/cm^2 (this is on the higher end of the energy density used in *in situ* laser annealing). The film was not found to crack, which confirms that thermal shock is not the cause of cracking in *in situ* laser annealed films. Some thermal grooving could be observed at the grain boundaries; this was attributed to laser-induced evaporation of excess PbO segregated at the grain boundaries [27].

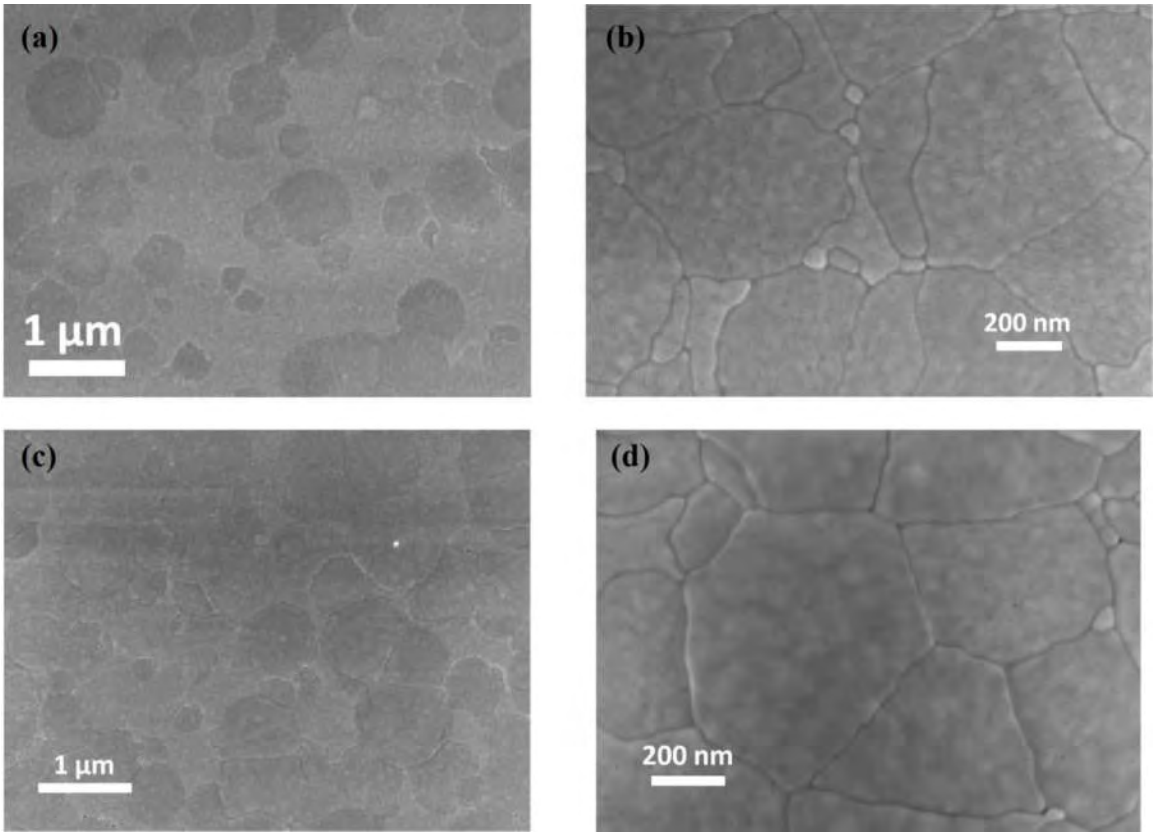

Figure 4-18: (a) & (b) Surface FESEM's of an as-RTA'd PZT thin film on STO (001) substrate at different magnifications. (c) & (d) Surface FESEM's of a laser exposed (~60 mJ/cm^2) RTA'd PZT thin film on STO (001) substrate. No cracks were seen to develop on laser exposure, while some thermal grooving of the grain boundaries was observable, possibly due to evaporation of excess PbO at the grain boundaries.

4.6 Electrical Properties

The frequency dependence of the dielectric properties, polarization-electric field hysteresis loops, and permittivity-electric field data for a 1.1 μm thick, *in situ* laser annealed, PZT (52/48) film on a laser crystallized PZT (20/80) seed (on platinized silicon base substrate; phase formation and microstructure reported in Figure 4-7 and Figure 4-8) are shown in Figure 4-19 (a)-(c). The film exhibits a dielectric loss of less than 2.5% at 10 kHz. The effective permittivity of the PZT (52/48) on PZT (20/80) seed is ~730. Polarization-electric field hysteresis measurements show well-saturated loops with a remanent polarization ~25 $\mu C/cm^2$ and a coercive field ~50 kV/cm. Ferroelectric switching is also apparent from the permittivity and loss tangent response to dc bias (Figure 4-19 (c)). Thus, the electrical properties of laser annealed film prepared at a substrate temperature below 400˚C are comparable to conventionally prepared films.

It is expected that the dielectric and piezoelectric properties should be optimized when the film as well as the seed layer consists of the MPB composition. A 420 nm PZT (52/48) film grown with *in situ* laser annealing on a ~70 nm PZT (52/48) sol-gel crystallized seed layer displayed a permittivity and loss of 970 and 2.3% respectively (at 1 kHz and 30 mV_{rms}). On poling at three times the coercive field for 20 min at room temperature, an $e_{31,f}$ of around -3.5 C/m^2 was measured. The $e_{31,f}$ value increased to about -6.1 C/m^2 on poling at 150˚C and can be attributed to thermal activation of domain wall mobility in the fine grain structure. The electrical properties of the PZT (52/48) films on the PZT (20/80), PZT (30/70) and PZT (52/48) seed layers are summarized in Table 4-1.

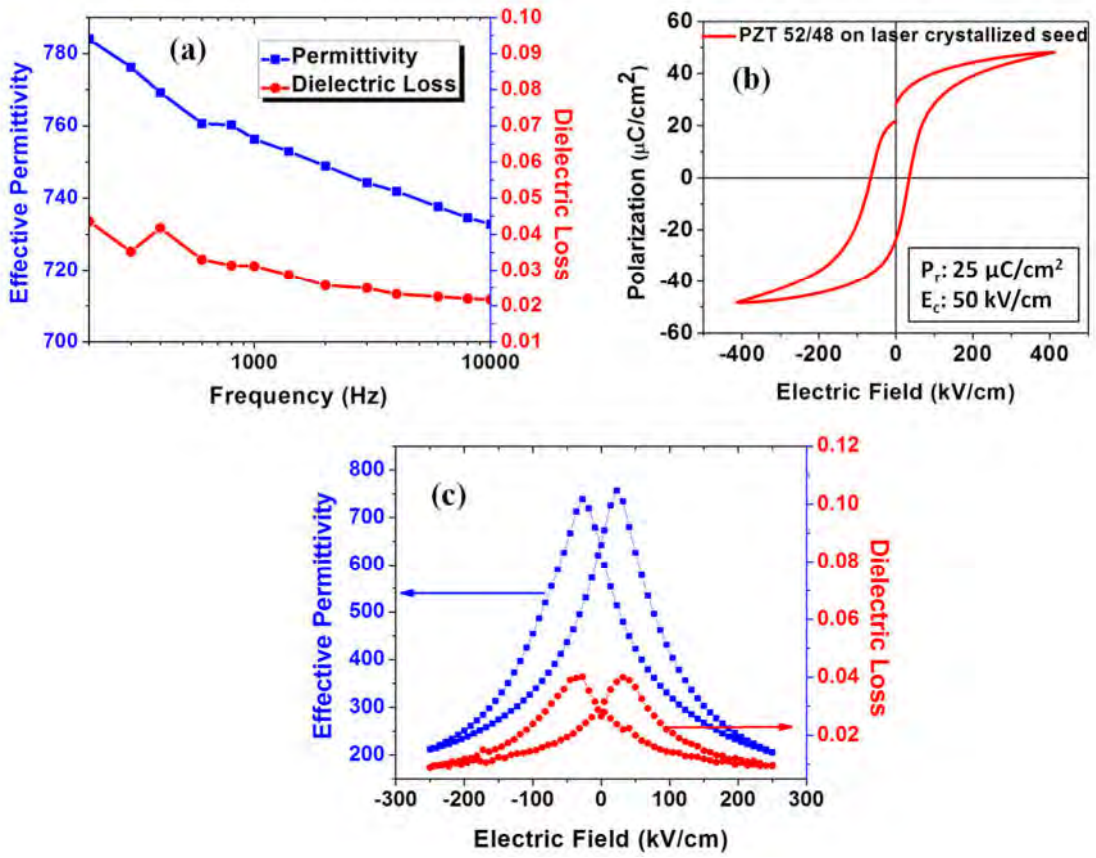

Figure 4-19: Dielectric properties of the *in situ* laser annealed PZT (52/48) film on laser crystallized PZT (20/80) seed layer.

Table 4-1: Dielectric properties of PZT (52/48) films prepared by the *in situ* laser annealing technique on various seed layers.

Film	Permittivity (Loss) (1 kHz, 30 mV_{osc})	Remanent Polarization ($\mu C/cm^2$)	Coercive Field (kV/cm)	$e_{31,f}$ (poling at 150˚C) (C/m^2)
PZT (52/48) on (20/80)	756 (0.03)	25	50	--
PZT (52/48) on (30/70)	876 (0.025)	25	38.5	--
PZT (52/48) on (52/48)	970 (0.023)	16	38	- 6.1

4.7 Conclusions

In summary, a pulsed laser deposition system enabling *in situ* laser annealing during growth was designed and built. *In situ* laser annealing during PZT film growth was nucleation limited. It was demonstrated that micron thick perovskite PZT (52/48) films could be grown at substrate temperatures below 400˚C on PZT buffer layers with good electrical properties and offers the possibility to be extended to polymeric and CMOS substrates.

Chapter 5 Microstructure Evolution of *In Situ* Pulsed-Laser Crystallized $Pb(Zr_{0.52}Ti_{0.48})O_3$ Thin Films

5.1 Introduction

[2]It was shown in the previous chapters that a combination of growth and real time laser induced crystallization approach lowers the substrate temperatures required for fabrication of piezoelectric oxide thin films while eliminating film thickness constraints due to limited thermal penetration depth of the absorbed laser pulse. Selected orientations can also be achieved by controlling nucleation from the substrate. It was further demonstrated that oriented perovskite $PbZr_{0.52}Ti_{0.48}O_3$ (PZT(52/48)) thin films with a thickness of the order of a micron could be grown using this technique. The film microstructure was characterized by fine columnar grains caused by a large nucleation density.

The functional properties of PZT thin films are heavily dependent on the crystallization as well as the microstructure. Hence it becomes imperative to understand the effect of growth parameters and pulsed laser heating on the evolution of the microstructure in PZT thin films produced by this technique. This chapter describes the microstructures of the thin films grown by *in situ* laser annealing along with the mechanisms responsible for the microstructure development.

---

[2] Parts of the results in this chapter were previously reported in:
A. Rajashekhar et al., *J. Am. Cer. Soc.* Vol 99, no. 1 pp 43-50 (2016)

5.2 Experimental Procedure

As in Chapter 4, a pulsed laser deposition (PLD) system with *in situ* laser annealing was used in this part of the work. A single 248 nm KrF excimer laser with a 20 ns pulse-width and 20 Hz repetition rate was used for PLD as well as the annealing, where a 50-50 beam splitter was utilized to carry out the two functions simultaneously. Figure 5-1 depicts the geometry of the substrate holder with respect to the ablation plume and the annealing beam. The center of the annealing spot is offset from the substrate rotation axis, and as a result, the growing film spent only a fraction of time per rotation in the deposition plume or the annealing beam.

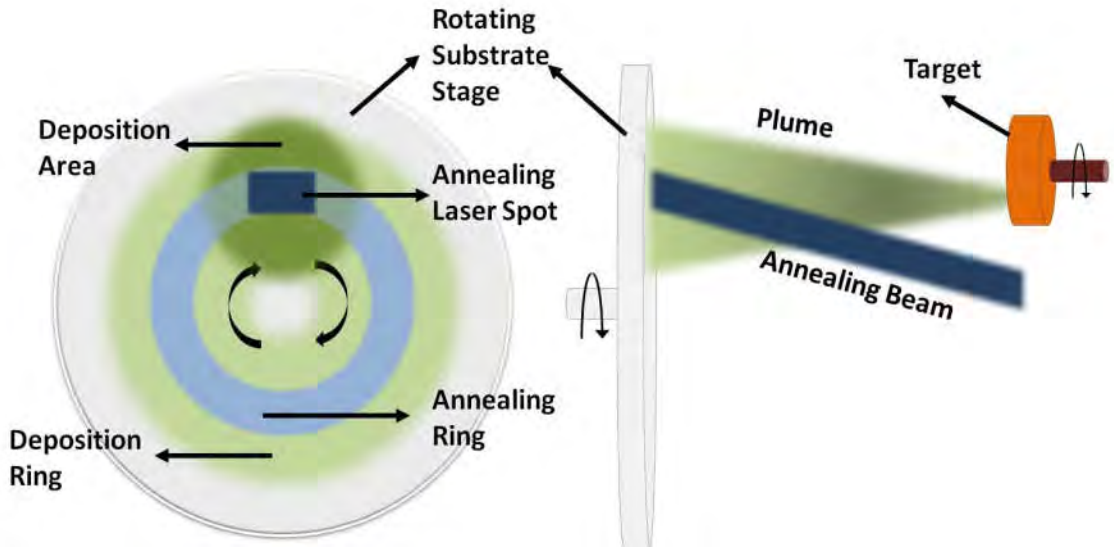

Figure 5-1: Schematic of the laser annealing process during growth by PLD. The annealing beam was ~1.6 cm by ~0.8 cm while the center of the annealing beam was located ~2cm above the center of the holder. The extent of the deposition vapor on the substrate holder was ~2.5 cm. The substrate was rotated at 10 rpm.

Growth with a seed-layer was adopted in this work. A low temperature seed-layer (by *ex situ* laser annealing) was demonstrated in Chapter 4, where it was seen that growth on laser-crystallized and rapid thermally annealed (RTA'd) seed-layers yielded comparable highly columnar growth, and well crystallized films. As the aim of this chapter was to study the

growth mechanism associated with *in situ* laser annealing, the crystallization temperature of the seed-layer was not critical for the current experiments. Hence, a sol-gel [91] $PbZr_{0.30}Ti_{0.70}O_3$ (PZT(30/70)) seed-layer on (111)Pt/Ti/SiO_2/Si wafers (from Nova Inc.), RTA furnace crystallized at 700˚C for 1 min was used as the substrate. A PZT(52/48) PLD target with 20%-excess PbO (unless otherwise mentioned) prepared by a conventional solid-state mixed oxide route was utilized for ablation in the laser fluence range of 1 – 2 J/cm^2. The target-substrate distance studied was in the range of 5 – 7.2 cm while the substrate temperature used was maintained around ~350 – 380 ˚C to provide some additional thermal energy. The laser annealing energy densities lay between 50 and 60 mJ/cm^2. A 90% oxygen/10% ozone ambient was utilized at chamber pressures between 50 – 120 mTorr. The substrate was rotated at 10 rpm to increase the annealing area. After the final ablation pulse was completed, the annealing pulses were continued for an additional 60 seconds, so as to crystallize any surface layers deposited by the last ablation pulses.

For the thermal simulations, finite element modeling of laser heating was performed using the 1-D heat equation as described in Chapter 2. Three (static) thicknesses of the PZT film were considered: 100 nm, 300 nm and 600 nm, while the substrate structure comprised of 100 nm Pt/10 nm Ti/1 μm SiO_2/500 μm Si.

5.3 Results and Discussion

5.3.1 Crystallization

TEM analysis (Courtesy: Huairuo Zhang, University of Sheffield, UK) was carried out on an *in situ* laser annealed PZT(52/48) film (~350 nm thick) deposited at an ablation fluence of ~1.8 J/cm^2, with a target-substrate distance of 7.2 cm, at a pO_2 of 70 mTorr, an annealing

energy density ~55 mJ/cm^2 and on a sol-gel crystallized PZT(30/70) seed-layer (~70 nm thick). A multi-beam dark-field TEM image taken with several Bragg diffraction beams shows that the film is columnar (Figure 5-2(a)). Figure 5-2(b) (inset) shows a [111] zone-axis electron diffraction pattern (EDP) taken from a single column. Further EDPs revealed that each column was a single grain. The mottled contrast in the single grain in the diffraction contrast image of Figure 5-2(a) may arise because local defects and compositional variations reduce the size of ferroelectric domains and disrupt the habit planes of their walls. Note that the seed-layer (Zr:Ti ratio 30:70) contains planar domain walls typical of a tetragonal ferroelectric. In this instance, the larger spontaneous strain with respect to the bulk of the film (Zr:Ti ratio 52:48) forces longer range polar coupling despite a similar density of local defects. High resolution TEM (Figure 5-3) revealed local epitaxy across the seed-layer – film interface. However, layers of pores were found to be segregated at the grain boundaries, as can be seen in the STEM bright-field image (Figure 5-2(b)).

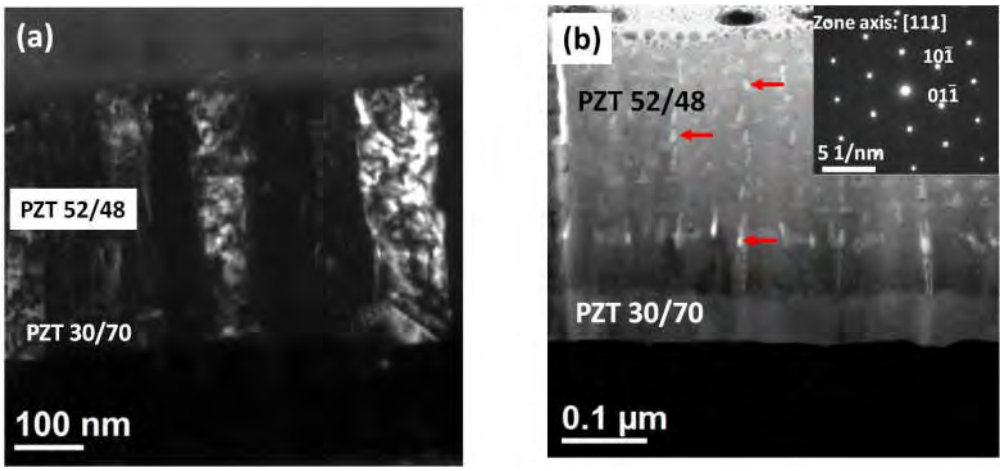

Figure 5-2: (a) Multi-beam dark-field TEM image of *in situ* annealed PZT film (b) STEM bright-field image showing pore segregation at the grain boundaries (some marked with red arrows). Inset in (b) shows the selected area electron diffraction pattern of a column showing good crystallinity of the grain.

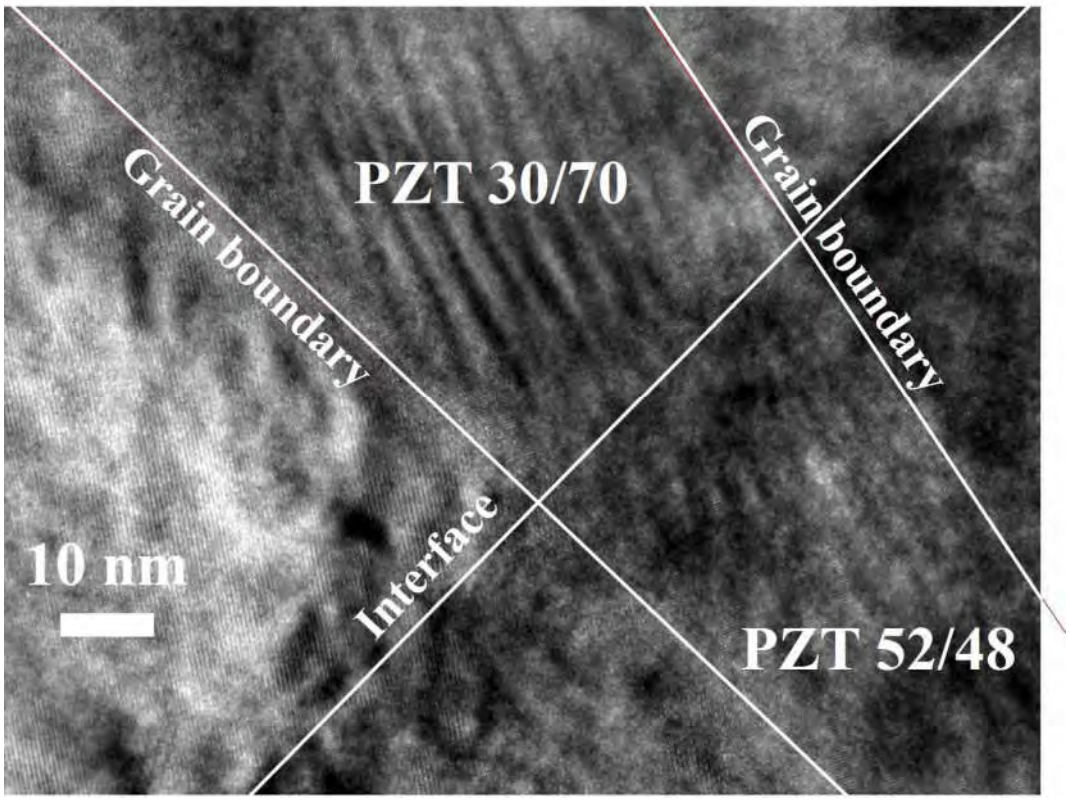

Figure 5-3: HRTEM across the seed layer/*in situ* laser annealed film interface

5.3.2 Microstructure Development

It is important to consider what determines the film densification. Atomistically, surface and bulk diffusion are expected to play a role in determining the microstructure in any thin film growth process. Here, the diffusivities are primarily a function of the energy of the arriving vapor species as well as the pulsed-laser heating. To assess these independently, the energy of the incident atoms was varied via the gas pressure in the chamber. Figure 5-4 and Figure 5-5 show the microstructures of films deposited at chamber pressures between 50 mTorr and 120 mTorr. For these experiments, the ablation-fluence (~1.7 J/cm^2), the annealing energy-density (~55 mJ/cm^2), and the target-substrate distance (6 cm) were held constant. A ~50nm thick PZT(30/70) seed layer was used. Higher pressures imply more

scattering of the plume species with the ambient gas molecules, effectively reducing the energy of the atoms/ions arriving at the substrate [94]. It was found that this produces a less dense, fine grained structure, with pores visible along the grain boundaries (120 mTorr). Reducing the O_2 pressure to 70 mTorr acts to densify the film, but the fine-grained structure is maintained, with some remanent porosity. At chamber pressures of 50 mTorr, coarsening of the fine grains (to ~200 nm diameter), with concomitant densification is observed. The improvement in crystallinity (inferred from the cross-sectional SEM and sharp peaks in the XRD pattern) may also be due to the higher energy of the depositing species associated with reduced collisions between the plume species and the chamber gas at low pO_2. Micro-cracking, which points to growth-induced residual stresses, was also observed.

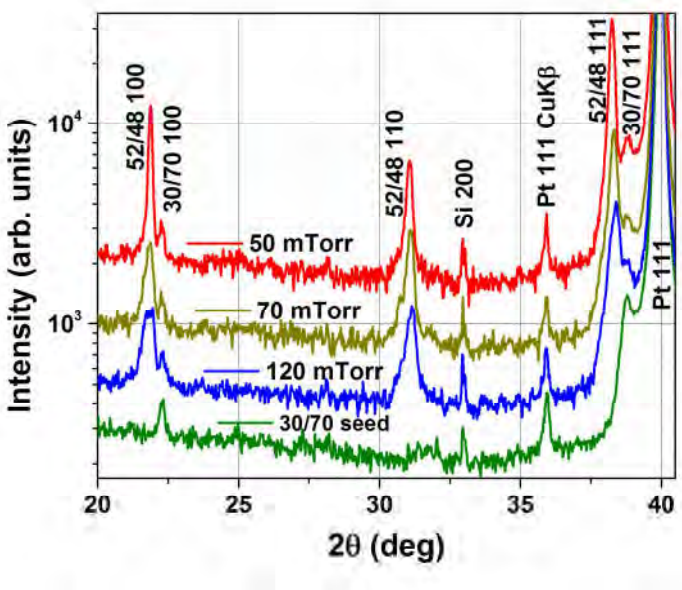

Figure 5-4: XRD of films deposited at various pO_2 chamber pressures. The XRD of the PZT(30/70) seed-layer is included for comparison. The ablation-fluence was ~1.7 J/cm^2, laser annealing energy-density was ~55 mJ/cm^2 and the target-substrate distance was 6 cm.

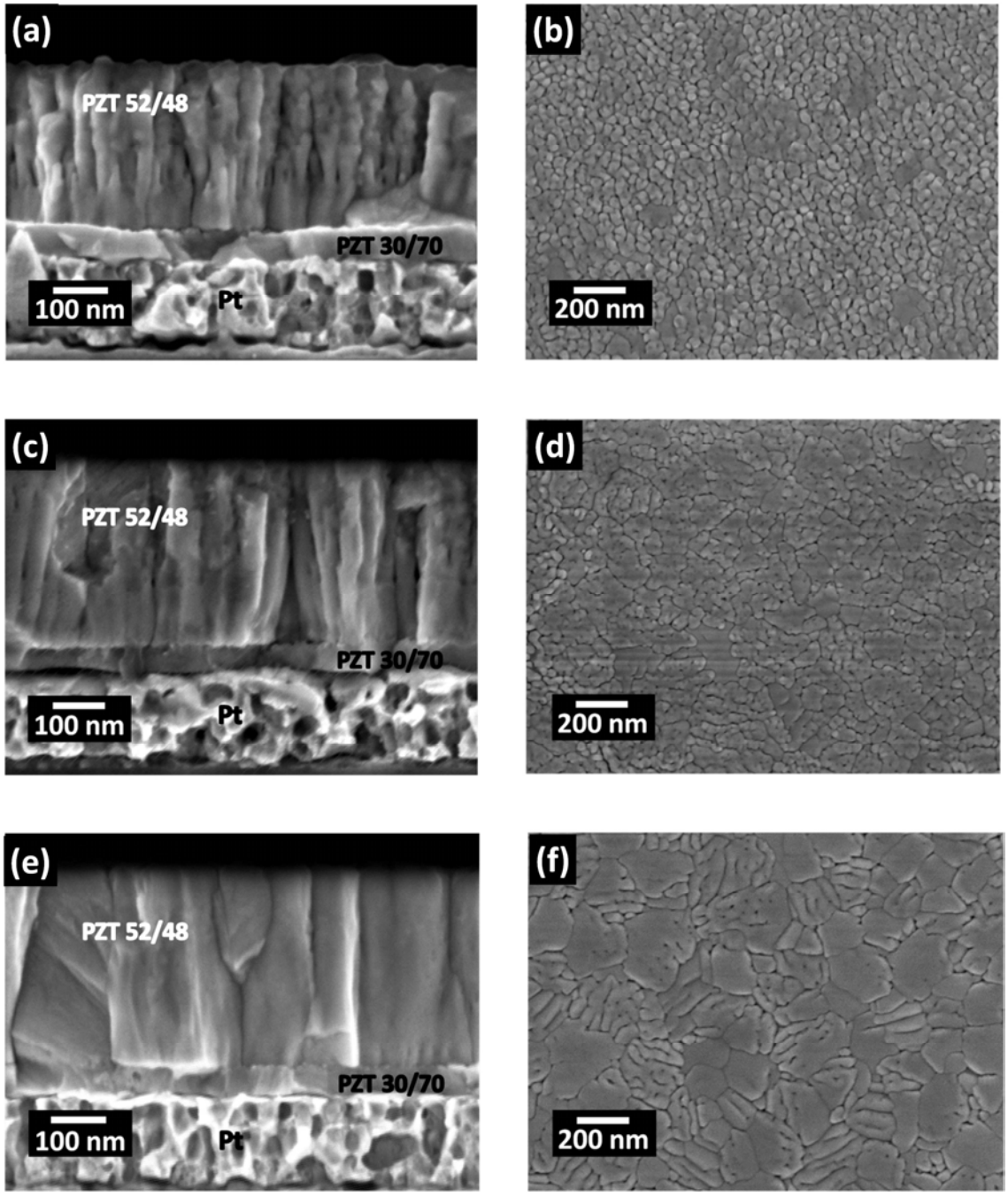

Figure 5-5: Cross-sectional and plan-view FESEM of PZT films deposited at different pO_2; (a) & (b) 120 mTorr, (c) and (d) 70 mTorr, (e) and (f) 50 mTorr

Increased bombardment contributes to densification by forward scattering of the surface atoms; films deposited under high bombardment conditions also show lower surface roughnesses [95]. However, excessive bombardment may induce Pb re-sputtering. Reducing the target-substrate distance to 5 cm, while maintaining the pressure at 50 mTorr, achieved similar densification, but with increased Pb loss from re-sputtering giving rise to some lead-deficient pyrochlore/fluorite phase (Microstructure shown in Figure 5-6, while XRD is shown in Figure 5-7).

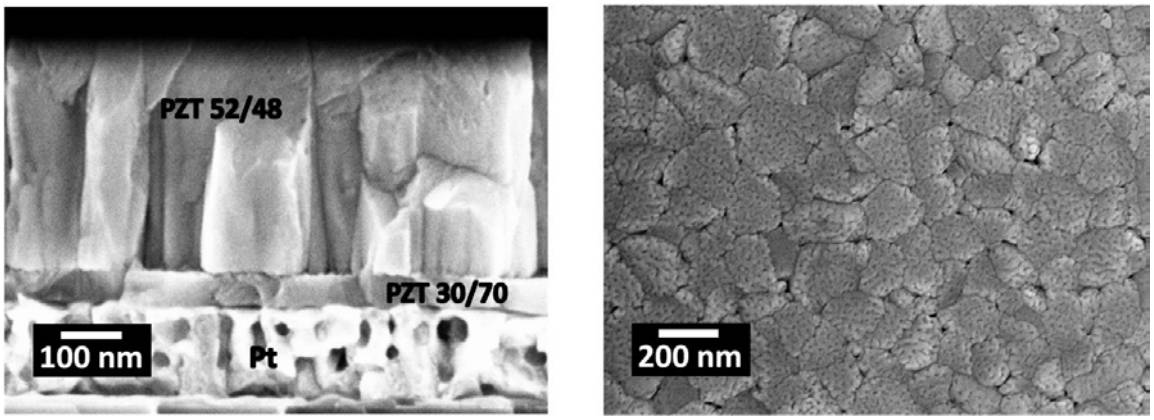

Figure 5-6 Microstructure of *in situ* laser annealed PZT 52/48 deposited using an ablation laser fluence ~1.7 J/cm^2, pO_2: 50 mTorr, target-substrate distance: 5 cm. The surface SEM suggests large grain sizes (~200 nm), but also shows unusual topography of the grains, that could be due to Pb-resputtering.

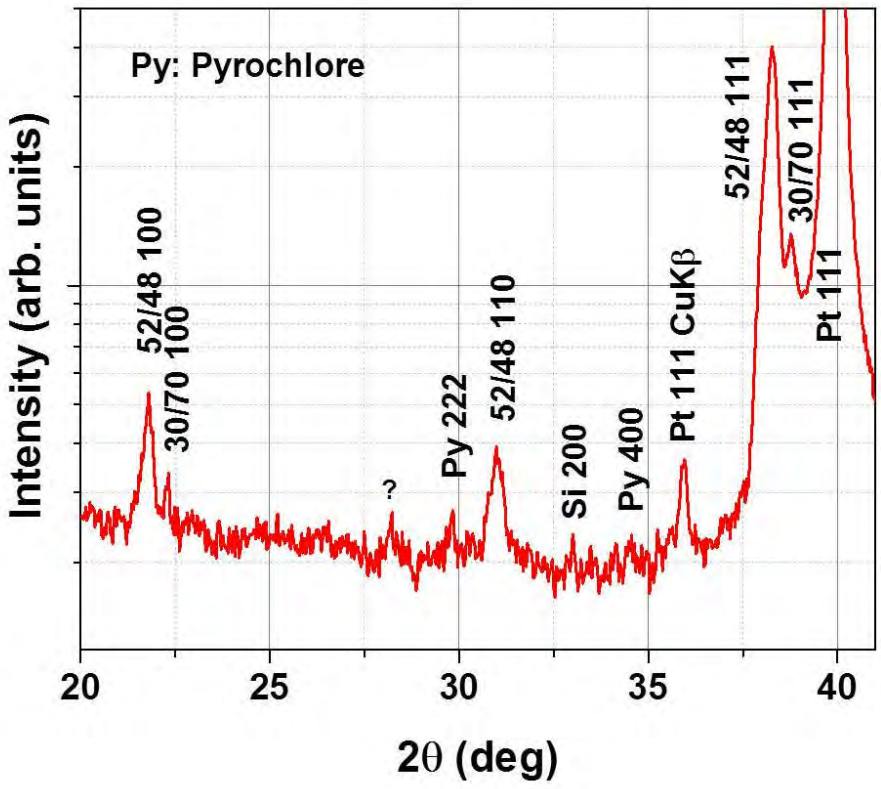

Figure 5-7: X-ray diffractogram for an *in situ* laser annealed PZT 52/48 film deposited using an ablation laser fluence ~1.7 J/cm^2, pO_2: 50 mTorr, target-substrate distance: 5 cm. Py = pyrochlore

To compare the properties to conventional films, the refractive indices of the film deposited at 50 mTorr and 6 cm target-substrate distance were extracted from spectroscopic ellipsometry in the wavelength range of 500 nm to 1690 nm. A model consisting of roughness/PZT(52/48)/PZT(30/70)/Pt was used for this purpose (Figure 5-8(d)). Since PZT is transparent in this spectral range, Sellmeier models [96] were utilized to describe the optical constants for both PZT(52/48) as well as PZT(30/70). The model fits for the spectroscopic ellipsometry parameters of Psi (ψ) and Delta (Δ) (with a weighted root Mean Squared Error (MSE) [66] of 14.5) are shown in Figure 5-8 (a) and (b). The refractive index

obtained was compared with those for the same composition film (PZT(52/48)) reported in Ref.[97] (Figure 5-8(c)). The difference in the refractive index was seen to arise from a porosity level of ~2.7 volume% as obtained from a Bruggeman effective medium model.

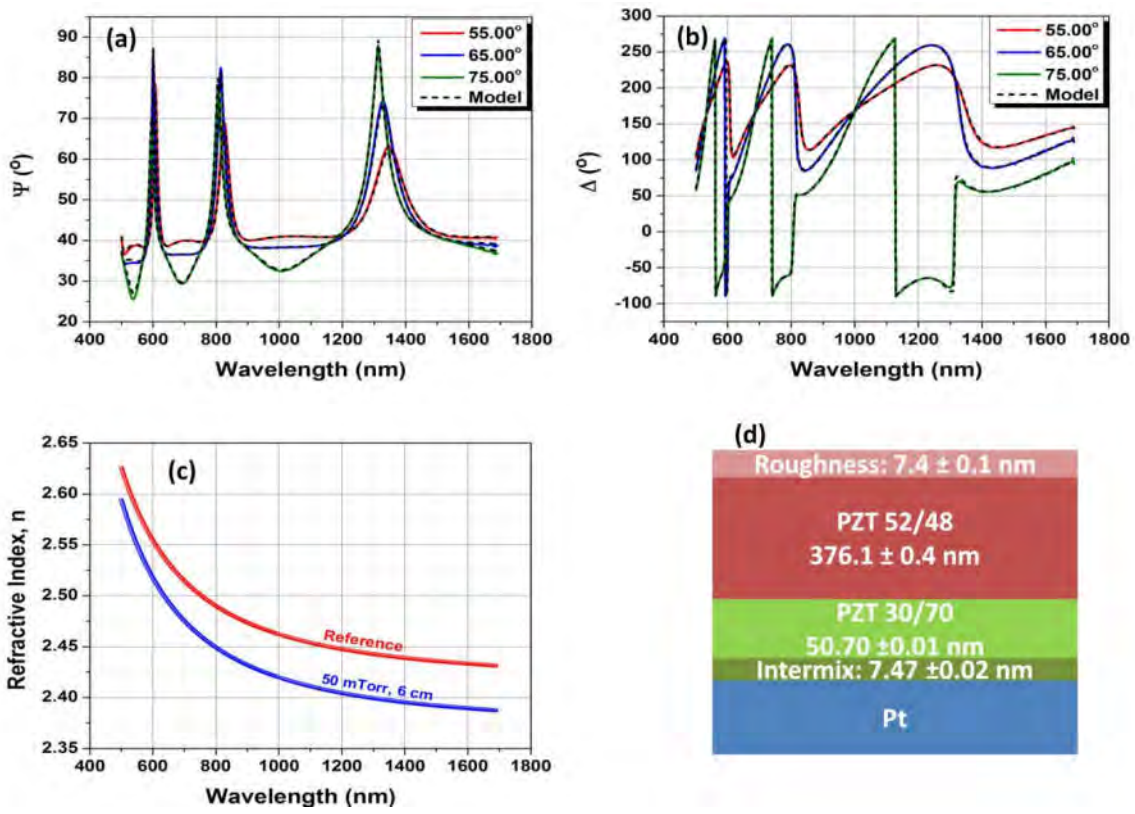

Figure 5-8 ((a) and (b)) Model fits to spectroscopic ellipsometry data (ψ and Δ), (c) Dispersion of refractive index n extracted from the fits (comparison with data from Ref.[23] in the manuscript, extrapolated to higher wavelengths), (d) Layered structure used in the modeling (values indicated in the individual layers correspond to the best fit thicknesses)

STEM-EDS (courtesy: Huairuo Zhang, University of Sheffield, UK) line scan analysis was carried out on the sample deposited at a pO_2 of 50 mTorr and 6 cm target-substrate distance to study compositional homogeneity, as illustrated in Figure 5-9(a). A vertical EDS scan demonstrates that the film is compositionally uniform through most of the thickness

(Figure 5-9(b)). However, the Pb concentration near the film – seed-layer interface is enhanced relative to the rest of the film; the reason for this is currently unknown. No significant compositional heterogeneity was observed across the grain boundary (Figure 5-9(c)). The HAADF image (Figure 5-9(d)) corroborates the large grain size witnessed in the cross-sectional FE-SEM, and also shows some trapped layered porosity within the grains as expected from the spectroscopic ellipsometry.

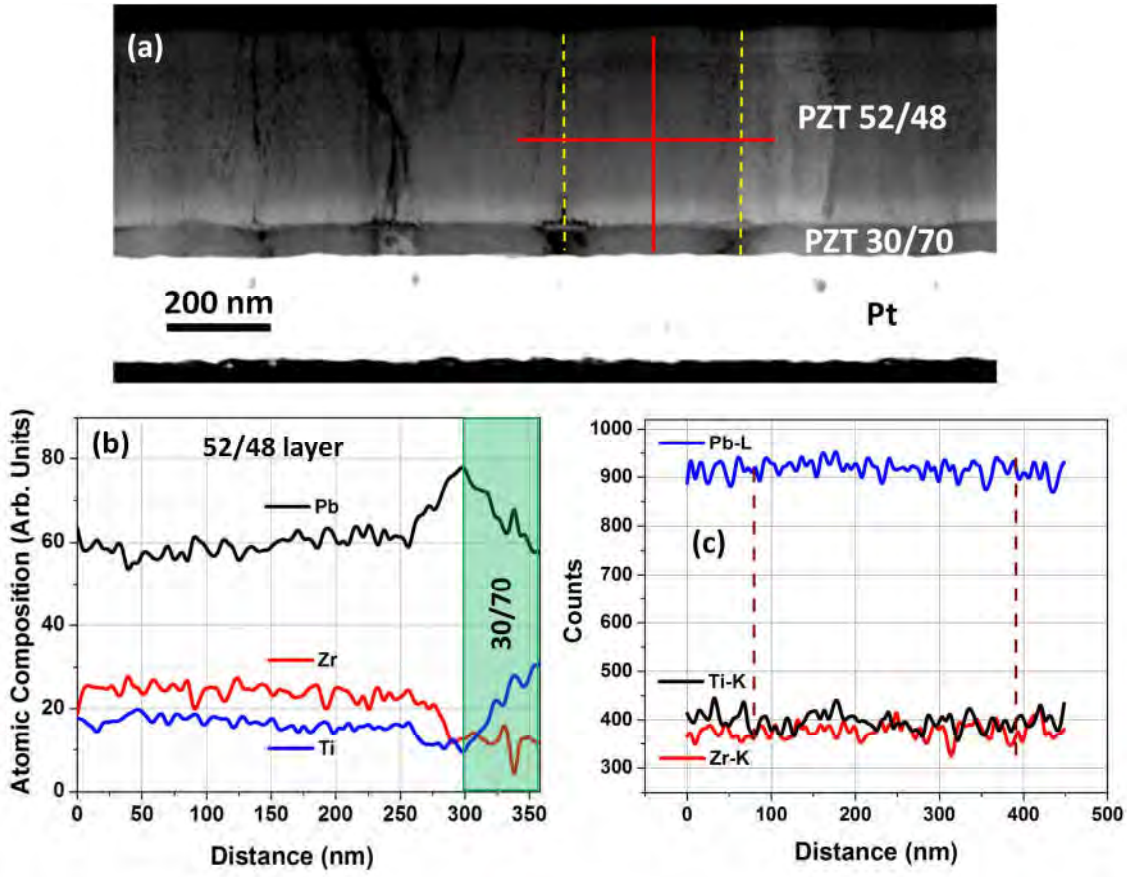

Figure 5-9: (a) an HAADF image showing large grain sizes and some layered porosity. The vertical and horizontal lines along which EDS scans were carried out are marked (red lines); The dashed vertical lines denote the positions of the grain boundaries, (b) vertical EDS and (c) horizontal EDS scan intensities of Pb-L, Zr-K and Ti-K peaks

Laser annealing duration as a fraction of the deposition time was also varied to understand the role of laser-induced diffusion, while maintaining other factors constant at an ablation fluence ~1.7 J/cm^2, annealing energy density: ~55 mJ/cm^2, target-substrate distance: 6 cm, pO_2: 85 mTorr, and deposition duration: 1.5 hours. To achieve this, an electronic shutter (*Smart*Shutter® from Sutter Instrument Company, controlled using a Lambda SC control unit) was used on the annealing arm of the laser pathway. The 'fractional anneal time' (f_t^{Anneal}) was defined as the ratio of the annealing duration to the total ablation (deposition) duration. With the shutter for annealing continuously open, the total durations for annealing and deposition are the same, hence giving an f_t^{Anneal}=1. The ratio of the pulses was maintained continuously in real time to minimize any spatial variation as the substrate was rotated. Consider, for example, the case of f_t^{Anneal} of 0.27 (= 3/11). Here, a single shutter open/close cycle consisted of 11 consecutive annealing (and ablation) laser pulses, with a laser repetition rate of 20 Hz. Of these only a set of 3 annealing pulses were let in, while the subsequent 8 pulses on the annealing arm were blocked). For all the cases investigated (listed in Table 5-1), the annealing shutter open duration (packets of 3 annealing pulses at a time) was kept constant, while the shutter close time was varied (the number of annealing pulses let in plus the number of blocked annealing pulses give the total number of deposition pulses per cycle). This was done while maintaining a constant total deposition time. The approximate numbers of cumulative annealing pulses seen by the sample were calculated for each f_t^{Anneal} using the substrate rotation geometry and are listed in Table 5-1. The approximate growth rate was also estimated as ~0.3 Å/pulse for all cases.

Table 5-1: List of fractional anneal times investigated

Number of consecutive annealing pulses let in per shutter cycle	Number of blocked pulses on the annealing arm per shutter cycle	Number of consecutive deposition pulses per shutter cycle	Fractional Anneal Time (f_t^{Anneal})	Approximate number of cumulative annealing pulses for 590 nm PZT
3	0	3	3/3 (= 1)	~13074
3	4	7	3/7 (= 0.43)	~5622
3	8	11	3/11 (= 0.27)	~3530
3	15	18	3/18 (≈ 0.17)	~2223
3	30	33	3/33 (≈ 0.09)	~1177

The X-ray diffraction patterns of the films (~590 nm thick PZT(52/48) on ~50 nm PZT(30/70) sol-gel seed) along with that of a film that saw no laser annealing and the PZT(30/70) seed-layer are shown in Figure 5-10. The film which was not laser-annealed primarily showed the pyrochlore phase along with seed-layer and substrate peaks. The films with different fractional anneals are all crystalline but with varying degrees of preferred orientation. Figure 5-11(a), (b) and (c) show the 111_{pc}, 110_{pc} and 100_{pc} (pc: pseudocubic perovskite) PZT peaks for the films. These peaks were fit to Lorentzian profiles using Mathematica® and integrated peak-intensities, peak-positions, and full-width-at-half-maxima (FWHM) were extracted. As shown in Figure 5-11(d), on increasing the f_t^{Anneal}, an increase in the integrated-intensity of the 111_{pc} PZT(52/48) peak is seen along with a corresponding reduction in the integrated-intensities of the 110_{pc} and 100_{pc} peaks. That is, smaller laser f_t^{Anneal} promote a more random orientation. One possibility is that the random orientation with low f_t^{Anneal} is characteristic of grains nucleating from a pyrochlore matrix [98]. With higher f_t^{Anneal}, 111_{pc} orientation is preferred, presumably

as a result of preferential nucleation from the substrate. Alternatively, it is possible that in the initial stages of the film growth, grains with 111_{pc} orientation outgrow the ones oriented along the 100_{pc} and 110_{pc} directions on increasing f_t^{Anneal}, hence yielding the current trend. A concomitant shift of the 111_{pc} peak to higher 2θ angles is also seen Figure 5-11(e)) with increasing f_t^{Anneal}. If these shifts are entirely due to the development of an in-plane residual tensile strain, a consequent out-of-plane compressive strain of about -0.5% can be inferred on going from an f_t^{Anneal}=0.09 to an f_t^{Anneal}=1. It should be noted that neither the seed-layer 111 peak nor the 111 Pt peak are affected, indicating that the peak shift is induced by the *in situ* laser annealing growth process of PZT(52/48). However, the origin of a corresponding increase in the FWHM of the 111_{pc} peaks with increasing f_t^{Anneal} is currently not understood. Nested polarization-electric field hysteresis loops and leakage currents at 3 times the coercive field are shown in Figure 5-12 and the corresponding remanent polarization (P_r) and coercive field (E_c) values are also listed in Table 5-2.

The microstructural changes accompanying the increased f_t^{Anneal} are shown in Figure 5-13. It is important to note that all the films show fine-grained columnar microstructures which are maintained with increased f_t^{Anneal}. Lateral growth or coarsening of the grains is not observed. Micro-voids become apparent on the surface when the film is subjected to an f_t^{Anneal} of 0.3 (Figure 5-13(f)), while micro-cracks are observed in the cases of 0.5 and 1 (Figure 5-13(h) & (j)). The microcracking is likely to be the result of the in-plane tensile stresses.

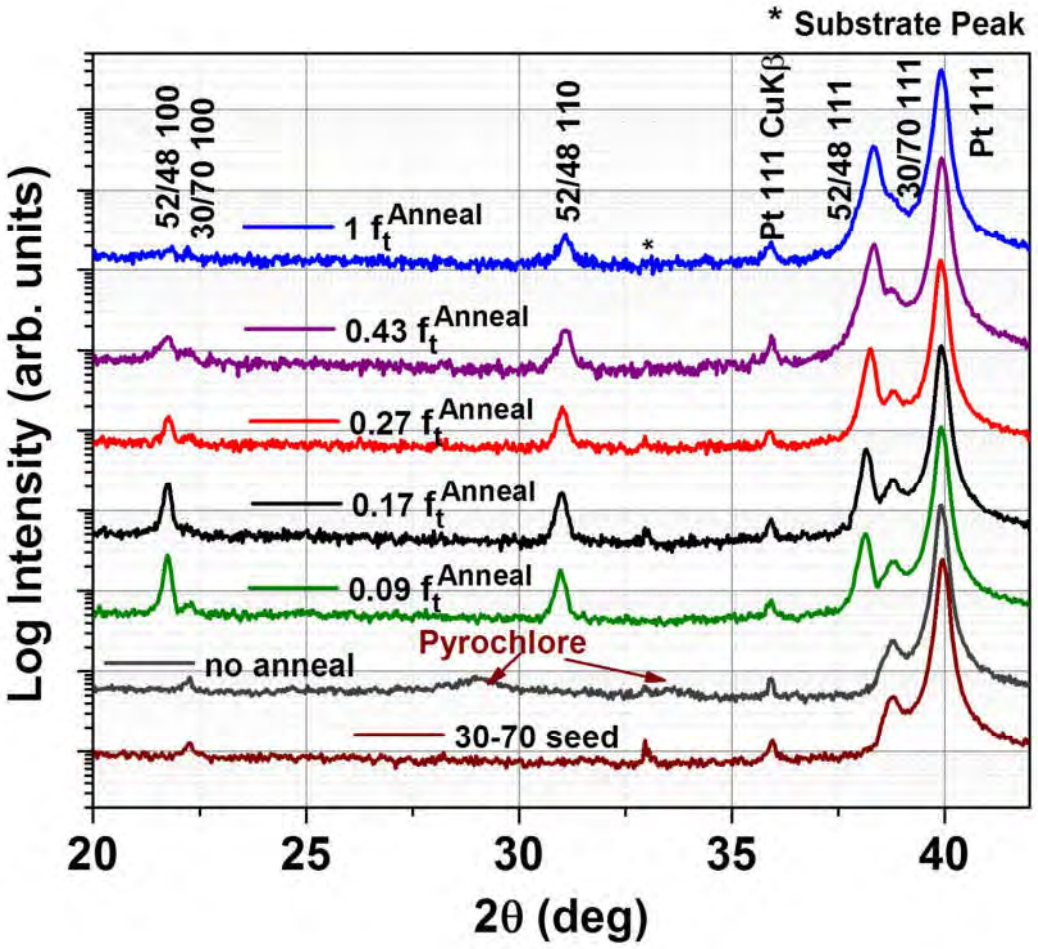

Figure 5-10: Evolution of crystallization with different fractional laser anneal times. The peak position marked with an asterisk (*) is from the substrate.

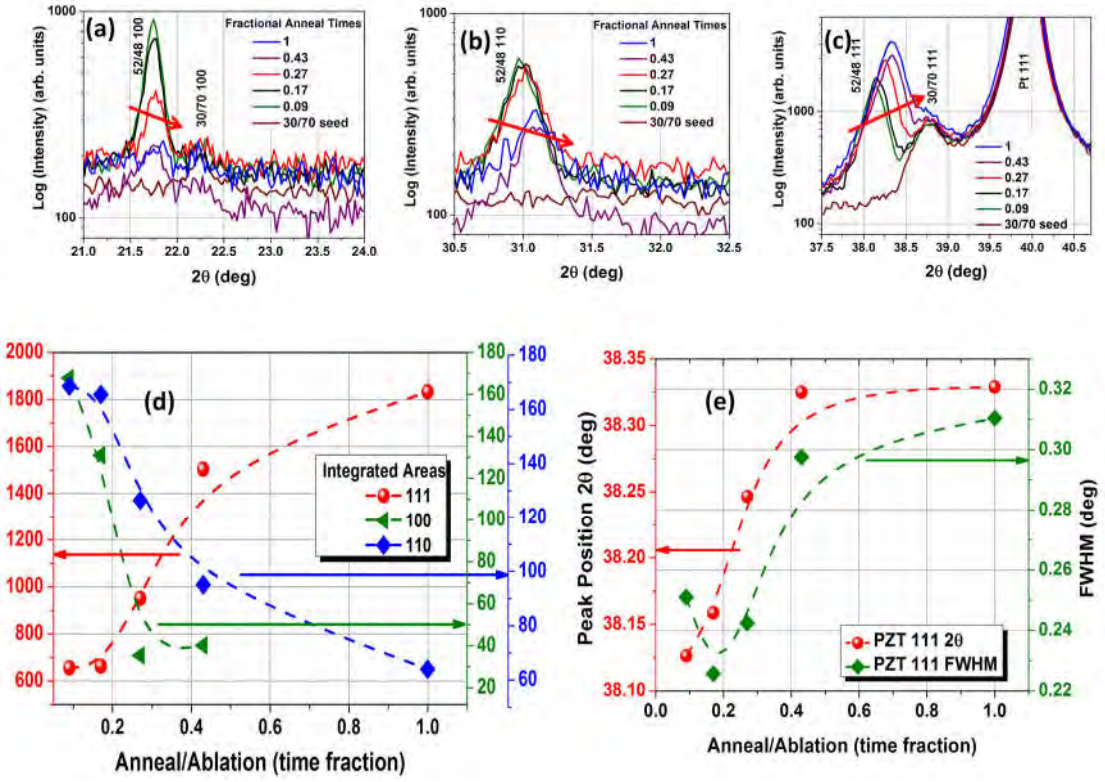

Figure 5-11: (a) 100_{pc}, (b) 110_{pc} and (c) 111_{pc} peaks with varying fractional laser anneals, (d) the integrated intensities and (e) 111 peak position and FWHM. The integrated intensities were calculated using the corresponding peak fits in Mathematica®.

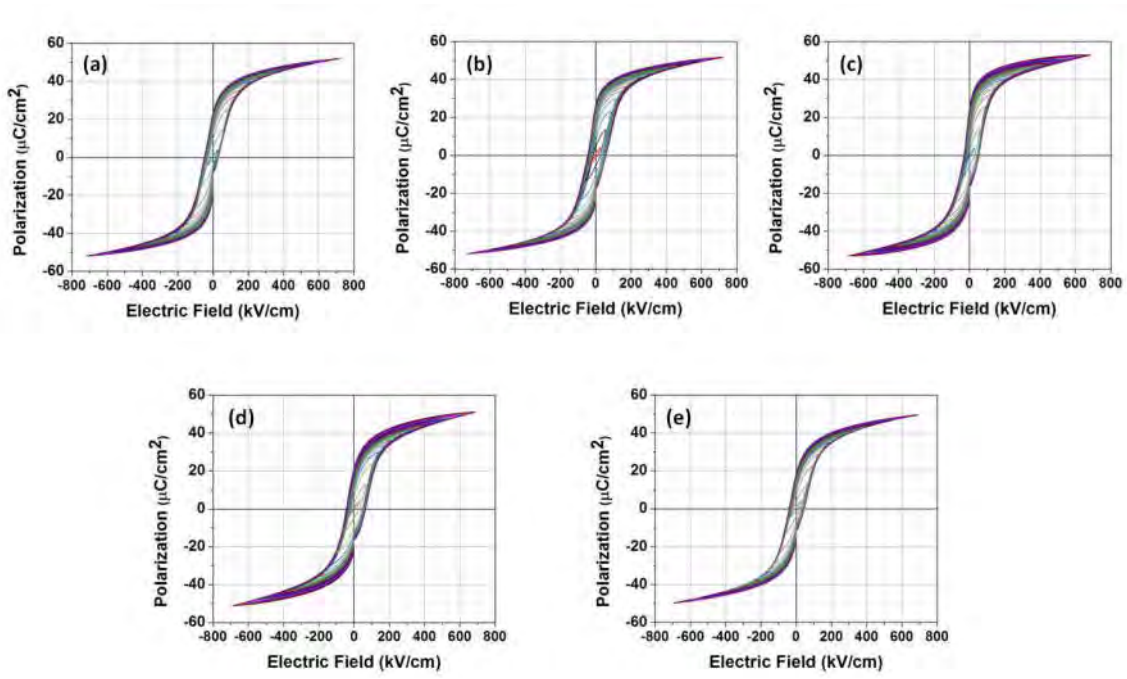

Figure 5-12: Nested polarization-electric field hysteresis loops for the various f_t^{Anneal} : (a) 0.09, (b) 0.17, (c) 0.27, (d) 0.43, (e) 1

Table 5-2: Summary of remanent polarization (P_r), coercive fields (E_c) and leakage currents for the various f_t^{Anneal}

f_t^{Anneal}	$(P_r^+ + P_r^-)/2$ ($\mu C/cm^2$)	$(E_c^+ + E_c^-)/2$ (kV/cm)	Leakage Current (at $3*E_c$) (A/cm^2)
1	18	43	1.4×10^{-8}
0.43	22.5	56	1.6×10^{-6}
0.27	25	43	2.8×10^{-8}
0.17	26.3	52	8.4×10^{-8}
0.09	22.4	40	1.5×10^{-8}

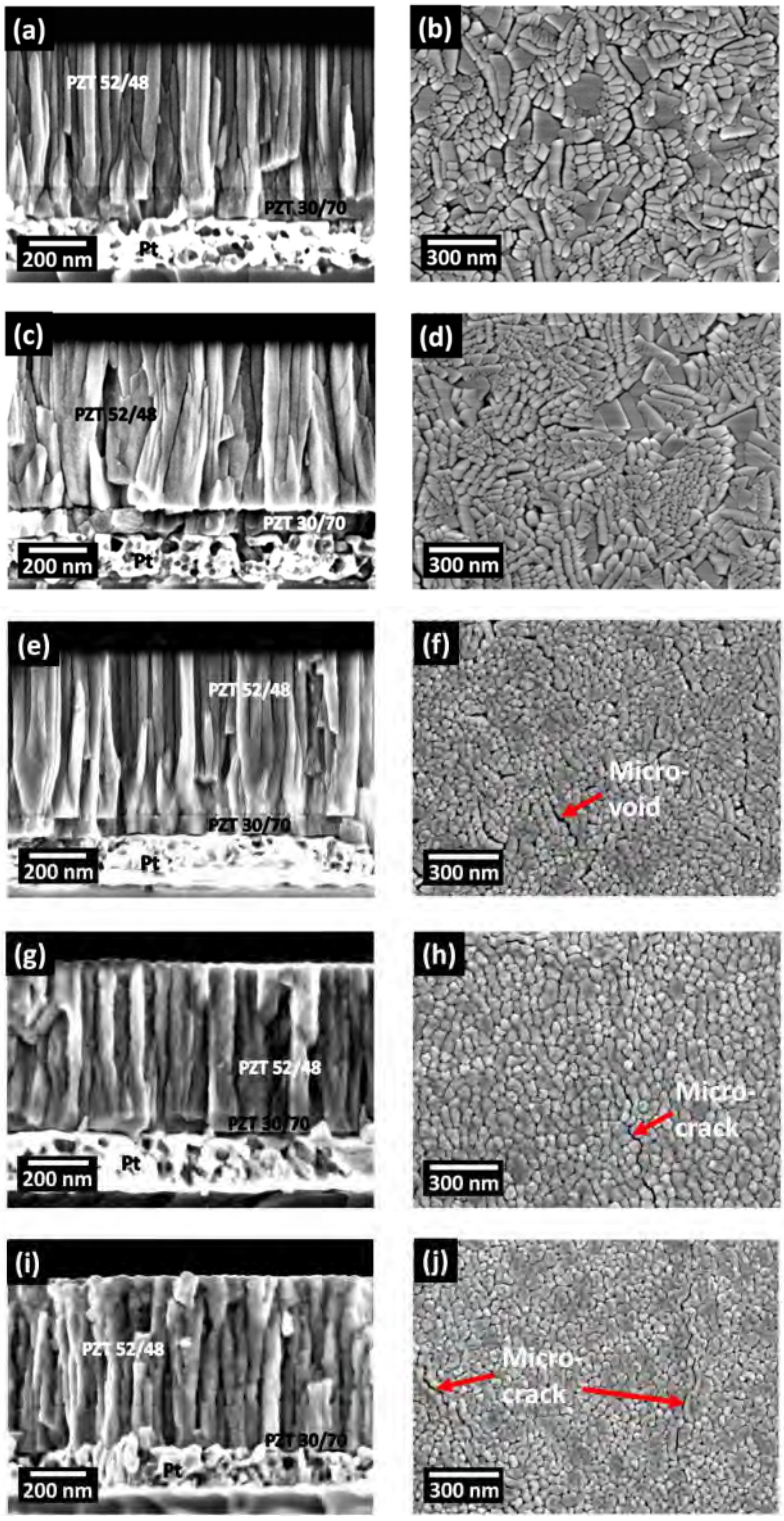

Figure 5-13: Microstructural changes as a function of fractional annealing time: 0.09 ((a) & (b)), 0.17 ((c) & (d)), 0.27 ((e) & (f)), 0.43 ((g) & (h)), 1 ((i) & (j)) (Micro-voids and micro-cracks have been labeled)

It is clear that a cumulative number of laser pulses of less than ~1200 (f_t^{Anneal}= ~0.09) can crystallize a ~590 nm thick PZT(52/48) on a PZT(30/70) seed layer. In comparison, in Ref. [51], 320-350 nm thick PZT(52/48) films were crystallized on a $PbTiO_3$ seed layer at 375˚C substrate temperature using about 4800-6000 pulses (using an energy density of 40-45 mJ/cm^2). Here, for an equivalent thickness, only about 650-712 pulses would have been needed at f_t^{Anneal}= ~0.09. In this case, every 33 deposition pulses (correspond to ~10 Å with respect to the growth rate of ~0.3 Å/pulse) get 3 annealing pulses (which yields ~3.3 Å per annealing pulse). Simulations of the temperature profiles due to photothermal heating by a single laser-pulse (with fluence = 55 mJ/cm^2 and pulsewidth = 20 ns, substrate temperature = 350˚C) at various depths in a 300 nm thick PZT (e.g.,) on Pt/Ti/SiO_2/Si substrate (Figure 5-14), show that the surface layers experience extremely high thermal excursions (T_{max} of ~1400˚C). Temperatures exceeding 600˚C are maintained for about 161 ns per pulse at the surface and are realized to a depth of ~250 nm inside the PZT. This suggests that each annealing pulse can potentially influence the crystallization to a comparatively large depth.

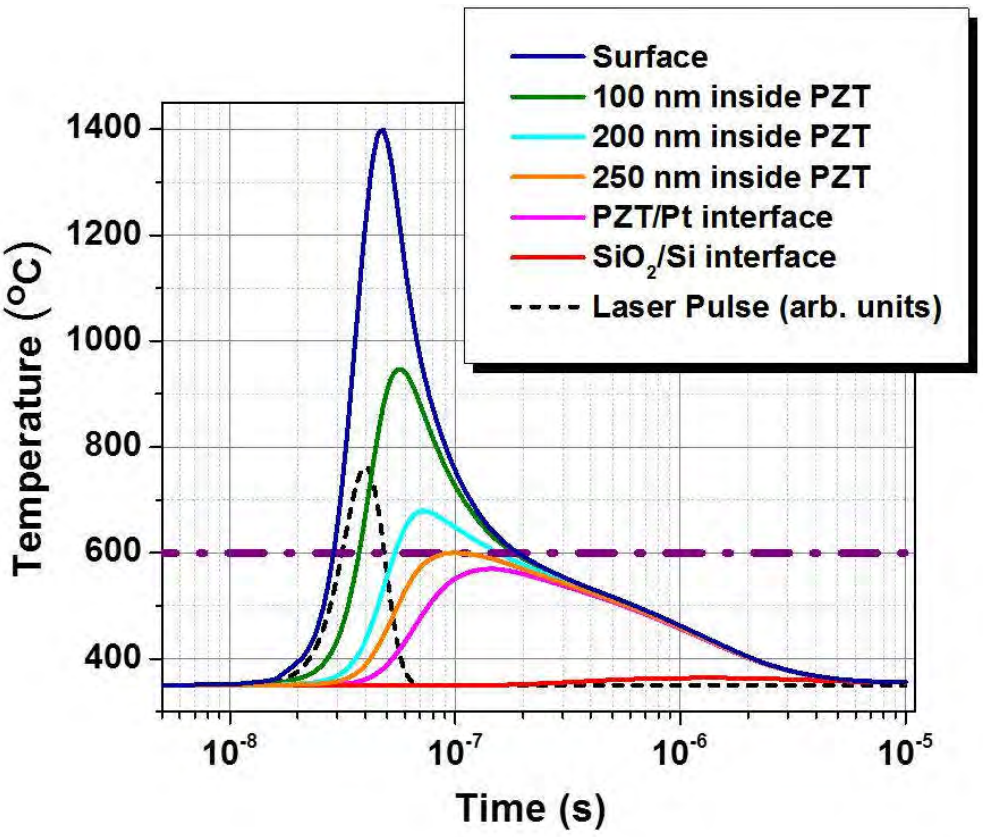

Figure 5-14: Temperature evolution at different depths inside 300 nm PZT on Pt/Ti/SiO_2/Si substrate. The laser pulse profile is also shown.

The thermal profiles are also compared to that of 100 nm and 600 nm thick PZT (Figure 5-15). It can be seen that although surface temperatures achieved for a 600 nm film are comparable to that of the 300 nm film (~1410˚C), temperatures over 600˚C are achieved only to a depth of ~300 nm in this case. Thus, a film of this thickness cannot be *ex situ* laser crystallized through the entire thickness with the given conditions. Instead, a sequential growth and crystallization route is necessary. For the 100 nm film, however, the surface temperatures achieved are lower (~1263˚C), although the entire PZT film thickness experiences maximum temperatures higher than 600˚C. It should be noted that in all of these cases, the SiO_2/Si interface experiences low thermal budgets (T_{max} ~370˚C). The lower surface temperatures in case of the thinner film is most likely due to the fact that heat

is rapidly removed by the underlying substrate at low thicknesses of the absorbing material [99]. In addition, at thicknesses lower than the optical absorption depth of the growing film (amorphous PZT has an optical absorption depth of about 33 nm [41]), reflection from the underlying metallic layer (in this case, Pt) might play a role as well. Effectively, the surface temperatures would be a function of the thickness of the material and would vary starting from the very initial atomic layers up to the large thicknesses during *in situ* laser annealing and growth. Hence, it should be kept in mind that for an efficient application of the *in situ* laser annealing process, the laser parameters (energy density, number of pulses) might have to be tuned with respect to the thickness of the film at every stage. Furthermore, change of reflectivity of the samples as a function of roughness of the thin films should also be taken into account as a factor affecting the absorption of the laser pulse. In general, higher the roughness, lower the reflectivity and higher the optical absorption in the material.

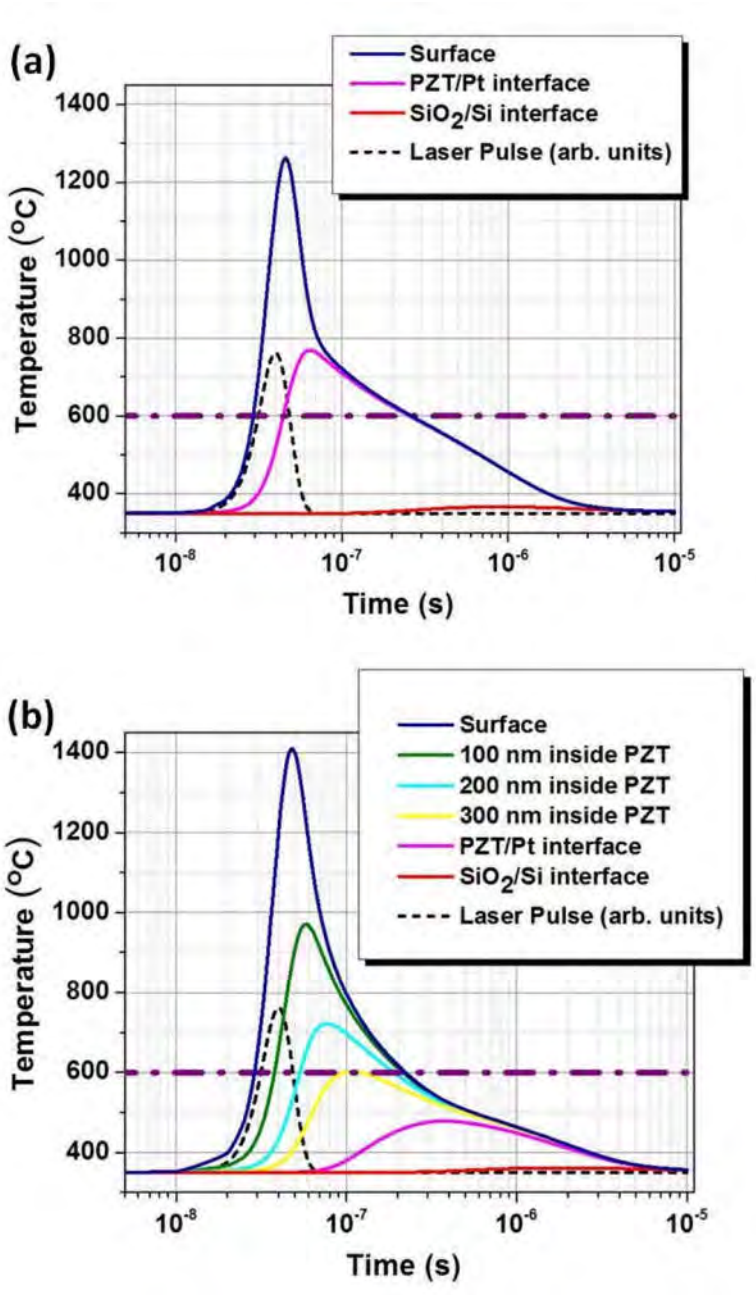

Figure 5-15: Temperature simulations for PZT with different thicknesses on Pt/Ti/SiO_2/Si substrates, (a) 100 nm thick, (b) 600 nm thick. The laser pulse profiles are also shown.

The structure zone model (SZM) was developed to describe the film microstructures characteristic of physical vapor deposition processes [100],[101]. The observed microstructure is a function of the homologous temperature, T_h (= T_s/T_m; where T_s: substrate temperature, T_m: melting point) and varies from Zone I (at low T_h; characterized by a low density structure and fine fiber texture due to very low adatom mobility) through Zone T (slightly higher T_h; characterized by a columnar structure, but immobile grain boundaries, with limited surface mobility sufficient for local epitaxy on top of a grain) to Zone II (high T_h regime where significant bulk diffusion operates giving rise to grain boundary migration and grain coarsening).

The microstructures of PZT films with varying f_t^{Anneal} indicate that pulsed laser heating primarily produces structures which lie in between Zone I and Zone T, which is surprising given the high surface temperatures seen as a result of pulsed laser irradiation. It is believed that a high density of nuclei is responsible for the observation of such fine grain features irrespective of the f_t^{Anneal} values. In this case, the activation barrier for nucleation of the perovskite phase is low due to a high thermodynamic driving force for crystallization (ΔG_v), which is the difference between the free energy of the crystalline solid and the metastable amorphous/pyrochlore deposited material at the low substrate temperature [31],[30] (Figure 5-16). This gives rise to a high nucleation rate [30], [31]. Furthermore, the larger this driving force is, the smaller the size of critical nuclei that should be required. In the case of laser ablation with simultaneous annealing at 20 Hz, the film sees an annealing laser pulse and a vapor pulse every 50 ms. Simulations of the laser-induced heat-pulse suggests a decay to the background (substrate) temperature on the order of a few

microseconds (Figure 5-14). Thus, the effective time at temperatures high enough for bulk diffusion is quite short. Furthermore, the lateral growth rates, determined by an activation energy that is independent of the driving force for crystallization [36], are low compared to the nucleation rates. Consequently, although the laser pulses provide the bursts of energy required for short-range diffusion such that the crystallization reaction can occur, long-range diffusion is kinetically limited. Moreover, the adatom mobility is low between consecutive ablation/annealing pulses (in contrast to conventional PLD where high substrate temperatures enable nuclei to undergo ripening in between pulses [92]). It is believed that these factors account for the observed Zone I/Zone T structures.

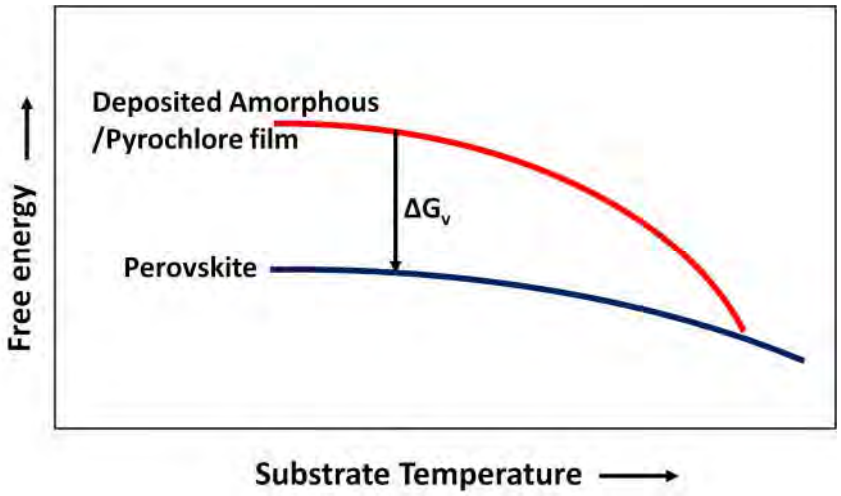

Figure 5-16: Schematic representing the variation of free energies of the deposited metastable amorphous/pyrochlore phase and the stable perovskite phase (adapted from Ref. [30], [31]**). The thermodynamic driving force for phase conversion (ΔG_v) for an arbitrary substrate temperature is indicated**

With respect to the growth stresses, it is reported in the literature on metal thin films that the coalescence of grains to form grain boundaries produces a residual tensile stress [102]. This tensile stress increases with decreasing grain size and is accentuated by low adatom

mobility conditions [102],[100]. Another model for the generation of tensile stress [103] is the constrained shrinkage that occurs during annealing of disordered material beneath the surface, while the film is being coated further with an incoming flux. The volume reduction associated with the amorphous/pyrochlore/perovskite transformation in PZT [104],[105] could potentially give rise to shrinkage-induced stresses. However, this mechanism for stress development would be more prominent at lower f_t^{Anneal} since, on average, a larger thickness of the film that needs to be crystallized is accumulated in between the annealing pulses. This in turn would mean larger tensile stresses at smaller f_t^{Anneal}, which is opposite to the observed trend. In addition, for PZT and other Pb-containing oxides, any unreacted excess PbO can, in principle, micro-segregate at the grain boundaries and subsequently evaporate on experiencing high temperatures during laser heat treatment. A combination of one or more of these factors could give rise to an intrinsic tensile stress and/or prevent complete coalescence of the grains, leaving pores.

5.4 Effect of Excess PbO in the Target on the Microstructure

In order to study the effect of excess PbO in the target on the resultant microstructure, depositions were carried out with targets with varying excess PbO concentration. Five target compositions were investigated: 20%, 15%, 10%, 5% and 0% excess PbO (molar %) and 600-700 nm thick films were grown using the various targets. The crystallization in terms of 111 PZT peak intensities as a function of the excess PbO target concentration is shown in Figure 5-17. It was seen that PZT (52/48) peak is broader for higher excess PbO concentrations in the target. Some peak splitting was also observed. The reason for this is currently unknown and needs to be investigated. Comparison of the cross-sectional

microstructure between these films (Figure 5-18) yields comparable results. All the microstructures are relatively dense for an initial growth thickness, while the grain boundaries become non-dense and curvy beyond that thickness. The weak dependence of the microstructure on the varying excess PbO content in the target implies that microsegregation of excess unreacted PbO is likely not the cause for the observed microstructure along the grain-boundaries.

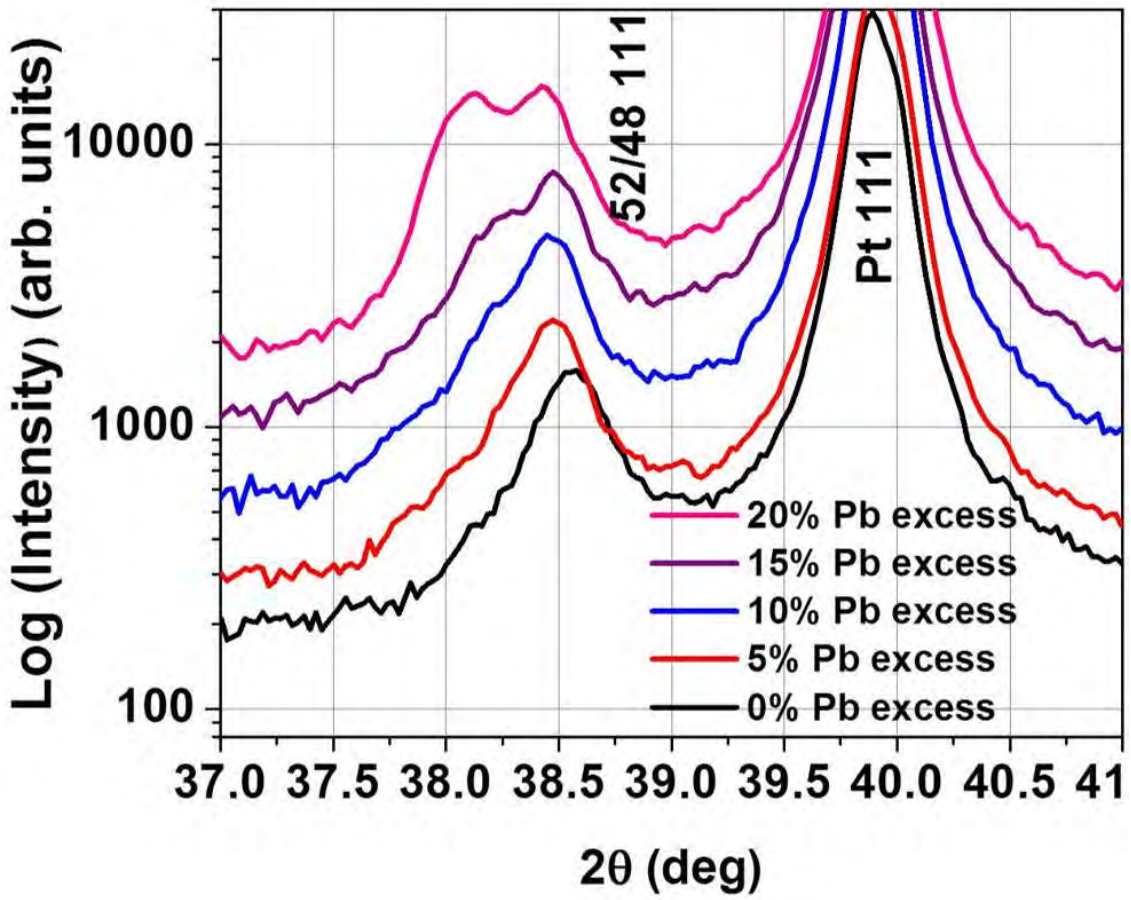

Figure 5-17: XRD 111 PZT peaks as a function of the excess Pb (PbO) in the target. (Ablation fluence: ~1.3 J/cm^2, pO_2: 85 mTorr (10% O_3), target-substrate distance: 6 cm, annealing energy density: ~55 mJ/cm^2, substrate temperature: ~350-370°C, frequency: 20Hz, film thickness: 600 – 700 nm)

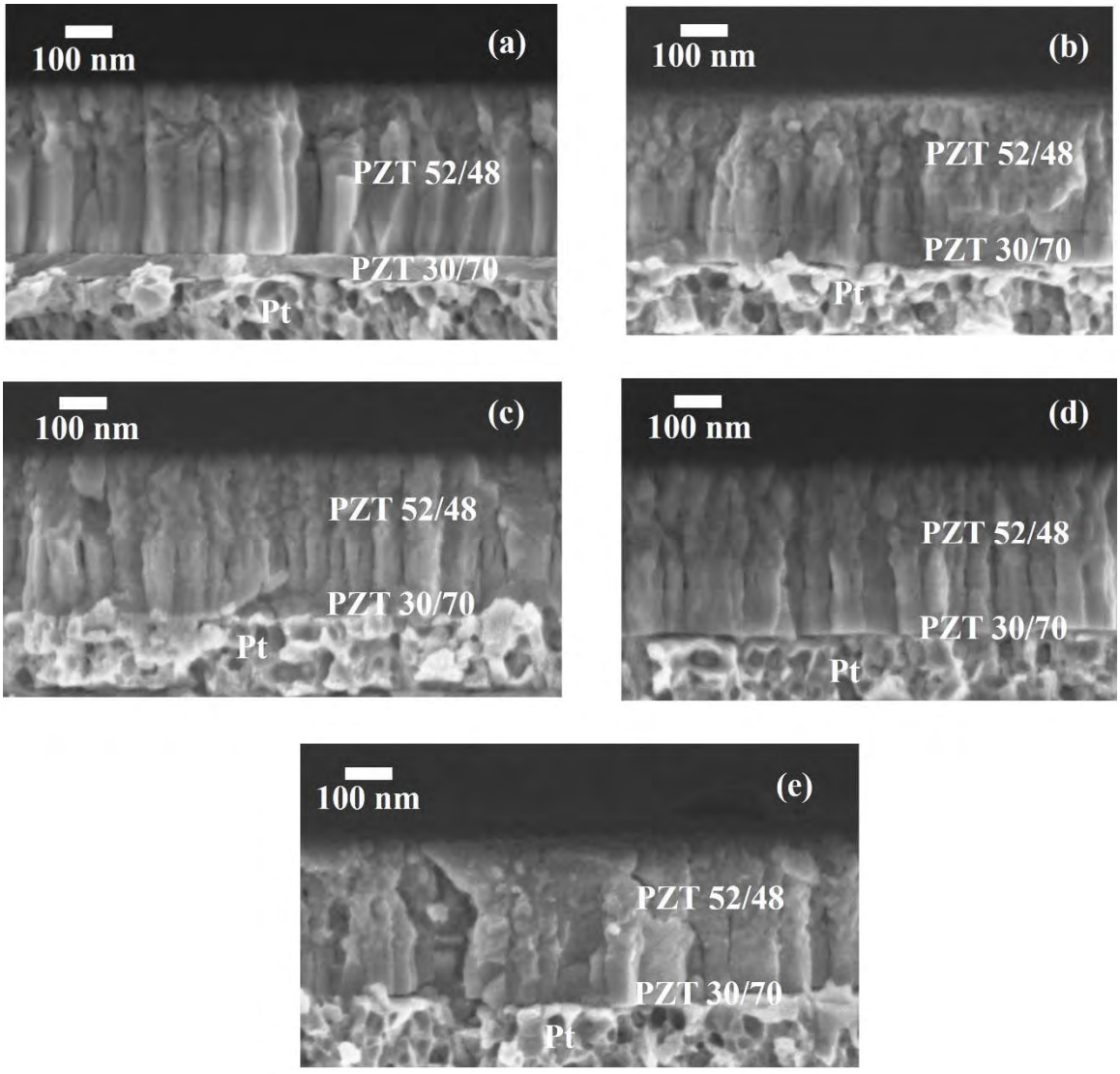

Figure 5-18: Cross-sectional micrographs showing the microstructure at various target excess PbO concentration ((a) 20%, (b) 15%, (c) 10%, (d) 5%, (e) 0%) (Ablation fluence: ~1.8 J/cm^2, pO_2: 85 mTorr (10% O_3), target-substrate distance: 6 cm, annealing energy density: ~55 mJ/cm^2, substrate temperature: ~350-370°C, frequency: 20 Hz, film thickness: 600 – 700 nm)

5.5 Conclusions

Simultaneous pulsed-laser heating during growth was utilized to crystallize PZT(52/48) thin films on PZT(30/70) seeded platinized-silicon substrates at a substrate-temperature of ~370 ˚C. Crystalline films were produced, but TEM measurements showed porosity

segregated at the grain boundaries under some conditions. It was demonstrated that the energy of the plume species played a dominant role in lateral densification and in affecting the grain sizes. Energy dispersive spectroscopy measurements showed that films were chemically homogeneous with no significant non-uniformity at the grain boundaries. The fine-grained columnar microstructure is preserved on varying the fractional laser annealing times, suggesting that nucleation and growth occurs in the direction normal to the substrate, with little or no lateral growth/densification due to laser annealing pulses. Reduction of excess PbO in the target didn't yield denser grain boundaries, pointing that PbO microsegregation at grain boundaries and subsequent evaporation is not the primary cause of the non-dense, curvy grain-boundaries.

Chapter 6 Conclusions and Future Work

6.1 Conclusions

The goal of this dissertation was to explore laser-induced crystallization as a means to crystallize $Pb(Zr_{1-x},Ti_x)O_3$ (PZT) thin films at substrate temperatures compatible with polymers and integrated circuits. It was shown that laser induced crystallization of ferroelectric PZT thin films could be achieved on polymeric substrates (Cu coated Epoxy-based Dielectric Film (EDF)) at substrate temperatures ~215°C. Amorphous sputtered PZT (30/70) films deposited at room temperature could be crystallized into the perovskite phase by laser crystallization at energy densities of ~50 – 85 mJ/cm^2, at timescales on the order of ~100 μs. Laser-induced crystallization of the perovskite phase was preferred in an oxygen environment, while including 10% ozone during the annealing was shown to stabilize the low temperature pyrochlore/fluorite phase. Tailoring of PbO content in the as-deposited films (via the Ar partial pressure used during rf sputtering) was necessary to induce crystallization; a high PbO content promoted nucleation of the perovskite phase. Furthermore, a target with higher excess PbO contents (20 mol%) was required to crystallize thinner films (~100 nm).

Laser-induced crystallization is thickness limited due to the limited heat diffusion depth of the absorbed laser pulse energy. To overcome this, layer-by-layer growth and crystallization was demonstrated to improve through-thickness crystallization in thicker films (~300 nm). Sequential growth and laser annealing allowed for nucleation from the

bottom interface. This yielded films with a grain size to the order of ~250 nm, compared to the films that nucleated primarily from the top surface (with effective grain sizes of the order of 2 microns). Ferroelectric switching was demonstrated for layer-by-layer grown and crystallized PZT on Pt/Ti/Cu/EDF based polymeric substrates. However, it was also seen that the presence of a thick buffer layer (such as oxides, metal) might be necessary to reduce heating of the underlying polymer.

High volume manufacturing (HVM) dictates simultaneous laser annealing during growth as an efficient means of crystallizing thicker films. To this end, a pulsed laser deposition system with simultaneous laser irradiation for *in situ* crystallization was designed and built. Films produced with this technique were of comparable quality to conventionally processed films (with remanent polarization ~25 $\mu C/cm^2$, and coercive field ~50 kV/cm), however with highly columnar grains possessing extremely fine grain sizes of the order of ~30 nm; this pointed to a nucleation dominated process. The energy of the plume species was important in dictating lateral densification; this was used as a tool to control grain sizes. However, varying the annealing durations had little impact on the observed microstructure, producing highly fine columnar grains, suggesting that diffusion length scales due to the short laser pulses are limited.

6.2 Suggestions for Future Work

6.2.1 Crystallization as a Function of Substrate Temperature and Film Thickness

In order to understand the applicability of the laser annealing process to a wider variety of substrates (with varying degrees of thermal stabilities), the crystallization and microstructure evolution of PZT films should be explored as a function of substrate temperature. Although, an extensive literature on this subject is lacking in the case of oxides, the crystallization velocity as a function of substrate temperature has been studied for laser annealing of Ge thin films (Figure 6-1) [106].

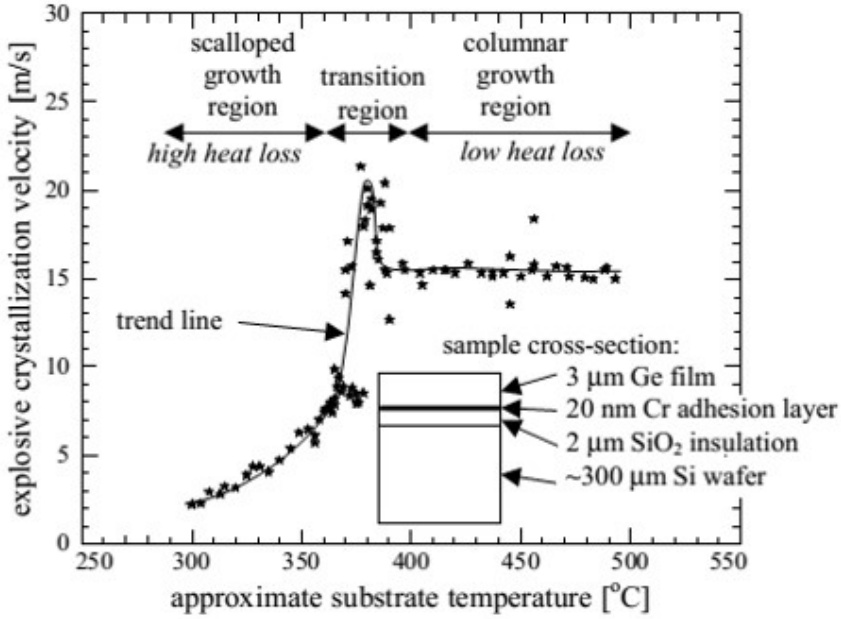

Figure 6-1: Measured crystallization velocity in case of 3 micron thick Ge films on Nd:YAG laser irradiation (wavelength: 1064 nm, pulsewidth: 5 ns) as a function of substrate temperature [106]**.**

It was seen that for lower substrate temperatures, the amount of heat loss to the substrate increased, causing the film crystallization velocity to decrease. Furthermore, below a certain substrate temperature, no crystallization was observed. On the other hand, at higher

substrate temperatures, a high crystallization velocity was observed until a saturation value was achieved.

The crystallization velocity should also be a function of the film thickness. It was demonstrated in the case of laser-induced crystallization of amorphous Ge films [99] that smaller thicknesses cause high heat loss (conduction into the substrate and radiative losses), reducing the crystallization velocity. Furthermore, for a given substrate temperature, there exists a minimum thickness below which explosive crystallization will not be achieved [107]. Thus, thinner films necessitated higher substrate temperatures to initiate explosive crystallization Figure 6-2 [99].

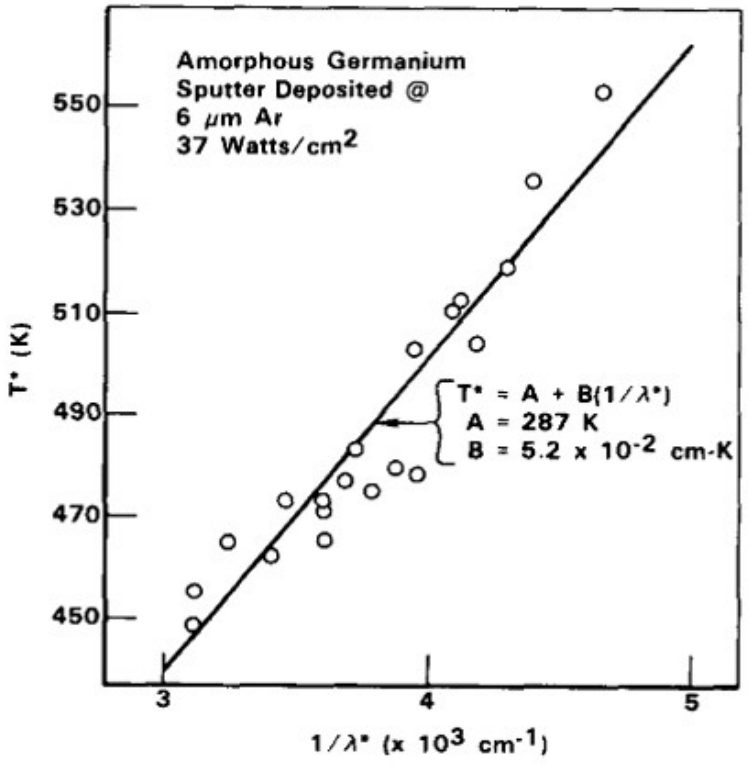

Figure 6-2 Minimum substrate temperature (T*) required to crystallize a Ge film with thickness λ* (from Ref. [99]**)**

It is possible that similar trends in crystallization will exist for laser-induced crystallization of PZT films. Thus, it would be interesting to determine experimentally the limits for film thickness and substrate temperature required to crystallize a given layer. A detailed Temperature-Time-Transformation analysis of crystallization is recommended to understand the limitations of the process. This would also ultimately control the minimum thickness of a laser crystallized seed layer at a given substrate temperature. Controlled crystallization of the seed layer would also be important in order to ensure a good interface devoid of defects/untransformed material.

6.2.2 Real-Time Spectroscopic Ellipsometry (RTSE)

The *in situ* laser annealing system is capable of real time characterization of the growing film using real time spectroscopic ellipsometry (RTSE). RTSE allows for continuous monitoring of the film thickness and film optical properties during growth [108]. Using this technique, an *in situ* crystallization of the seed layer can be envisaged wherein a certain thickness (dictated by the minimum thickness that can be explosively crystallized at the given substrate temperature) is first deposited and immediately laser annealed without breaking the vacuum. In this work, the seed layers were *ex situ* processed (by laser annealing or rapid thermal annealing) in a separate chamber before growing a film with *in situ* laser annealing. Optimization of parameters for an *in situ* preparation of seed layer is expected to result in further improvement.

The growth and crystallization kinetics can be tracked simultaneously using RTSE. In this case, the optical properties should lie between that of the non-converted amorphous/pyrochlore phase and the crystallized perovskite phase. Furthermore, variations in film density through the depth, as well as the evolution of surface roughness can be

tracked. Any compositional gradients [109] arising due to differential diffusion rates of various ions in the oxide system (especially Pb^{2+}) can be characterized *in situ* using this technique, and will be key for understanding the process. Furthermore, incorporation and evaporation of unreacted excess PbO (which leaves behind pores) in the microstructure can be closely monitored.

An example of the dynamic measurement of RTSE parameters Psi (ψ) and Delta (Δ) during the growth of PZT (52/48) thin film using the *in situ* laser annealing system (but without any substrate rotation) is shown in Figure 6-3. However, in order for successful integration of the RTSE with *in situ* laser annealing, a few challenges should be addressed. First and foremost, since the deposition/annealing currently utilizes substrate rotation for uniform large area deposition, close attention need to be paid to reduce the substrate wobble to a minimum. A substrate wobble would be detrimental if the reflected source beam misses the ellipsometer detector. Also, if a small substrate sample is used for deposition, while the substrate holder is rotated, the ellipsometer beam would not see the sample for the part of the time; the sample is not in the view. In order to solve this, a substrate 'jog' feature can be implemented, wherein instead of carrying out the whole continuous rotation, the sample just rocks back and forth by a certain angle. In this way, a reasonably sized sample can be used for real-time ellipsometry studies of the growth process. Another important point to be noted is that due to the finite area of the annealing laser beam, care should be taken during alignment, so that only data from the annealed regions of the sample (and not from the peripheral regions) is collected.

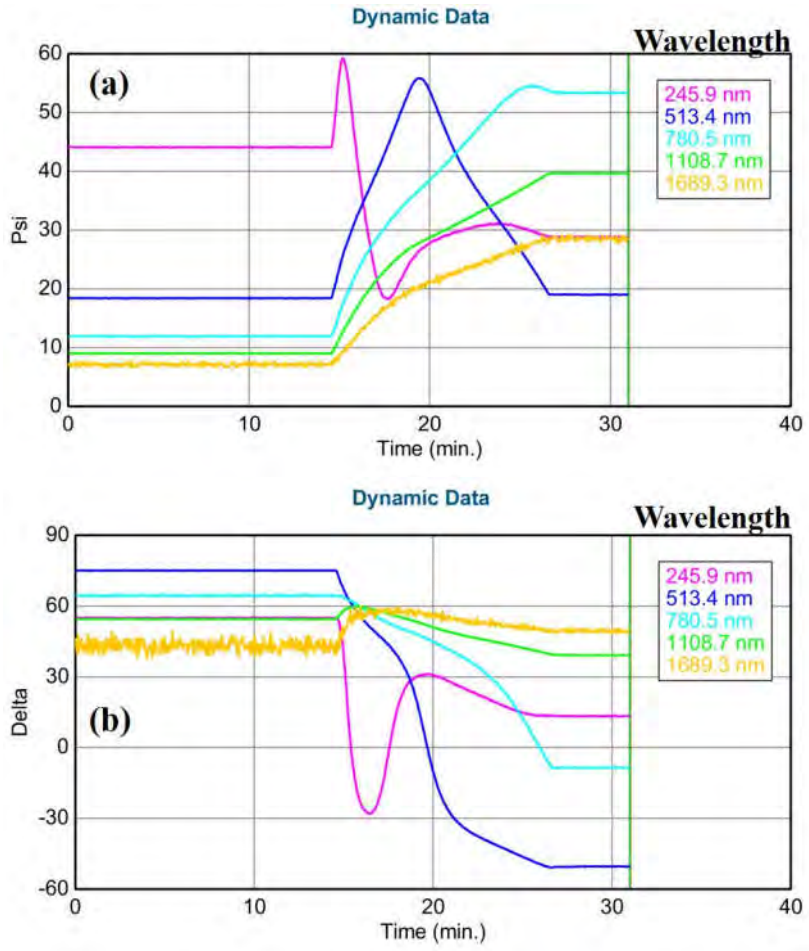

Figure 6-3: Dynamic measurement of the ellipsometric quantities Psi (ψ) and Delta (Δ) for various incident wavelengths (and at incident angle: 75°) as a function of growth time for PZT (52/48). The growth/annealing pulses (with frequency 20 Hz) were switched on at 14.5 min and switched off at 26.5 min (amounting to a total deposition time of 12 min). In order to avoid misalignment of the reflected ellipsometric beam with respect to the detector due to inherent substrate wobble, no substrate rotation was used in this measurement.

6.2.3 Measurement of Residual Stresses

Residual stresses are produced as a result of film growth. As shown in this dissertation, a low adatom mobility condition exists between the laser annealing pulses. Existing literature on evaporation of metal thin films suggested the development of a tensile residual stress in growth of high melting point (low adatom mobility) metal films [110]. The origin of the

residual stresses in thin films has been discussed by several authors [111],[102],[112],[113],[100]. One of the key factors is the constrained coalescence of the individual crystallites to form a grain boundary [102][60]. This so-called 'grain boundary zipping' produces a tensile stress, and can be seen as a reverse of a Griffith's crack formation [110].

The inbuilt tensile stress on grain boundary formation can be given by [60]:

$$\sigma = \frac{Y \Delta p}{(1-\nu) l_g}$$

where Y: Young's modulus, ν: Poisson's ratio, l_g: average grain size, Δ: constrained relaxation length or gap and p: packing density of the film [60]. It can be clearly seen that lower grain sizes produce higher associated residual stresses. In the case of *in situ* laser annealing of PZT, it can be argued that high adatom mobilities, albeit for very short intervals (~μs), are provided by the laser pulses which may serve to structurally relax the material. However, it is possible that the small grain sizes dictated by high nucleation rates prevent complete coalescence (coalescence of small grains with their inherent higher total surface energies would mean higher elastic strain energy generated). To assess how the stresses evolve in laser annealed films, residual stresses should be measured by bending of micro-cantilever beams (suitable for small samples) and application of the Stoney's formula [84]. Residual stresses heavily impact film properties and can be correlated to the polarization-electric field hysteresis loop rotations [114] and the Rayleigh analysis of the minor hysteresis loops.

6.2.4 Local Measurements of Domain Wall Mobility by Band-Excitation PFM (BE-PFM)

The fraction of the irreversible contribution to the piezoelectric effect ($\alpha_d/d_{33,init}$) due to domain wall mobility can be extracted using Rayleigh's law [115]. It is known that a decrease in the grain size of piezoelectric ceramics causes an ensuing reduction in the piezoelectric coefficients as a result of a reduction in the extrinsic contribution [116],[117]. In general, the density of non-180° domain walls (i.e. the ones that are generally involved in the extrinsic piezoelectric contribution) increase with reduction in grain size (along with a subsequent reduction in domain size) [116]. The cooperative motion of domains across the grain boundaries will be hindered in fine-grained material due to relatively small density of the twin walls [116]. Typically, the domain wall mobility is reduced with large domain wall densities characteristic of small grain sizes [118]. There is also a further reduction in the extrinsic response due to large density of the grain-boundaries (which can act as pinning centers for domain wall motion) [119].

It was shown in this thesis that crystallization of ferroelectric PZT thin films with *in situ* laser annealing produces grain sizes of the order of ~30 nm diameter (much smaller than those characteristic of conventionally processed thin films). This presumably should provide access to high domain wall densities, and so might be useful in probing domain wall pinning and cooperative motion of domain walls across the grain boundaries. Band-excitation PFM allows for local measurements of piezoelectric non-linearity using Rayleigh measurements [120]. In general, maps of $\alpha_d/d_{33,init}$ obtained by this technique have shown clusters with length scales larger than the average grain size of the thin film [121].

6.2.5 Extension of *In Situ* Laser Annealing to Other Systems

Laser annealing has been shown to crystallize oxides such as lead zirconate titanate [41], [51], barium strontium titanate [43] [122], lanthanum strontium manganite [123], [44], and bismuth zinc niobate [46] among others. Bismuth zinc niobate (BZN) pyrochlores can be utilized for dielectric energy storage and would benefit from low temperature integration onto polymers for applications in flexible electronics [124]. Preliminary results (Figure 6-4) on *in situ* laser annealing of BZN films on a ~50 nm thick laser crystallized BZN seed layer on a platinized silicon substrate proves the wide applicability of the process and also opens up avenues for various applications integrated with a wide variety of substrates.

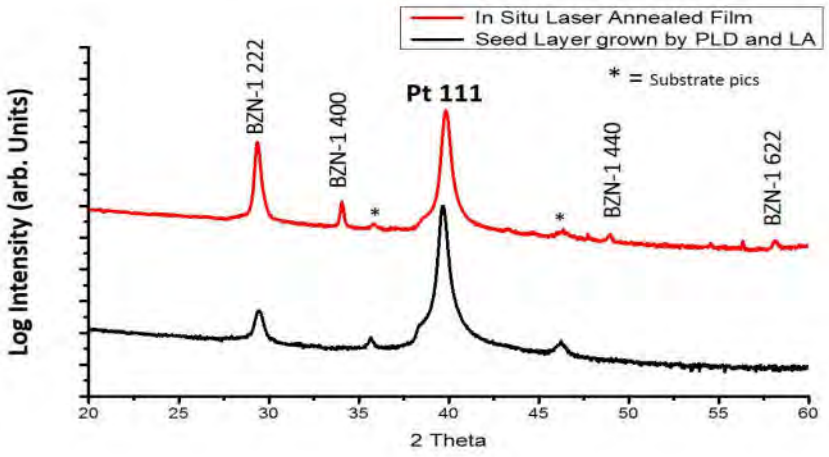

Figure 6-4 *In situ* laser annealing of ~310 nm thick BZN film (BZN-1: $Bi_{1.5}Zn_{1.0}Nb_{1.5}O_7$; laser fluence: ~1.6 -1.8 J/cm^2, Target-Substrate distance: 6 cm, Substrate temperature: 360 – 380°C, annealing energy density: 40-50 mJ/cm^2, pO_2 (with 10% Ozone): 120 mTorr, growth rate: ~0.1 Angstrom/pulse) on *ex situ* laser crystallized BZN seed layer. (LA: Laser Annealed)

References

[1] M. Ghoneim and M. Hussain, "Review on Physically Flexible Nonvolatile Memory for Internet of Everything Electronics," *Electronics*, vol. 4, no. 3, pp. 424–479, 2015.

[2] A. Carlson, A. M. Bowen, Y. Huang, R. G. Nuzzo, and J. A. Rogers, "Transfer Printing Techniques for Materials Assembly and Micro/Nanodevice Fabrication," *Adv. Mater.*, vol. 24, no. 39, pp. 5284–5318, 2012.

[3] G. A. Kachurin, N. B. Pridachin, and L. S. Smirnov, "Annealing of Radiation Defects by Laser Radiation Pulses," *Sov. Phys. Semicond.*, vol. 9, no. 7, pp. 946–946, 1975.

[4] I. B. Khaibullin, E. I. Shtyrkov, M. M. Zaripov, R. M. Bayazitov, and M. F. Galjautdinov, "Some Features of Laser Annealing of Implanted Si Layers," *Radiat. Eff.*, vol. 36, no. 3–4, pp. 225–233, 1978.

[5] P. Baeri and E. Rimini, "Laser Annealing of Silicon," *Mater. Chem. Phys.*, vol. 46, no. 2–3, pp. 169–177, Nov. 1996.

[6] S. C. Lai, H.-T. Lue, K. Y. Hsieh, S. L. Lung, R. Liu, T. B. Wu, P. P. Donohue, and P. Rumsby, "Extended-pulse Excimer Laser Annealing of $Pb(Zr_{1-x}Ti_x)O_3$ Thin Film on $LaNiO_3$ Electrode," *J. Appl. Phys.*, vol. 96, no. 5, pp. 2779–2784, 2004.

[7] J. T. Evans and R. Womack, "An Experimental 512- bit Nonvolatile Memory with Ferroelectric Storage Cell," *IEEE J. Solid-State Circuits*, vol. 23, no. 5, pp. 1171–

1175, 1988.

[8] Y. Arimoto and H. Ishiwara, “Current Status of Ferroelectric Random-Access Memory,” *MRS Bull.*, vol. 29, no. 11, pp. 823–828, 2004.

[9] K. Kim and S. Lee, “Integration of Lead Zirconium Titanate Thin Films for High Density Ferroelectric Random Access Memory,” *J. Appl. Phys.*, vol. 100, no. 5, p. 051604, 2006.

[10] L.-P. Wang, K. Deng, L. Zou, R. Wolf, R. J. Davis, and S. Trolier-McKinstry, “Microelectromechanical Systems (MEMS) Accelerometers Using Lead Zirconate Titanate Thick Films,” *IEEE Electron Device Lett.*, vol. 23, no. 4, pp. 182–184, Apr. 2002.

[11] P. Muralt, R. G. Polcawich, and S. Trolier-McKinstry, “Piezoelectric Thin Films for Sensors, Actuators, and Energy Harvesting,” *MRS Bull.*, vol. 34, pp. 658–664, 2011.

[12] P. Muralt, “Piezoelectric Thin Films for MEMS,” *Integr. Ferroelectr.*, vol. 17, no. 1997, pp. 297–307, 1997.

[13] S. Tadigadapa and K. Mateti, “Piezoelectric MEMS Sensors: State-of-the-art and Perspectives,” *Meas. Sci. Technol.*, vol. 20, no. 9, p. 092001, Sep. 2009.

[14] M. Mandeljc, M. Kosec, B. Malič, and Z. Samardzija, “Low Temperature Processing of Lanthanum Doped PZT Thin Films,” *Integr. Ferroelectr.*, vol. 30, no. 1–4, pp. 149–156, 2000.

[15] S. Trolier-McKinstry, F. Griggio, C. Yaeger, P. Jousse, D. Zhao, S. S. N. Bharadwaja, T. N. Jackson, S. Jesse, S. V Kalinin, and K. Wasa, “Designing

Piezoelectric Films for Micro Electromechanical Systems," *IEEE Trans. Ultrason. Ferroelectr. Freq. Control*, vol. 58, no. 9, pp. 1782–92, Sep. 2011.

[16] T. D. Nguyen, N. Deshmukh, J. M. Nagarah, T. Kramer, P. K. Purohit, M. J. Berry, and M. C. McAlpine, "Piezoelectric Nanoribbons for Monitoring Cellular Deformations," *Nat. Nanotechnol.*, vol. 7, no. 9, pp. 587–593, 2012.

[17] H. Hida, S. Yagami, A. Sakurai, and I. Kanno, "High-Productive Fabrication Method of Flexible Piezoelectric Substrate," *MEMS 2015, Estoril, Port.*, pp. 377–380, 2015.

[18] K.-I. Park, C. K. Jeong, J. Ryu, G.-T. Hwang, and K. J. Lee, "Flexible and Large-Area Nanocomposite Generators Based on Lead Zirconate Titanate Particles and Carbon Nanotubes," *Adv. Energy Mater.*, vol. 3, no. 12, pp. 1539–1544, 2013.

[19] C. Dagdeviren, B. D. Yang, Y. Su, P. L. Tran, P. Joe, E. Anderson, J. Xia, V. Doraiswamy, B. Dehdashti, X. Feng, B. Lu, R. Poston, Z. Khalpey, R. Ghaffari, Y. Huang, M. J. Slepian, and J. A. Rogers, "Conformal Piezoelectric Energy Harvesting and Storage from Motions of the Heart, Lung, and Diaphragm," *Proc. Natl. Acad. Sci.*, vol. 111, no. 5, pp. 1927–1932, 2014.

[20] G. K. Fedder, R. T. Howe, T.-J. King Liu, and E. P. Quevy, "Technologies for Cofabricating MEMS and Electronics," *Proc. IEEE*, vol. 96, no. 2, pp. 306–322, 2008.

[21] R. W. Whatmore, P. B. Kirby, A. Patel, N. M. Shorrocks, T. Bland, and M. Walker, "Ferroelectric Thin Films for Capacitor and Sensor Applications," in *Proceedings NATO Advanced Research Workshop on Science and Technology of Electroceramic*

Thin Films, 1994, pp. 383–397.

[22] H. Takeuchi, A. Wung, X. Sun, R. T. Howe, and K. Tsu-Jae, "Thermal Budget Limits of Quarter-Micrometer Foundry CMOS For Post-Processing MEMS Devices," *IEEE Trans. Electron Devices*, vol. 52, no. 9, pp. 2081–2086, 2005.

[23] R. E. Jones, P. D. Maniar, R. Moazzami, P. Zurcher, J. Z. Witowski, Y. T. Lii, P. Chu, and S. J. Gillespie, "Ferroelectric Non-Volatile Memories for Low-Voltage, Low-Power Applications," *Thin Solid Films*, vol. 270, no. 1–2, pp. 584–588, 1995.

[24] T. Hase, T. Noguchi, and Y. Miyasaka, "Analysis of the Degradation of PZT and $SrBi_2Ta_2O_9$ Thin Films with a Reductive Process," *Integr. Ferroelectr.*, vol. 16, pp. 29–40, 1997.

[25] P. Muralt, "PZT Thin Films for Microsensors and Actuators: Where Do We Stand?," *IEEE Trans. Utrasonics, Ferroelectr. Freq. Control*, vol. 47, no. 4, pp. 903–15, Jan. 2000.

[26] C. K. Kwok and S. B. Desu, "Low Temperature Perovskite Formation of Lead Zirconate Titanate Thin Films by a Seeding Process," *J. Mater. Res.*, vol. 8, no. 02, pp. 339–344, Jan. 1993.

[27] H. E. Brown, *Lead Oxide: Properties and Applications*. Ney York: International Lead Zinc Research Organization, 1985.

[28] C. V. R. V. Kumar, M. Sayer, R. Pascual, D. T. Amm, Z. Wu, and D. M. Swanston, "Lead Zirconate Titanate Films by Rapid Thermal Processing," *Appl. Phys. Lett.*, vol. 58, no. 11, p. 1161, 1991.

[29] H. Hu, C. J. Peng, and S. B. Krupanidhi, “Effect of Heating Rate on the Crystallization Behavior of Amorphous PZT Thin Films,” *Thin Solid Films*, vol. 223, no. 2, pp. 327–333, Feb. 1993.

[30] R. Roy, “Gel Route to Homogeneous Glass Preparation,” *J. Am. Ceram. Soc.*, vol. 52, no. 6, p. 344, 1969.

[31] R. W. Schwartz, “Chemical Solution Deposition of Perovskite Thin Films,” *Chem. Mater.*, vol. 9, no. 11, pp. 2325–2340, 1997.

[32] D. Bauerle, *Laser Processing and Chemistry*, Fourth Edi. Springer Berlin Heidelberg.

[33] M. von Allmen and A. Blatter, *Laser-Beam Interactions with Materials*, 2nd Ed. Springer US, 1995.

[34] J. M. Poate and J. W. Mayer, *Laser Annealing of Semiconductors*. Academic Press, 1982.

[35] M. Darif and N. Semmar, “Numerical Simulation of Si Nanosecond Laser Annealing by COMSOL Multiphysics,” *Excerpt from Proc. COMSOL Conf. 2008 Hann.*, 2008.

[36] J. W. Christian, *The Theory of Transformations in Metals and Alloys (Part I and II)*. 2002.

[37] M. Avrami, “Kinetics of Phase Change I,” *J. Chem. Phys.*, vol. 7, no. 1930, pp. 1103–1112, 1939.

[38] M. Avrami, “Kinetics of Phase Change. II - Transformation-Time Relations for

Random Distribution of Nuclei," *J. Chem. Phys.*, vol. 8, no. 1940, pp. 212–224, 1940.

[39] C. Kwok and S. B. Desu, "Formation Kinetics of $PbZr_xTi_{1-x}O_3$ Thin Films," *J. Mater. Res.*, vol. 9, no. 7, pp. 1728–1733, 1994.

[40] Y. Zhu, J. Zhu, Y. J. Song, and S. B. Desu, "Laser-Assisted Low Temperature Processing of Pb(Zr, Ti)O_3 Thin Film," *Appl. Phys. Lett.*, vol. 73, no. 14, pp. 1958–1960, 1998.

[41] S. Bharadwaja, J. Kulik, R. Akarapu, H. Beratan, and S. Trolier-McKinstry, "Ultrafast Crystallization Kinetics in (Pb, La)$(Zr_{0.30}Ti_{0.70})O_3$ Thin Films by Pulsed Excimer Laser Annealing," *IEEE Trans. Ultrason. Ferroelectr. Freq. Control*, vol. 57, no. 10, pp. 2182–2191, 2010.

[42] O. Baldus and R. Waser, "Experimental and Numerical Investigations of Heat Transport and Crystallization Kinetics in Laser-induced Modification of Barium Strontium Titanate Thin Films," *Appl. Phys. A*, vol. 80, no. 7, pp. 1553–1562, Jul. 2004.

[43] O. Baldus and R. Waser, "Laser Crystallization Studies of Barium Strontium Titanate Thin Films," *J. Eur. Ceram. Soc.*, vol. 24, no. 10–11, pp. 3013–3020, Sep. 2004.

[44] T. Nakajima, T. Tsuchiya, M. Ichihara, H. Nagai, and T. Kumagai, "Epitaxial Growth Mechanism for Perovskite Oxide Thin Films under Pulsed Laser Irradiation in Chemical Solution Deposition Process," *Chem. Mater.*, vol. 20, pp. 7344–7351, 2008.

[45] T. Nakajima, T. Tsuchiya, M. Ichihara, H. Nagai, and T. Kumagai, "Effective-Time of Pulsed Photothermal Heating for Polycrystalline Nucleation of Perovskite Oxide Films from an Amorphous Matrix," *Appl. Phys. Express*, vol. 2, p. 023001, Jan. 2009.

[46] J.-G. Cheng, J. Wang, T. Dechakupt, and S. Trolier-McKinstry, "Low-Temperature Crystallized Pyrochlore Bismuth Zinc Niobate Thin Films by Excimer Laser Annealing," *Appl. Phys. Lett.*, vol. 87, no. 23, p. 232905, 2005.

[47] H. Lee, Y. S. Kang, S.-J. Cho, B. Xiao, H. Morkoç, T. D. Kang, G. S. Lee, J. Li, S.-H. Wei, P. G. Snyder, and J. T. Evans, "Dielectric Functions and Electronic Band Structure of Lead Zirconate Titanate Thin Films," *J. Appl. Phys.*, vol. 98, no. 9, p. 094108, 2005.

[48] X. M. Lu, J. S. Zhu, W. S. Hu, Z. G. Liu, and Y. N. Wang, "Pulsed Excimer (KrF) Laser Induced Crystallization of $PbZr_{0.44}Ti_{0.56}O_3$ Amorphous Films," *Appl. Phys. Lett.*, vol. 66, no. 19, pp. 2481–2483, 1995.

[49] Z.-G. Ye, Ed., *Handbook of Advanced Dielectric, Piezoelectric and Ferroelectric Materials: Synthesis, Properties and Applications*. Woodhead Publishing, 2008.

[50] X. M. Lu, J. S. Zhu, X. F. Huang, C. Y. Lin, and Y. N. Wang, "Laser-Induced Phase Transformation from Amorphous to Perovskite in $PbZr_{0.44}Ti_{0.56}O_3$ Films with the Substrate at Room Temperature," *Appl. Phys. Lett.*, vol. 65, no. 16, pp. 2015–2017, 1994.

[51] S. S. N. Bharadwaja, F. Griggio, J. Kulik, and S. Trolier-McKinstry, "Highly Textured Laser Annealed $Pb(Zr_{0.52}Ti_{0.48})O_3$ Thin Films," *Appl. Phys. Lett.*, vol. 99,

no. 4, p. 042903, 2011.

[52] A. Queralto, A. Perez Del Pino, M. De La Mata, J. Arbiol, M. Tristany, A. Gomez, X. Obradors, and T. Puig, "Growth of Ferroelectric $Ba_{0.8}Sr_{0.2}TiO_3$ Epitaxial Films by Ultraviolet Pulsed Laser Irradiation of Chemical Solution Derived Precursor Layers," *Appl. Phys. Lett.*, vol. 106, p. 262903, 2015.

[53] A. Queraltó, A. Pérez del Pino, M. de la Mata, J. Arbiol, X. Obradors, and T. Puig, "Ultrafast Crystallization of $Ce_{0.9}Zr_{0.1}O_{2-y}$ Epitaxial Films on Flexible Technical Substrates by Pulsed Laser Irradiation of Chemical Solution Derived Precursor Layers," *Cryst. Growth Des.*, vol. 15, no. 4, pp. 1957–1967, 2015.

[54] Y.-R. Luo, *Handbook of Bond Dissociation Energies in Organic Compounds*. CRC Press, 2002.

[55] T. Tsuchiya, I. Yamaguchi, T. Manabe, T. Kumagai, and S. Mizuta, "Effect of Substrates on Epitaxial PZT Films by a Coating Photolysis Process," in *Materials Science in Semiconductor Processing*, 2002, vol. 5, no. 2–3, pp. 207–210.

[56] H. Palneedi, D. Maurya, G.-Y. Kim, S. Priya, S.-J. L. Kang, K.-H. Kim, S.-Y. Choi, and J. Ryu, "Enhanced Off-Resonance Magnetoelectric Response in Laser Annealed PZT Thick Film Grown on Magnetostrictive Amorphous Metal Substrate," *Appl. Phys. Lett.*, vol. 107, no. 1, p. 012904, 2015.

[57] S. Otsubo, T. Minamikawa, Y. Yonezawa, T. Maeda, A. Moto, A. Morimoto, and T. Shimizu, "Preparation of Ba-Y-Cu-O Superconducting Films by Laser Ablation with and without Laser Irradiation on Growing Surface," *Jpn. J. Appl. Phys.*, vol. 27, no. 12, pp. L2442–L2444, 1988.

[58] H. Tabata, T. Kawai, S. Kawai, O. Murata, J. Fujioka, and S. Minakata, "Preparation of $PbTiO_3$ Thin Films at Low Temperature by an Excimer Laser Ablation Technique," *Appl. Phys. Lett.*, vol. 59, no. 19, p. 2354, 1991.

[59] H. Tabata, O. Murata, T. Kawai, S. Kawai, and M. Okuyama, "Preparation of $PbTiO_3$ Thin Films by an Excimer Laser Ablation Technique with Second Laser Irradiation," *Jpn. J. Appl. Phys.*, 1992.

[60] M. Ohring, *Materials Science of Thin Films: Deposition and Structure*, 2nd ed. Elsevier, 2001.

[61] J. Maria, "Deposition and Measurement of Epitaxial Barium Titanate Thin Films using Conductive Epitaxial Oxide Electrodes Prepared by Pulsed Laser Deposition," Pennsylvania State University, 1996.

[62] [Online], "Material Property Data," *www.matweb.com*. [Online]. Available: www.matweb.com. [Accessed: 30-Jun-2015].

[63] R. A. Young and D. B. Wiles, "Profile Shape Functions in Rietveld Refinements," *J. Appl. Crystallogr.*, vol. 15, no. 4, pp. 430–438, 1982.

[64] *CompleteEASE Software Manual*. J.A. Woollam Co.

[65] H. Fujiwara, *Spectroscopic Ellipsometry: Principles and Applications*. John Wiley & Sons, 2007.

[66] B. Johs, R. H. French, F. D. Kaik, W. A. Mcgahan, and J. A. Woollam, "Optical Analysis of Complex Multilayer Structures Using Multiple Data Types," *SPIE Proc.*, vol. 2253, pp. 1098–1106, 1994.

[67] J.-P. Maria, J. F. Shepard, and Susan Trolier-McKinstry, “Characterization of the Piezoelectric Properties of $Pb_{0.98}Ba_{0.02}(Mg_{1/3}Nb_{2/3})O_3$-$PbTiO_3$ Epitaxial Thin Films,” *Int. J. Appl. Ceram. Technol.*, vol. 2, no. 1, pp. 51–58, 2005.

[68] C. Yeager, “PZT Thin Films for Piezoelectric MEMS Mechanical Energy Harvesting,” Pennsylvania State University, 2015.

[69] K.-I. Park, J. H. Son, G.-T. Hwang, C. K. Jeong, J. Ryu, M. Koo, I. Choi, S. H. Lee, M. Byun, Z. L. Wang, and K. J. Lee, “Highly-Efficient, Flexible Piezoelectric PZT Thin Film Nanogenerator on Plastic Substrates.,” *Adv. Mater.*, vol. 26, no. 16, pp. 2514–2520, Apr. 2014.

[70] Y. Qi, N. T. Jafferis, K. Lyons, C. M. Lee, H. Ahmad, and M. C. McAlpine, “Piezoelectric Ribbons Printed onto Rubber for Flexible Energy Conversion,” *Nano Lett.*, vol. 10, no. 2, pp. 524–525, 2010.

[71] Y. Qi, J. Kim, T. D. Nguyen, B. Lisko, P. K. Purohit, and M. C. McAlpine, “Enhanced Piezoelectricity and Stretchability in Energy Harvesting Devices Fabricated from Buckled PZT Ribbons,” *Nano Lett.*, vol. 11, no. 3, pp. 1331–1336, 2011.

[72] I. Bretos, R. Jiménez, A. Wu, A. I. Kingon, P. M. Vilarinho, and M. L. Calzada, “Activated Solutions Enabling Low-Temperature Processing of Functional Ferroelectric Oxides for Flexible Electronics,” *Adv. Mater.*, vol. 26, no. 9, pp. 1405–1409, 2014.

[73] R. H. T. Wilke, R. L. Johnson-Wilke, V. Cotroneo, W. N. Davis, P. B. Reid, D. Schwartz, and S. Trolier-McKinstry, “Sputter Deposition of PZT Piezoelectric

Films on Thin Glass Substrates for Adjustable X-Ray Optics.," *Appl. Opt.*, vol. 52, no. 14, pp. 3412–3419, 2013.

[74] K. Iijima, Y. Tomita, R. Takayama, and I. Ueda, "Preparation of c-axis Oriented $PbTiO_3$ Thin Films and their Crystallographic, Dielectric, and Pyroelectric Properties," *J. Appl. Phys.*, vol. 60, no. 1, pp. 361–367, 1986.

[75] A. Gras-Marti and J. A. Valles-Abarca, "Slowing Down and Thermalization of Sputtered Particle Fluxes: Energy Distributions," *J. Appl. Phys.*, vol. 54, no. 2, pp. 1071–1075, 1983.

[76] S. W. Jiang, Q. Y. Zhang, W. Huang, B. Jiang, Y. Zhang, and Y. R. Li, "Texture Control of $Pb(Zr, Ti)O_3$ Thin Films with Different Post-Annealing Processes," *Appl. Surf. Sci.*, vol. 252, no. 24, pp. 8756–8759, 2006.

[77] A. M. S. Chowdhury, "Photodissociation of Ozone at 248 nm and Vacuum Ultraviolet Laser-Induced Fluorescence Detection of O(1D)," *Laser Chem.*, vol. 17, no. 4, pp. 191–203, 1998.

[78] L. A. Bursill and K. G. Brooks, "Crystallization of Sol-gel Derived Lead-Zirconate-Titanate Thin Films in Argon and Oxygen Atmospheres," *J. Appl. Phys.*, vol. 75, no. 9, pp. 4501–4509, 1994.

[79] M. G. Cain, "Dielectric Breakdown in Dielectrics and Ferroelectric Ceramics," in *Characterisation of Ferroelectric Bulk Materials and Thin Films*, Springer US, 2014.

[80] B. Jaffe, R. S. Roth, and S. Marzullo, "Piezoelectric Properties of Lead Zirconate-

Lead Titanate Solid-Solution Ceramics," *J. Appl. Phys.*, vol. 25, no. 6, pp. 809–810, 1954.

[81] D. Bolten, U. Böttger, and R. Waser, "Reversible and Irreversible Polarization Processes in Ferroelectric Ceramics and Thin Films," *J. Appl. Phys.*, vol. 93, no. 3, pp. 1735–1742, 2003.

[82] D. P. Gosain, "Excimer Laser Crystallized Poly-Si TFTs on Plastic Substrates," *Proc. SPIE*, vol. 4426, pp. 394–400, Feb. 2002.

[83] P. M. Smith, P. G. Carey, and T. W. Sigmon, "Excimer Laser Crystallization and Doping of Silicon Films on Plastic Substrates," *Appl. Phys. Lett.*, vol. 70, no. 1997, pp. 342–344, 2001.

[84] D. L. Smith, *Thin-Film Deposition: Principles and Practice*. McGraw-Hill, 1995.

[85] Y. Zhu, J. Zhu, Y. J. Song, and S. B. Desu, "Laser-assisted low temperature processing of PZT thin films," *Mater. Res. Soc. Symp. Proc.*, vol. 493, pp. 305–309, 1998.

[86] T. Nishiwaki, K. Sumi, M. Murai, and M. Shimada, "Piezoelectric Thin-Film Device Process for Manufacturing the same, and Ink-Jet Recording Head Using the same," 2000.

[87] R. Roy and K. Etzold, "Substrate and Temperature Effects in Lead Zirconate Titanate Films Produced by Facing Targets Sputtering," *J. Mater. Res.*, vol. 7, no. 6, pp. 1455–1464, 1992.

[88] J. S. Horwitz, K. S. Grabowski, D. B. Chrisey, and R. E. Leuchtner, "*In Situ*

Deposition of Epitaxial $PbZr_xTi_{1-x}O_3$ Thin Films by Pulsed Laser Deposition," *Appl. Phys. Lett.*, vol. 59, no. 13, pp. 1565–1567, 1991.

[89] C. H. Peng and S. B. Desu, "Structure Development Study of $Pb(Zr,Ti)O_3$ Thin Films by an Optical Method," *J. Am. Ceram. Soc.*, vol. 77, no. 6, pp. 1486–1492, 1994.

[90] A. Ito, A. Machida, and M. Obara, "Cobalt Doping in $BaTiO_3$ Thin Films by Two-Target Pulsed KrF Laser Ablation with *In Situ* Laser Annealing," *Appl. Phys. Lett.*, vol. 70, no. 25, pp. 3338–3340, 1997.

[91] K. D. Budd, S. K. Dey, and D. A. Payne, "Sol-Gel Processing of $PbTiO_3$, $PbZrO_3$, PZT and PLZT Thin Films," *Br. Ceram. Proc.*, vol. 36, pp. pp. 107–121, 1985.

[92] D. B. Chrisey and G. K. Hubler, *Pulsed Laser Deposition of Thin Films*. Wiley Interscience, 1994.

[93] K. C. Chen and J. D. Mackenzie, "Crystallization Kinetics of Metallo-Organics Derived PZT Thin Film," *MRS Proc.*, vol. 180, p. 663, 1990.

[94] D. B. Geohegan, "Diagnostics and Characterization of Pulsed Laser Deposition Laser Plasmas," in *Pulsed Laser Deposition of Thin Films*, D. B. Chrisey and G. K. Hubler, Eds. John Wiley & Sons, 1994, pp. 115–165.

[95] D. L. Smith, "Surface Effects," in *Thin-Film Deposition: Principles and Practice*, McGraw-Hill, 1995, pp. 402–411.

[96] H. Fujiwara, "Dielectric Function Models," in *Spectroscopic Ellipsometry: Principles and Applications*, John Wiley & Sons, 2007, pp. 158–176.

[97] S. Trolier-McKinstry, H. Hu, S. Krupanidhi, P. Chindaudom, K. Vedam, and R. Newnham, "Spectroscopic Ellipsometry Studies on Ion Beam Sputter Deposited Pb(Zr, Ti)O_3 Films on Sapphire and Pt-Coated Silicon Substrates," *Thin Solid Films*, vol. 230, pp. 15–27, 1993.

[98] I. Reaney, D. Taylor, and K. Brooks, "Ferroelectric PZT Thin Films by Sol-Gel Deposition," *J. Sol-Gel Sci. Technol.*, vol. 13, pp. 813–820, 1998.

[99] R. Koba and C. E. Wickersham, "Temperature and Thickness Effects on the Explosive Crystallization of Amorphous Germanium Films," *Appl. Phys. Lett.*, vol. 40, no. 8, pp. 672–675, 1982.

[100] J. Thornton, "High Rate Thick Film Growth," *Annu. Rev. Mater. Sci.*, vol. 7, pp. 239–260, 1977.

[101] I. Petrov, P. B. Barna, L. Hultman, and J. E. Greene, "Microstructural Evolution During Film Growth," *J. Vac. Sci. Technol. A Vacuum, Surfaces, Film.*, vol. 21, no. 5, p. S117, 2003.

[102] W. Nix and B. Clemens, "Crystallite Coalescence- A Mechanism for Intrinsic Tensile Stresses in Thin Films," *J. Mater. Res.*, vol. 14, no. 8, pp. 3467–3473, 1999.

[103] E. Klokholm and B. S. Berry, "Intrinsic Stress in Evaporated Metal Films," *J. Electrochem. Soc.*, vol. 115, no. 8, pp. 823–826, 1968.

[104] S. Corkovic, Q. Zhang, and R. W. Whatmore, "The Investigation of Key Processing Parameters in Fabrication of Pb(Zr_xTi_{1-x})O_3 Thick Films for MEMS Applications," *J. Electroceramics*, vol. 19, no. 4, pp. 295–301, Mar. 2007.

[105] C. Kwok and S. Desu, "Pyrochlore to Perovskite Phase Transformation in Sol-Gel Derived Lead-Zirconate-Titanate Thin Films," *Appl. Phys. Lett.*, vol. 60, no. 12, pp. 1430–1432, 1992.

[106] A. Chojnacka and M. O. Thompson, "Morphological Instabilities during Explosive Crystallization of Germanium Films," *MRS Symp. Proc.*, vol. 648, pp. P11.12.1 – P11.12.8, 2001.

[107] C. E. Wickersham, G. Bajor, and J. E. Greene, "Impulse Stimulated 'explosive' Crystallization of Sputter Deposited Amorphous (In,Ga)Sb Films," *Solid State Commun.*, vol. 27, no. 1, pp. 17–20, 1978.

[108] R. W. Collins, A. S. Ferlauto, G. M. Ferreira, C. Chen, J. Koh, R. J. Koval, Y. Lee, J. M. Pearce, and C. R. Wronski, "Evolution of Microstructure and Phase in Amorphous, Protocrystalline, and Microcrystalline Silicon Studied by Real Time Spectroscopic Ellipsometry," *Sol. Energy Mater. Sol. Cells*, vol. 78, no. 1–4, pp. 143–180, 2003.

[109] S. Kim and R. W. Collins, "Optical Characterization of Continuous Compositional Gradients in Thin Films by Real Time Spectroscopic Ellipsometry," *Appl. Phys. Lett.*, vol. 67, no. 1995, p. 3010, 1995.

[110] F. Spaepen, "Interfaces and Stresses in Thin Films," *Acta Mater.*, vol. 48, no. 1, pp. 31–42, Jan. 2000.

[111] R. Abermann and R. Koch, "*In Situ* Study of Thin Film Growth by Internal Stress Measurement Under Ultrahigh Vacuum Conditions: Silver and Copper Under the Influence of Oxygen," *Thin Solid Films*, vol. 142, no. 1, pp. 65–76, Aug. 1986.

[112] R. Abermann, “Measurements of the Intrinsic Stress in Thin Metal Films,” *Vacuum*, vol. 41, pp. 1279–1282, 1990.

[113] G. Thurner and R. Abermann, “Internal Stress and Structure of Ultrahigh Vacuum Evaporated Chromium and Iron Films and Their Dependence on Substrate Temperature and Oxygen Partial Pressure During Deposition,” *Thin Solid Films*, vol. 192, pp. 277–285, 1990.

[114] J. Shepard, S. Trolier-McKinstry, M. Hendrickson, and R. Zeto, “The Effects of Biaxial Stress on the Ferroelectric Characteristics of PZT Thin Films,” *Mater. Res. Soc. Symp. Proc.*, vol. 459, pp. 47–51, 1997.

[115] D. Damjanovic and M. Demartin, “The Rayleigh Law in Piezoelectric Ceramics,” *J. Phys. D. Appl. Phys.*, vol. 29, no. 7, pp. 2057–2060, Jul. 1996.

[116] W. Cao and C. A. Randall, “Grain Size and Domain Size Relations in Bulk Ceramic Ferroelectric Materials,” *J. Phys. Chem. Solids*, vol. 57, no. 10, pp. 1499–1505, 1996.

[117] C. A. Randall, N. Kim, J.-P. Kucera, W. Cao, and T. R. Shrout, “Intrinsic and Extrinsic Size Effects in Fine-Grained Morphotropic-Phase-Boundary Lead Zirconate Titanate Ceramics,” *J. Am. Ceram. Soc.*, vol. 81, no. 3, pp. 677–688, 1998.

[118] G. Arlt and N. a. Pertsev, “Force Constant and Effective Mass of 90^{o} Domain Walls in Ferroelectric Ceramics,” *J. Appl. Phys.*, vol. 70, no. 1991, pp. 2283–2289, 1991.

[119] N. Bassiri-Gharb, I. Fujii, E. Hong, S. Trolier-McKinstry, D. V. Taylor, and D. Damjanovic, “Domain Wall Contributions to the Properties of Piezoelectric Thin

Films," *J. Electroceramics*, vol. 19, no. 1, pp. 47–65, 2007.

[120] S. Jesse, S. V. Kalinin, R. Proksch, A. P. Baddorf, and B. J. Rodriguez, "The Band Excitation Method in Scanning Probe Microscopy for Rapid Mapping of Energy Dissipation on the Nanoscale," *Nanotechnology*, vol. 18, p. 435503, 2007.

[121] P. Bintachitt, S. Jesse, D. Damjanovic, Y. Han, I. M. Reaney, S. Trolier-McKinstry, and S. V Kalinin, "Collective Dynamics Underpins Rayleigh Behavior in Disordered Polycrystalline Ferroelectrics.," *Proc. Natl. Acad. Sci. U. S. A.*, vol. 107, no. 16, pp. 7219–7224, 2010.

[122] S. Halder, U. Boettger, T. Schneller, R. Waser, O. Baldus, P. Jacobs, and M. Wehner, "Laser Annealing of BST Thin Films with Reduced Cracking at an Elevated Temperature," *Mater. Sci. Eng. B*, vol. 133, no. 1–3, pp. 235–240, Aug. 2006.

[123] T. Tsuchiya, K. Daoudi, T. Manabe, I. Yamaguchi, and T. Kumagai, "Preparation of The La0.8Sr0.2MnO3 Films on STO and LAO Substrates by Excimer Laser-Assisted Metal Organic Deposition using the KrF Laser," *Appl. Surf. Sci.*, vol. 253, no. 15, pp. 6504–6507, May 2007.

[124] E. K. Michael-Sapia, H. U. Li, T. N. Jackson, and S. Trolier-McKinstry, "Nanocomposite Bismuth Zinc Niobate Tantalate for Flexible Energy Storage Applications," *J. Appl. Phys.*, vol. 118, no. 23, 2015.

VITA

Adarsh Rajashekhar was born in Sagar (State: Karnataka), India, on April 9th, 1985. In 2007, he received a Bachelor of Technology degree in Metallurgical and Materials Engineering from the Indian Institute of Technology Madras, India. He then went on to obtain his M.S. degree in Materials Science and Engineering in 2009 from the Ecole Polytechnique Federale de Lausanne (EPFL), Switzerland. In the fall of 2009, he began his doctorate degree under the guidance of Dr. Susan Trolier-McKinstry in the department of Materials Science and Engineering at Pennsylvania State University.